Visible Light Communication and Positioning for Autonomous Vehicles

by

Burak Soner

A Dissertation Submitted to the
Graduate School of Sciences and Engineering
in Partial Fulfillment of the Requirements for
the Degree of

Doctor of Philosophy

in

Electrical and Electronics Engineering

KOÇ ÜNİVERSİTESİ

January 17, 2022

Visible Light Communication and Positioning for Autonomous Vehicles

Koç University

Graduate School of Sciences and Engineering

This is to certify that I have examined this copy of a doctoral dissertation by

Burak Soner

and have found that it is complete and satisfactory in all respects,

and that any and all revisions required by the final

examining committee have been made.

Committee Members:

Prof. Sinem Çöleri (Advisor)

Prof. Alper Erdoğan

Prof. Öznur Özkasap

Prof. Sinan Gezici

Prof. Murat Uysal

Date:

Edibe, Samiye ve Tayyar'a

ABSTRACT

Visible Light Communication and Positioning for Autonomous Vehicles
Burak Soner
Doctor of Philosophy in Electrical and Electronics Engineering
January 17, 2022

Automotive research is currently heavily oriented towards autonomy and especially developing reliable vehicular connectivity and localization technologies for autonomous driving. Since existing technologies have failed to satisfy all requirements so far, new complementary technologies are sought. Specifically, radio frequency communications like cellular and "DSRC" suffer from reliability and security issues at mid-range (<100 m) congested driving scenarios due to heavy interference, and sensor-based localization systems (e.g., GPS, vision) fail to provide the required accuracy and rate due to sensor rate limitations and prohibitively high computational complexity. Recently, visible light communication (VLC) and positioning (VLP) technologies, based on modulated LED head/tail lights and low-cost photodiodes, were conjectured to be promising complementaries that can help solve these problems and enable challenging applications like collision avoidance and platooning. This thesis aims to prove that vehicular VLP can realize this promise.

First, we describe the vehicular VLC system model and provide the problem definition for vehicular VLP considering relative positioning of vehicles using VLC signals. Then, we propose a "VLP-friendly" improvement to the vehicular VLC physical layer: A novel receiver design that enables realizing high-accuracy angle-of-arrival based vehicular VLP methods in low complexity and cost (named "QRX"). Next, we review state-of-the-art positioning algorithms used in vehicular VLP and propose new algorithms that advance the state-of-the-art, most of which are exclusively enabled by the QRX. Finally, we derive the Cramer-Rao lower bounds on positioning accuracy for all algorithms and also simulate their performances under challenging weather and noise conditions in realistic driving scenarios. The results prove the eligibility of vehicular VLP for use as a suitable complementary technology for collision avoidance and platooning scenarios in future autonomous vehicles.

ÖZETÇE

Otonom Araçlar için Görünür Işıkla Haberleşme ve Konumlama
Burak Soner
Elektrik ve Elektronik Mühendisliği, Doktora
17 Ocak 2022

Otomotiv araştırmaları şu anda ağırlıklı olarak otonom sürüşe, ve özellikle de bu amaca yönelik güvenilir araç haberleşme ve konumlama teknolojileri geliştirmeye odaklanmıştır. Mevcut teknolojiler tüm gereksinimleri karşılayamadığı için tamamlayıcı teknolojiler aranmaktadır. Spesifik olarak, hücresel ve "DSRC" gibi radyo frekans haberleşme teknolojileri orta menzil (<100 m) sıkışık trafikte karışımdan ötürü güvenlik ve güvenilirlik isterlerini sağlayamamakta, ve sensörlü konumlama sistemleri de (GPS, kamera gibi) sensör hızı limitleri ve çok yüksek hesap karmaşıklığı nedeniyle doğruluk ve hız isterlerini sağlayamamaktadır. Son zamanlarda araç LED farlarını ve düşük maliyetli fotodiyotları kullanan görünür ışıkla haberleşme (GIH) ve konulama (GIK) teknolojilerinin bu sorunları çözerek çarpışma önleme ve otonom konvoy gibi zorlu uygulamaları mümkün kılabilecek tamamlayıcı teknolojiler olabilecekleri vaadedilmiştir. Bu tezin amacı, bu vaatleri GIK özelinde doğrulamaktır.

Tezde ilk olarak araçlar için GIH sistem modelini açıklıyoruz ve ilgili GIK problemini, yani GIH sinyallerini kullanarak araçlar arası konumlama yapma problemini, tanımlıyoruz. Ardından, GIH/GIK fiziksel katmanı için varış açısı ölçümü tabanlı araç GIK metodlarını yüksek doğruluk, düşük maliyet ve düşük karmaşıklıkta gerçeklemeye izin veren "QRX" isminde yeni bir alıcı tasarımı öneriyoruz. Daha sonra, son teknoloji GIK algoritmaları literatürünün bir incelemesini sunuyoruz, ve son teknolojiyi iyileştiren yeni algoritmalar öneriyoruz; bunların çoğu münhasır olarak QRX sayesinde gerçeklenebilen yöntemlerdir. Son olarak, tüm algoritmalar için Cramer-Rao konumlama doğruluğu alt sınırlarını türetiyor, ve bu algoritmaların gerçekçi ve zorlu sürüş, hava ve GIH kanal gürültüsü koşulları altındaki performanslarını sayısal benzetim ile değerlendiriyoruz. Sonuçlar GIK teknolojisinin gelecekteki otonom araçlarda çarpışma önleme ve otonom konvoy uygulamaları için uygun bir tamamlayıcı teknoloji olarak kullanılabileceğini kanıtlıyor.

ACKNOWLEDGMENTS

First, I would like to sincerely thank my advisor Prof. Sinem Çöleri for her guidance and help throughout my PhD journey and for being a source of inspiration through setting a great example of what academic success looks like. Similarly, I would like to also thank the committee members, especially Prof. Alper Erdoğan and Prof. Öznur Özkasap who provided very valuable feedback and suggestions throughout all thesis monitoring meetings, and also Prof. Murat Uysal and Prof. Sinan Gezici, for their contributions. I would like to thank my colleagues at the Wireless Network Laboratory (WNL), Gökhan Gürbilek, Mertkan Koca, Dr. Buğra Turan and Ali Uyruş, for their contributions and support at all the hustle and hard work we have been through together. I would also like to thank our collaborators at Ford Otosan for helping our research work stay industrially relevant.

On a personal note, I would like to thank Prof. Asif Šabanović and Prof. Tarik Uzunović for molding a researcher out of the confused undergrad I was back in 2014, and for giving me the first push towards doing a PhD. I would like to thank Prof. Hakan Ürey, Prof. Göksen Yaralıoğlu, Dr. Erdem Ulusoy, Dr. Kıvanç Hedili, Dr. Uğur Aygün and all my colleagues at the Optical Microsystem Laboratory (OML) and CY Vision for showing me what being a PhD student and doing cutting edge research is like, and for bearing with me while I transformed into an engineer that can actually do those things.

Finally, I would like to express my deepest gratitude to my family and my friends for their encouragement, guidance and continuous support in this process, and for shaping me into the individual I am today. I am sincerely grateful for having you in my life.

TABLE OF CONTENTS

LIST OF TABLES

LIST OF FIGURES

ABBREVIATIONS

AoA	Angle-of-arrival
AWGN	Additive White Gaussian Noise
CRLB	Cramer-Rao Lower Bound
DGPS	Differential Global Positioning System
DSRC	Dedicated Short Range Communications
ETSI	European Telecommunications Standards Institute
IM/DD	Intensity Modulation / Direct Detection
LED	Light Emitting Diode
LIDAR	Light Detection and Ranging
LoS	Line-of-Sight
LTE	Long Term Evolution
MIMO	Multiple-Input-Multiple-Output
MLE	Maximum Likelihood Estimation
MVUE	Minimum Variance Unbiased Estimator
RBLS	Rao-Blackwell-Lehmann-Scheffe
RF	Radio Frequency
RX	Receiver
SAE	Society of Automotive Engineers
SLAM	Simulatenous Localization and Mapping
SWaP	Size-Weight-and-Power
TIA	Transimpedance Amplifier
TX	Transmitter
VANET	Vehicular Ad-Hoc Networks
VLC	Visible Light Communication
VLP	Visible Light Positioning

Chapter 1

INTRODUCTION

Automotive research is currently heavily oriented towards improving driving safety and efficiency through vehicular automation and autonomy [Ford, 2018]. A multitude of significant legal, social, economical and technical challenges are faced for the widespread deployment of such self-driving vehicles in traffic [Maurer et al., 2016]. The technical problems related to making a vehicle fully autonomous, which have been under investigation for a few decades now, continues to motivate innovation, especially for areas related to automated robot perception and navigation [Faisal et al., 2021]. Although there has been significant progress, a fully autonomous vehicle that can perform safely and reliably under any road and environment condition, is yet to be realized. For instance, the problem of autonomously navigating a single vehicle in an unknown but static or slowly-changing environment was largely solved by early work on Simultaneous Localization and Mapping (SLAM), as most popularly demonstrated during the DARPA Grand Challenges of 2004-2007 [Thrun et al., 2006]. However, employing multiple autonomous vehicles in dynamic traffic environments without compromising transportation efficiency (i.e., sustaining sufficiently high traffic flow) and/or occupant and pedestrian safety (i.e., avoiding crashes) is still an open topic that continually generates extremely hard problems compared to the single agent case, motivating ongoing related research efforts.

The Society of Automotive Engineers (SAE) categorizes the efforts towards developing such "fully autonomous" vehicles for civilian traffic into 5 levels (L#), with L5 corresponding to a vehicle that does not require any input from a human driver [SAE, 2021]. An L5 driving system is expected to have the following core functions, which are also depicted in Fig. 1.1 [Pendleton et al., 2017]:

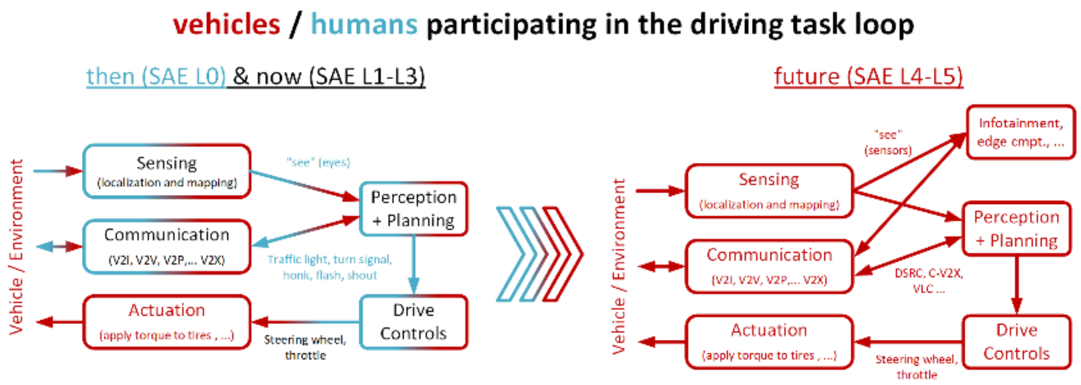

Figure 1.1: The anatomy of autonomous driving systems. Drawing influenced by the system perspective in [Pendleton et al., 2017].

- *Perception & Coordination*: The autonomous vehicle needs to have situational awareness in the dynamically changing road environment [Sirkin et al., 2017]. Specifically, it needs to be aware of what state its driving environment is in, and what the other mobile agents within its driving environment are doing, at all times. This implies that the vehicle needs to succeed in tasks such as sensing road and weather conditions [Wedel et al., 2009], recognizing drivable and non-driveable areas [Thrun et al., 2006], localizing other static and quasi-static road entities (e.g., pedestrians) and objects [Lategahn and Stiller, 2014], and finding and updating the real-time relative position of other moving vehicles such as cars or motorcycles. There are many open problems in these fields, especially in effective communication, detection, identification/recognition and localization technologies for all road entities including vehicles, pedestrians and road infrastructure units such as traffic lights.

- *Planning:* The autonomous vehicle needs to act pro-actively in terms of where it's planning to go. This implies that the vehicle needs to succeed in path, motion, behavior and overall mission planning in dynamic environments [Dolgov et al., 2010]. There are many open problems in these fields, especially in probabilistic path prediction and planning methods that work robustly and efficiently even when a large number of highly dynamic entities are involved.

- *Control:* Once it perceives its environment and plans its move, the autonomous vehicle needs to be able to actually go where it plans to go. Accordingly, "drive-by-wire" systems which consider the fail-operational [Stolte et al., 2021] control and automation of vehicle motion actuators, has become a mature and standardized field in the recent years [Sinha, 2011] and has enjoyed widespread deployment in the sector [Isermann et al., 2002].

Recently popularized attempts at building L5 vehicles have focused exclusively on enhancing perception and planning systems, disregarding the coordination aspect (e.g., Tesla Autopilot). However, such efforts have largely failed to jointly satisfy traffic efficiency, reliability and safety requirements at the macro level [Brown and Laurier, 2017]. Majority of the automakers have now switched gears, developing L2 and L3 vehicles that heavily rely on coordination through vehicular communications rather than taking blind shots at standalone L5 capabilities that utilize only sensor-based perception. Consequently, recent emergence of high-performance brand-agnostic RF communication technologies like 802.11p and LTE C-V2X has already enabled automakers to roll-out some L2 vehicles (and as very recently announced by Daimler, UN-R157 [UNECE, 2021] compliant L3 vehicles) with automated safety functions such as forward collision warning, emergency braking and lane keeping. However, although the final goal is still L5, none of the existing technologies for communication and perception are ready for supporting L5 driving capability with high reliability, efficiency and safety under all road conditions yet. Currently, the best approach at a safe, efficient and reliable perception (mainly, localization and positioning) and communication/coordination system for autonomous driving is combining multiple complementary and redundant technologies without high additional costs [Zheng et al., 2015].

Accordingly, there has been a recent focus towards research on better vehicular communication and localization technologies which enable automated driving functions that incrementally pave the way towards fully autonomous vehicles

[Papadimitratos et al., 2009]. A chronological list of such driving functionalities categorized according to the level of automation, are provided in Fig. 1.2.

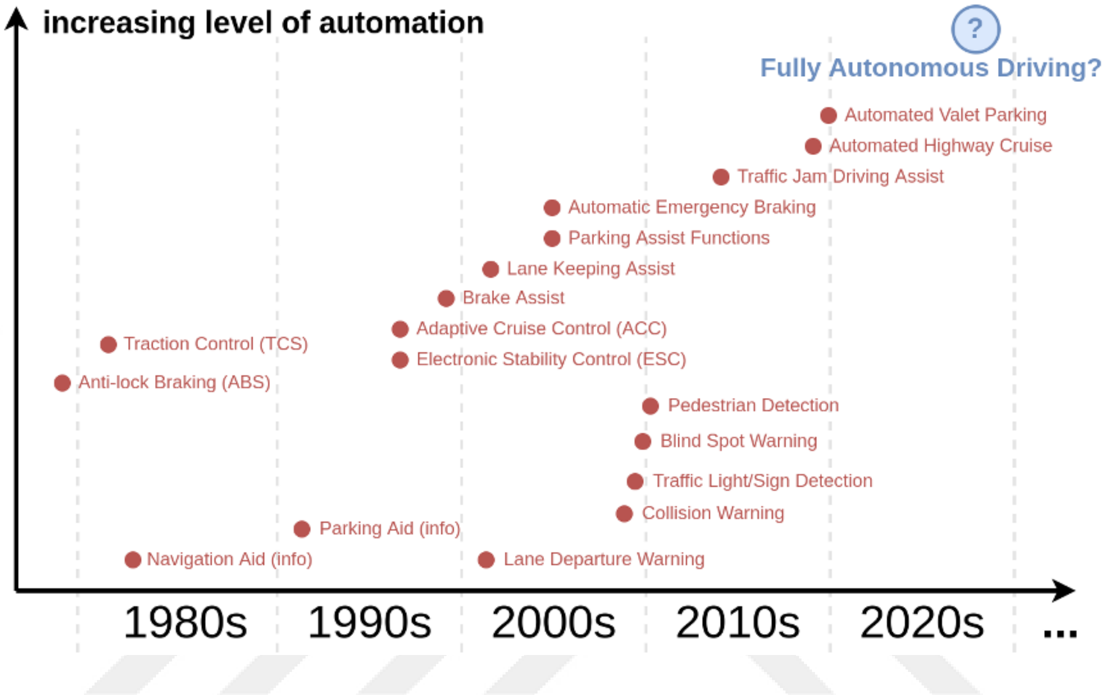

Figure 1.2: Automated driving function deployments over the years. Recent additions that pave the way towards fully autonomous driving heavily rely on vehicular communication and localization technologies. Adapted from [Beiker, 2016].

1.1 *Communication and Localization for Autonomous Driving*

Vehicular communication and localization technologies aim to make traffic safer and more efficient for a multitude of road entities including vehicles, pedestrians and infrastructure units such as traffic lights and buildings. These technologies are therefore studied under different interaction categories such as vehicle to infrastructure (V2I), vehicle to vehicle (V2V) and pedestrian to infrastructure (P2I), as pictured in Fig. 1.3. The umbrella term for technologies related exclusively to vehicles is vehicle-to-everything (V2X).

While all of these technologies have significant impact on the overall autonomous traffic framework, some categories have heavier implications in terms of safety since

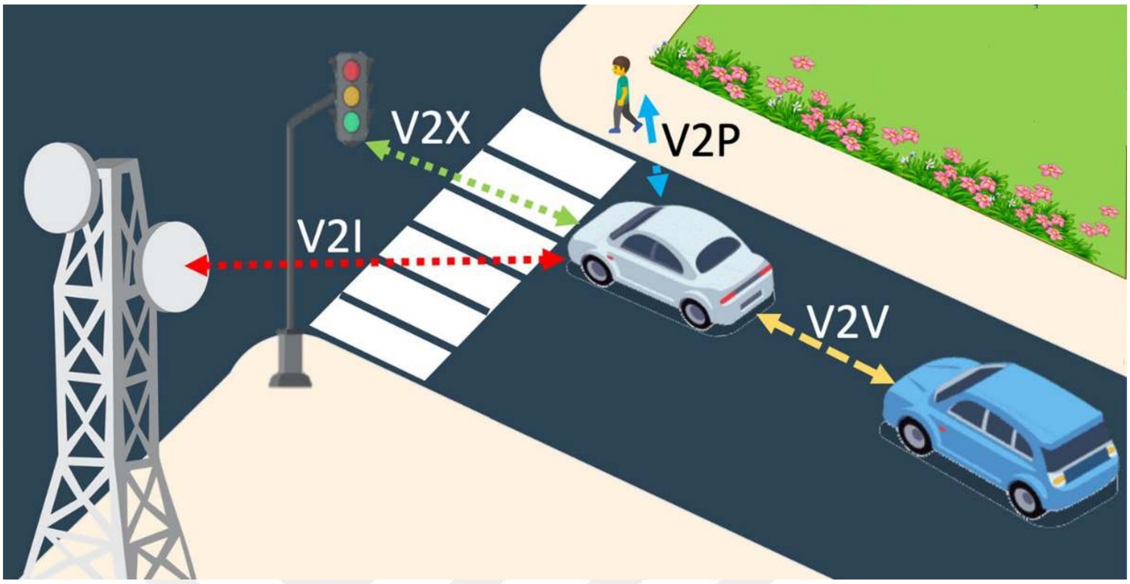

Figure 1.3: Different interaction modes between road entities. Figure adapted from [Zeadally et al., 2020].

the distribution and severity of traffic accidents vary a lot from one interaction type to another, making research on some categories more safety-critical than others. For instance, the annual traffic accident report published by the Federal Statistical Office of Germany (DESTATIS) [DESTATIS, 2017] shows that 63% of traffic accidents are V2V collisions, demonstrating the importance of V2V communication and localization technologies for collision avoidance and safe platooning applications in future automated/autonomous vehicle safety concepts [Kusano and Gabler, 2012a]. Accordingly, we focus on V2V communications and localization used for collision avoidance and safe platooning applications in this thesis.

1.1.1 Vehicle-to-Vehicle (V2V) Communication

V2V communication is currently pre-dominantly based on radio frequency (RF) technologies like cellular communications ("C-V2X") and Dedicated Short Range Communications (DSRC) using the IEEE 802.11p protocol, including ETSI ITS-G5

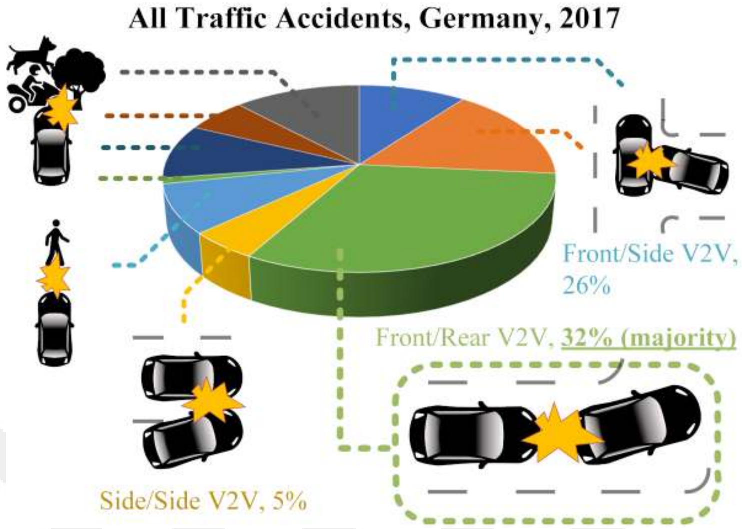

Figure 1.4: Distribution of traffic accident types [DESTATIS, 2017]. This emphasizes the importance of V2V communication and localization technologies for collision avoidance and safe platooning, as also stated in [Kusano and Gabler, 2012a].

and WAVE [Ansari, 2021, Kiela et al., 2020, Mannoni et al., 2019, Eckhoff et al., 2013]. These V2V technologies have enabled the first realizations of vehicular adhoc networks (VANETs) which support various classes of new driving applications ranging from infotainment and advertisement to driver assistance and safety [Lee and Atkison, 2021]. Some example automated safety functions that these technologies enable and their communication latency and range requirements are listed in Table 1.1, which is adapted from [Cailean et al., 2014].

Although these RF V2V technologies have satisfied the requirements for such simple automated safety applications and advanced the state-of-the-art in safe autonomous driving, they have significant security vulnerabilities [Ucar et al., 2016] and their performance heavily suffers from interference in congested traffic scenarios [Bazzi, 2019]. The main culprit here is their omni-directional antenna characteristics, which makes it easier for malicious eavesdroppers and jammers to interfere with communications and also generates a significant amount of undesired multi-path components on the channel. Technologies with directional propagation characteris-

Table 1.1: Example Automated Safety Functions for RF V2V Communications

function	range requirement	latency requirement
Emergency Electronic Brake Light	300 m	100 ms
Co-operative Collision Mitigation [a]	50 m	20 ms
Forward Collision Warning	150 m	100 ms
Lane Change Warning	150 m	100 ms

[a] Mark that this is warning-based. Automated collision avoidance requirements are more stringent.

tics like millimeter-wave [Va et al., 2016] and visible light communications (VLC) [Căilean and Dimian, 2017] can complement RF technologies to improve security and reliability in short to mid-range scenarios [Cailean et al., 2014]. Due to the lack of manufacturing and design infrastructure for these new technologies in the automotive sector, solutions that require minimal design effort and minimal additional cost are highly valuable. To this end, VLC promises to be a very efficient complementary technology since it simply uses readily available LED head/tail lights and low-cost photodiodes for V2V communication.

1.1.2 Relative Vehicle Positioning

Relative vehicle positioning considers an "ego" vehicle that tries to find the relative position of a "target" vehicle on the road; the ego vehicle repeats this for all other vehicles within its vicinity to build a real-time map of its environment and the surrounding dynamic agents for avoiding collisions and forming efficient driving platoons. The performance requirements for this capability can be grouped under 8 attribute categories [de Ponte Müller, 2017]:

1. *Positioning Accuracy*: The ego vehicle cannot realistically estimate the relative position of the target vehicle exactly correct at all times due to noise and other disturbances. The accuracy of this estimation denotes "how close" this

estimation is to the true relative position of the target vehicle. Accuracy requirements vary significantly from one application to the other, and will be discussed in a mathematically rigorous manner later in the text.

2. *Position Estimation Rate*: Since nearly all vehicle positioning methods are based on digital techniques, estimations are updated at a finite rate. Positioning rate is therefore an important performance attribute since the estimations need to “catch up” with the fast movement of the target vehicle.

3. *Effective Field-of-View for Valid Estimations*: Depending on the directionality and orientation of the estimation setup, the ego vehicle might be constrained to estimating the relative positions of vehicles that are only within a certain viewing frustum. However, as Fig. 1.4 shows, vehicles may crash into each other from various directions which may or may not be within this region. Therefore, the effective field-of-view of the vehicle position estimation method is an important attribute for high operational use case coverage.

4. *Dimensionality of Estimations*: While urban roads and highways are usually built in “piece-wise flat” form, and average vehicle heights do not differ more than a few centimeters, there are of course cases that violate these conditions and make 3D vehicle positioning an important requirement. However, 2D positioning (i.e., imagining a 2D coordinate system on the road surface) is sufficient for most safety-relevant applications such as collision avoidance.

5. *Target Identification Capability*: The ability to identify and track the individual trajectory of different vehicles on the road can bring benefits to both safety-relevant and general-purpose driving applications, and is therefore an important performance attribute.

6. *Cost and Size-Weight-and-Power (SWaP) of Estimation Setup*: Automotive is a heavily cost and SWaP constrained sector due to the extremely high number of units involved in production and sales every year. Therefore, decreasing the

cost and SWaP footprint of vehicle positioning solutions (e.g., avoiding high-cost sensors that need to be mounted on vehicle exteriors) is a highly valuable design aspect.

7. *Reliability of Position Estimations*: Although the road, weather and environment conditions may vary significantly throughout the operational lifetime of a vehicle positioning solution, sustaining the reliability of position estimations despite these variations is paramount since the estimations directly affect the performance of safety-relevant driving functions. This is an extremely hard problem due to the vast set of different conditions that the system can face, and currently the best approach is combining many complementary technologies that have failure modes that are "orthogonal" to each other with respect to the changing conditions.

8. *Availability of Estimations*: Estimation methods may rely on certain technologies and conditions (e.g., cameras need ambient light, some positioning methods require road infrastructure units like base stations), but if the availability of these are technologies and conditions are compromised throughout operation (e.g., reduced base station coverage on highways), loss of position estimation might cause severe and unacceptable safety vulnerabilities. The case for infrastructure units requires higher level macroeconomic planning, but even continuously available positioning methods that use on-board hardware may fail to provide estimation under certain conditions (e.g., cameras failing to recognize dark-clothed pedestrians at night). This is therefore another extremely hard problem that is currently approached by combining multiple redundant and complementary technologies.

The quantitative requirements for each of these performance attributes varies significantly from one application to the other. In this thesis, we consider collision avoidance and safe platooning applications since vehicle-to-vehicle collisions constitute the majority of traffic safety threats [Kusano and Gabler, 2012a]. These applications typically consider vehicles that are within 1 to 20 m distance of each other, driving in more or less longitudinally parallel trajectories (e.g., parallel lanes on a highway) at speeds greater than 30 km/h [Jootel, 2012]. This implies that the positioning problem can be safely formulated in 2D since most roads can be considered flat for such short distances [American Association of Highway and Transportation Officials (AASHTO), 2011a] and the field-of-view requirement isn't stringent since forward and backward facing positioning units suffice. Since vehicle relative speeds are very high in pre-crash scenarios and maneuvers should be decided in a very fast and accurate manner, cm-level position estimation accuracy and greater than 50 Hz update rate is required for full autonomy [Caveney, 2010, Shladover and Tan, 2006].

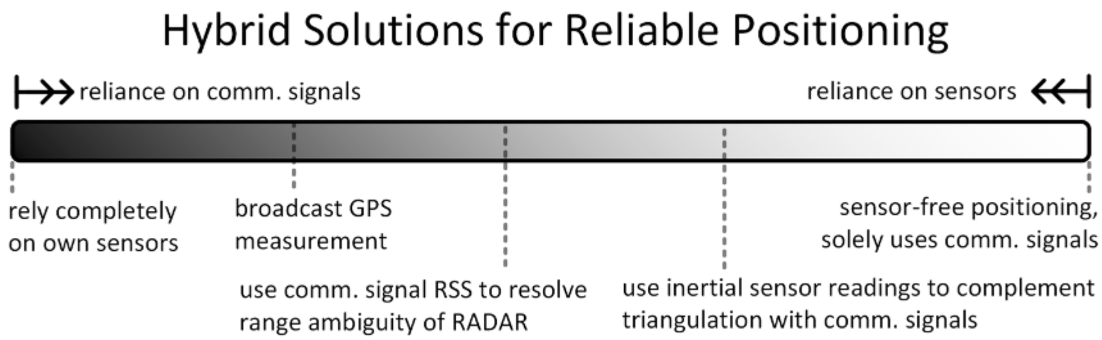

Figure 1.5: There is no "silver bullet" system that completely solves the relative vehicle positioning problem under all possible challenging road and environment conditions. Hybrid systems that utilize multiple complementary and redundant technologies for positioning is necessary. Positioning methods that utilize V2V communication signals is one promising addition.

While sensor-based solutions are the first approach to this kind of a positioning problem, these solutions currently cannot satisfy all requirements under all conditions. Co-operative approaches that utilize information from V2V communications for sensor/data fusion (e.g., using broadcasted global location information for removing inertial sensor drift) improve reliability and availability, but these hybrid methods also cannot solve the problem completely. Therefore, the best approach at solving this extremely hard problem is keeping a set of many different low-cost/SWaP complementary methods that provide high positioning accuracy and rate in order to improve reliability and availability under all conditions as much as possible. The growing maturity of V2V communication technologies offers another suitable addition to this hybrid relative vehicle positioning stack: methods that use communication signals from target vehicles directly for estimating their relative positions.

1.2 Communication-based Relative Vehicle Positioning

Current sensor-based methods for relative vehicle positioning, which are readily being used for less demanding conventional autonomous driving tasks, fail to meet the cm-level accuracy and >50 Hz rate requirements of collision avoidance and platooning systems [de Ponte Müller, 2017]. Differential Global Positioning System (DGPS), which is used for global self-localization, allows vehicles to also cooperatively localize each other. However, this sensor provides only meter-level accuracy at less than 20 Hz rate [Feng et al., 2008], and cannot provide high-precision location information since it regards vehicles as point objects. Alternatively, RADAR/LIDAR [Mukhtar et al., 2015] and camera-based methods [Badino et al., 2009], which are used for the localization of non-vehicle objects on the road, can be used for vehicle localization at up to cm-level accuracy. However, these methods are limited to less than 50 Hz rate since they require scanning, locating and labelling millions of points/pixels for object localization [Lategahn and Stiller, 2014]. On the other hand, communication-based positioning methods, which promise estimation of antenna positions at cm-level accuracy and greater than 50 Hz rate, can be extended for vehicle localization, enabling fully autonomous collision avoidance and safe platooning, and complementing the existing sensor-based vehicle positioning system for higher safety and driving efficiency.

Communication-based positioning methods in the vehicular domain mainly employ RF technologies such as cellular and DSRC [Abboud et al., 2016], and VLC technologies [Balico et al., 2018, Yu et al., 2013]. Cellular-based positioning methods either utilize location-fingerprinted received signal strength (RSS) measurements or apply triangulation via physical system parameters such as time-of-arrival (ToA), time-difference-of-arrival (TDoA) and angle-of-arrival (AoA) [Liu et al., 2007a]. However, these methods rely on tight synchronization between base stations and the mobile terminal, with limited accuracy due to excessive multi-path interference. Although pilot-based synchronization methods [Gustafsson and Gunnarsson, 2005] and estimators like multiple signal classification (MUSIC) [Klukas and Fattouche, 1998] somewhat mitigate these problems, overall cellular-based positioning accuracy is worse than 10 m in practical scenarios [Broumandan et al., 2008, Chen and Abedi, 2010]. DSRC also suffers from similar issues; while roundtrip-time-of-flight (RToF) methods successfully mitigate synchronization issues [Ciurana et al., 2009, Alam et al., 2011], the best reported accuracy is around 1-10 m [Alam and Dempster, 2013], still worse than the cm-level requirement.

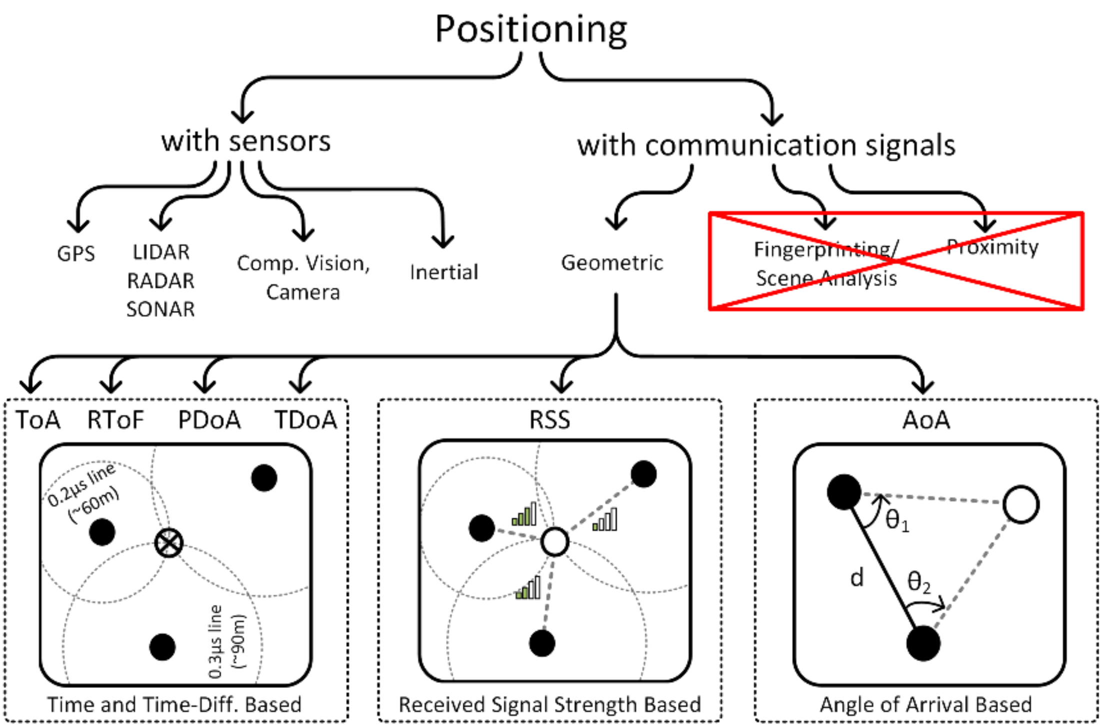

Figure 1.6: Categorization of geometric positioning methods that use communication signals. Fingerprinting and proximity-based position estimators are not suitable for vehicular use since they assume constant availability of high-definition RSS maps or landmark location maps.

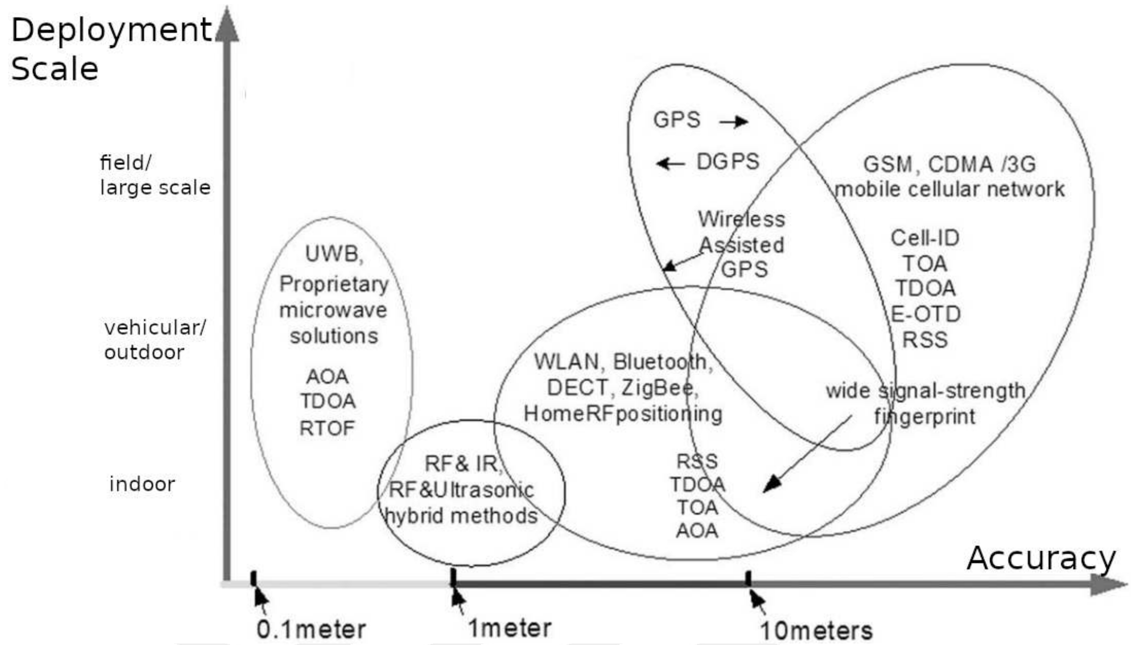

Figure 1.7: RF methods and GPS cannot provide cm-level (less than 10 cm) accuracy. DSRC-based positioning (not shown here) performs similar to cellular based methods [Alam and Dempster, 2013]. Figure adapted from [Liu et al., 2007a].

As an alternative, vehicular visible light positioning (VLP), which uses received directional VLC signals from modulated vehicle head/tail LED lights for positioning, fundamentally promises the required cm-level accuracy owing to the dominant line-of-sight (LoS) propagation characteristics of the channel at distances relevant to collision avoidance and platooning [Armstrong et al., 2013, Zhuang et al., 2018a, Turan et al., 2018, Turan and Coleri, 2021]. Moreover, vehicular VLP methods can also provide the required high positioning rates with moderate processing hardware due to their low computational complexity and robust target detection procedures that leverage similar functionalities from the communication subsystem; this is a significant advantage over sensor-based methods which would require costly accelerators (e.g., graphical processing units, GPUs) for achieving the same objective [Janai et al., 2020a, Mukhtar et al., 2015]. For these reasons, vehicular VLP can be a suitable complementary solution for vehicular localization.

1.3 Vehicular Visible Light Communication based Positioning

Vehicular VLP methods estimate relative vehicle position by finding the positions of the VLC transmitters (TX) that are on the target vehicle, with respect to the receivers (RX) that are on the ego vehicle. They estimate TX relative position in two steps. First, received noisy VLC signals are processed for measuring physical system parameters, i.e., relative bearing (angle-of-arrival, AoA) or range (distance) between a TX and one or more receivers (RX), with a certain level of accuracy. Next, these individual parameter measurements are combined to estimate the position of the VLC TX relative to the VLC RXs. This two-step estimation procedure is depicted in Fig. 1.8.

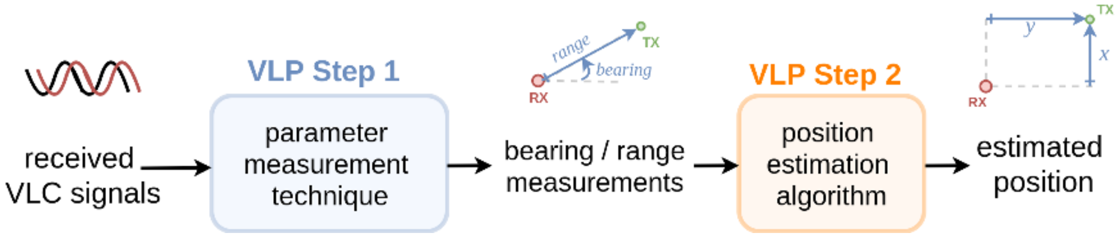

Figure 1.8: Anatomy of two-step position estimation in vehicular VLP methods.

The main sources of positioning error in these methods are VLC channel noise and high vehicle mobility, where the latter occurs due to the finite rate and latency of the position estimations. While this is a fundamental problem that affects all finite-rate localization methods and requires complex trajectory prediction solutions (e.g., [Lefèvre et al., 2014, Althoff et al., 2009]), this error naturally decreases with higher positioning rate and is typically negligible for realistic vehicle speeds when positioning rate is higher than 50 Hz. For this reason, the primary design goal of VLP methods for vehicular use cases is attaining greater than 50 Hz positioning rate while providing cm-level accuracy despite channel noise.

VLP methods were initially investigated for indoor use cases, aimed at localization of mobile RX units under LED ceiling light TX units [Keskin et al., 2018].

However, most of these methods designed for indoor use cases cannot directly be used for vehicular VLP since the vehicular domain differs from the indoor in three major aspects:

1. *Fewer TX, more RX units*: LED head/tail lights are the natural vehicular VLC TX unit choice due to their constant availability [Memedi and Dressler, 2020], and RX units are typically placed alongside TXs to simplify regulation compliance [Eldeeb and Uysal, 2019]. For this reason, vehicular use cases consider only two head or two (maximum three [Narmanlioglu et al., 2018]) tail lights as TX/RX units. However, indoor use cases typically consider a large number of TX ceiling luminaries and typically only one RX unit (e.g., a cell phone). Therefore, indoor VLP methods that rely on noise mitigation by averaging position estimations over a large number of TX units (e.g., [Eroglu et al., 2015]) do not work well in the vehicular domain.

2. *Very high mobility*: While vehicular use cases have very high TX-RX relative mobility resulting in frequent TX coverage fluctuations, indoor use cases consider very low RX mobility compared to the vehicular case and static TX units [Keskin et al., 2018]. Therefore, indoor VLP methods that rely on low mobility (e.g., by averaging more samples for noise mitigation at the cost of lower rate) do not work well in the vehicular domain. There are also some methods that re-interpret such indoor ceiling luminary-based methods for the vehicular domain by considering road/traffic lights as TX units [Bai et al., 2011, Mahmoud et al., 2020a]: Such vehicle-to-infrastructure methods are not suitable for collision avoidance and platooning since they suffer from the low availability of road lighting outside of urban regions.

3. *LoS-dominant channel*: The vehicular VLC channel is LoS-dominant [Turan et al., 2018, Turan and Coleri, 2021] but indoor channels typically contain significant non-LoS components due to high scattering/reflection. Specifi-

cally in such non-LoS-dominant channels, direct position estimation using RX VLC signal samples (i.e., no parameter measurement) theoretically provides marginally higher accuracy than two-step estimation (as shown for indoor environments in [Steendam et al., 2016a]), but has significantly higher complexity. For these reasons, even though direct estimation is applicable for vehicular use, its complexity is prohibitive especially under the 50 Hz estimation rate requirement, and it does not provide significant advantages in the vehicular domain since the channel is LoS-dominant [Keskin et al., 2017].

Accordingly, we categorize existing major works in VLP based on their use of direct or two-step estimation, the measured parameter(s) they utilize, and their applicability for collision avoidance and platooning, in Table 1.2. The state-of-the-art vehicular VLP methods proposed before this thesis [Roberts et al., 2010, Béchadergue et al., 2017] both utilize two-step estimation with "minimal" configurations: They require at most two TXs and two RXs on the vehicles and the positioning algorithms require the minimum number of measurements to be available from those units (i.e., just enough to formulate determined systems of equations, as opposed to least squares based algorithms which require lots of redundant measurements for high accuracy [Steendam et al., 2017]).

These existing simple vehicular VLP methods based on range measurements have already shown promising performance, but there is still room for significant improvement. Specifically, bearing-based VLP has not yet been investigated due to the lack of a suitable low-cost RX unit that provides high-accuracy bearing measurements. Furthermore, VLP methods that use multiple measurements from the same RX unit rather than from multiple RX units simultaneously, have not yet been investigated; these methods would improve the effective field-of-view of vehicular VLP since they only require one RX unit to sustain LoS with the target TX unit at a given time. Moreover, the performance of vehicular VLP has so far only been tested under limited test cases that do not fully represent the conditions that are faced under normal operation; this makes it hard to determine the exact role of vehicular VLP

Table 1.2: Existing VLP Methods, Indoor and Vehicular

reference	est.[a]	useful for collision avoidance and platooning?
[Steendam et al., 2016a]	D	×, indoor, not applicable, requires more TXs than available on the target vehicle for non-parallel TX/RX or for non-planar (i.e., not on a ceiling) TX arrays; both conditions occur frequently in the vehicular case. [Keskin et al., 2018] summarizes all methods in this category.
[Steendam et al., 2017], [Eroglu et al., 2015], [Zhu et al., 2017]	B	
[Jung et al., 2011], [Nadeem et al., 2014]	R	
[Yang et al., 2014a], [Prince and Little, 2012]	H	
[Steendam, 2017]	B	×, indoor, not applicable, algos diverge in the high-mobility case without good data
[Mazuelas et al., 2018]	R	
[Mahmoud et al., 2020b]	D	×, vehicular but not applicable since fixed co-planar TX arrays are assumed (traffic/road lights); these methods are useful for vehicle-to-infrastructure applications
[Shieh et al., 2017], [Yamazato and Haruyama, 2014]	B	
[Bai et al., 2011], [He and Zhou, 2021]	R	
[Lu and Chen, 2013], [Lu and Chen, 2010], [Shieh et al., 2018]	B	✓, but low precision [b] .
[Yamazato et al., 2014]	B	✓, but low VLC rate [Căilean and Dimian, 2017, Ziehn et al., 2020] and costly [c].
[Xu and Xu, 2019]	R	✓, but needs ≫2 RXs for high accuracy.
[Roberts et al., 2010, Béchadergue et al., 2017]	R	✓✓, state-of-the-art methods before this thesis

[a] Estimation method: (D)irect, (B)earing-based, (R)ange-based, (H)ybrid.
[b] Due to the use of tilted (pyramid) angular diversity RX units.
[c] Special high-FPS camera, still achieves only 500 bps VLC rate per link.

within the relative vehicle positioning technology stack. Theoretical analyses and simulated comparative performance benchmarks for vehicular VLP methods under realistic and challenging road and weather conditions are necessary. While theoretical analyses exist for indoor VLP [Zhuang et al., 2018b, Luo et al., 2017, Do and Yoo, 2016, Keskin and Gezici, 2016, Keskin et al., 2018], these cannot directly be used for evaluating vehicular VLP methods due to the major discrepancies between the two domains, as discussed earlier. Overall, these shortcomings in the existing literature emphasize the need for a comprehensive study that clarifies the potential of VLP for relative vehicle positioning in collision avoidance and platooning applications.

1.4 Outline of the Thesis and Contributions

In this thesis, we aim to advance the state-of-the-art in vehicular VLP and prove its eligibility for use as a complementary relative vehicle positioning technology for collision avoidance and platooning applications in the automotive sector. To this end, we make the following contributions to the existing literature:

- We propose a novel low-cost/size VLC RX design which enables high-rate VLC and high-accuracy, high-resolution and high-rate bearing measurement, simultaneously; we call this design "QRX". This design enables the first practical vehicular implementation of bearing-based VLP methods for relative vehicle positioning at cm-level accuracy and higher than 50 Hz rate and also has much lower complexity and cost compared to the range measurement techniques envisioned by previous vehicular VLP methods in the literature. QRX design is described in detail in [Soner and Coleri, 2021c] and a proof-of-concept experimental setup was presented in [Soner and Coleri Ergen, 2019b].

- We build and evaluate an in-house prototype vehicular VLC TX LED driver out of low-cost commercial-off-the-shelf components for supporting trials with QRX and as part of the collaboration in our lab with Ford Otosan. Performance evaluations and design details for the driver were documented in an internal technical project report at Ford Otosan [Soner et al., 2020], and the driver schematics and main design principles are provided in this thesis.

- We review feasible bearing/range measurement techniques other than QRX and the existing algorithms that use these techniques for position estimation in vehicular VLP. We identify four previously unexplored vehicular VLP methods in the literature, and formulate associated positioning algorithms that provide maximum likelihood estimation (MLE) given noisy parameter measurements for these methods. Three of these algorithms are exclusively enabled by the QRX, and one of those (namely, classical position fixing using direct bearing measurements) provides cm-level accuracy and greater than 50 Hz rate under most challenging road and channel conditions, significantly advancing the state-of-the-art. The review of parameter measurement techniques and positioning algorithms is provided in [Soner et al., 2022], and the novel algorithms are proposed in [Soner and Coleri, 2021c], [Soner and Coleri Ergen, 2019c], [Soner and Coleri Ergen, 2019a], and [Soner et al., 2022].

- We derive the Cramer-Rao lower bounds on positioning accuracy (CRLB) against parameter measurement noise for all state-of-the-art algorithms used in vehicular VLP in [Soner et al., 2022]. Since the bounds are derived with respect to input bearing/range measurements, they can be used for evaluating theoretical positioning accuracy of new bearing/range measurement techniques in the future. Similar analyses from indoor VLP (i.e., [Steendam et al., 2017, Keskin et al., 2018]) are not directly applicable here due to significant differences between indoor and vehicular VLP systems, so this thesis provides such theoretical analysis for the first time in vehicular VLP literature.

- We benchmark the state-of-the-art in vehicular VLP performance by simulating all methods under the same challenging noise and weather conditions for realistic driving scenarios in [Soner et al., 2022]. While individual vehicular VLP methods have been shown to satisfy the requirements for collision avoidance and platooning in earlier studies [Béchadergue et al., 2017, Yu et al., 2013], we improve upon these by providing extended results under realistic simulation scenarios that include recorded collision course trajectories, in fair comparison among all methods.

- We discuss, in detail, the open research questions and challenges faced for widespread deployment of vehicular VLP in the automotive sector and elaborate on potential solutions in detail to clarify the role of vehicular VLP for use as a complementary relative vehicle positioning technology in autonomous driving. This discussion is presented in [Soner et al., 2022].

We present these contributions in four chapters. The vehicular VLC-VLP system, including the system model assumptions, the mathematical definition of the received VLC signals and the associated problem definition for relative vehicle positioning using VLC signals (i.e., the vehicular VLP problem definition), is described in Chapter 2. Our prototype low-cost transmitter physical layer prototype is also presented in this chapter. Our "VLP-friendly" extension to the vehicular VLC physical layer, the novel low-cost/size QRX design, the associated angle-of-arrival (bearing) measurement procedure, and an experimental proof-of-concept study for the QRX (including a simple RX physical layer implementation), are presented in Chapter 3. Parameter measurement techniques other than bearing measurements with QRX (i.e., range measurement techniques that are used in previous vehicular VLP methods) and existing algorithms that use those techniques for position estimation in vehicular VLP are reviewed, the novel positioning algorithms are proposed, and the CRLBs for all algorithms (for both the proposed and the existing ones) are derived in Chapter 4. The CRLB evaluations and the simulations under realistic collision avoidance and platooning scenarios are presented in Chapter 5. Finally, remaining open questions and challenges are discussed, the findings in the thesis are summarized, and our conclusions are presented in Chapter 6.

Chapter 2

VEHICULAR VISIBLE LIGHT COMMUNICATION AND POSITIONING SYSTEM

This section describes the vehicular VLC system model, presents our low-cost TX prototype, defines the problem for relative vehicle positioning using parameter measurements over received VLC signals (i.e., two-step VLP), and provides the mathematical model of the received VLC signals that are used for those measurements.

The abstract block diagram of a VLC system is depicted in Fig. 2.1.

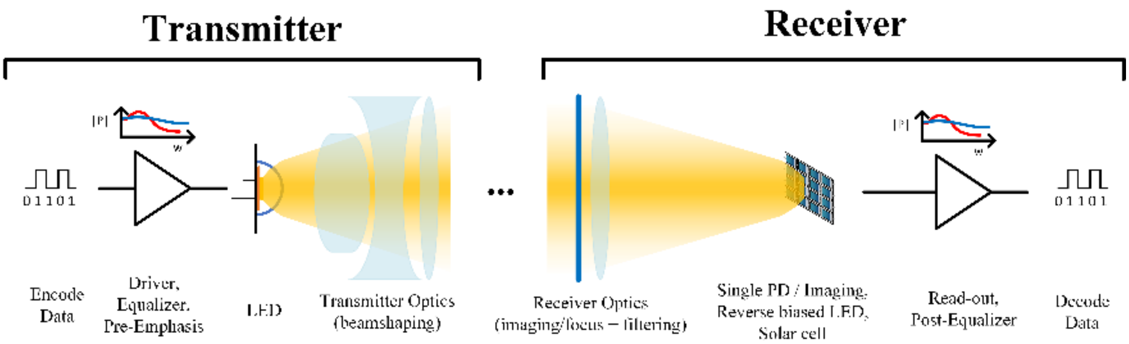

Figure 2.1: Components of a VLC system [Turan et al., 2019].

VLC transmitters typically use LEDs as light sources due to their high availability, high optical power output and low-cost. The intensity of the LED is modulated (IM) to carry a message signal, and a low-cost photodiode is used for direct detection (DD) on the receiver side (i.e., the VLC channel is "IM/DD" [Kahn and Barry, 1997]). VLC channel bandwidth is typically limited by the capacitive characteristics of high-power LED primary packages and photodiodes, making the design of TX LED drivers and RX read-out circuits that compensate for this characteristic an important issue. Moreover, the design of optical components that shape and filter the TX and RX beams is also important since the amount of received signal power directly influences communication and positioning reliability.

Vehicular realizations of VLC systems have additional constraints on TX and RX design that are based on regulations and automotive sector dynamics. We discuss these issues and describe vehicular VLC TX and RX designs, which are also used for positioning purposes via VLP methods, in the following.

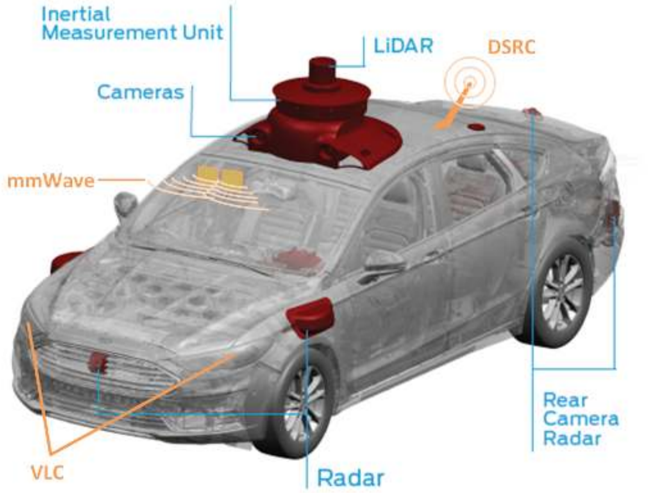

Figure 2.2: Vehicular VLC considers LED head/tail lights as TX units. It complements RF-based V2V communications and can be used for positioning (VLP) to complement sensor-based vehicle localization. Figure adapted from [Ford, 2018].

2.1 Vehicular VLC Transmitters

LED head/tail lights are the natural choice for vehicular VLC TX units due to their constant availability. However, the geometric placement and optical properties of these sources are practically fixed by strict traffic and eye safety regulations [Ko et al., 2012, National Highway Traffic Safety Administration, 1997, UN ECE Regulation, No R112, 2004, NHTSA, 2004], thus, they do not provide a degree-of-freedom in vehicular VLC system design. While the less-strictly-regulated roadside/traffic lights do get considered as TX units in some works, the low availability of such roadside luminaries outside of urban regions makes such systems practically unusable for collision avoidance and platooning applications. Therefore, LED head/tail lights can be accepted as TX units for vehicular VLC and VLP, as is.

One challenge associated with using automotive LED head/tail lights as VLC TX units is that their large-signal intensity modulation bandwidth is very limited compared to typical RF antennas [Windisch et al., 2000] (-3 dB bandwidth around 1 MHz [Turan et al., 2018]). While there are numerous reasons for this, mainly stemming from the radiative recombination phenomenon which generates the light in an LED, the major limiting effect is that of the high-capacitance package which is necessary for high optical power output. Pre-emphasis and equalization circuits that boost the effective bandwidth and flatten the frequency response of the LED have been studied for tackling this problem and increasing reliable VLC communication rates. While these works have not produced automotive VLC TX units that provide multiple GHz bandwidth like in the indoor case [Huang et al., 2015], works on modulation and coding strategies for VLC [Yesilkaya et al., 2017] have improved spectral efficiency to the point where vehicular VLC can satisfy the requirements for V2V communication with improved security benefits over existing RF technologies [Memedi and Dressler, 2020, Ucar et al., 2018].

One other challenge with using the LED as a transmitter is device non-linearity. The LED can be considered a current-mode device that produces optical power directly proportional to the amount of current that passes over it since its current-to-optical-power transfer function is mostly linear [Chen et al., 1999]. However, since its I-V characteristics are highly nonlinear due to varying AC impedance [Li et al., 1998], it cannot simply be driven by an impedance-matched antenna circuit like in RF because this would induce unwanted harmonics on the transmitted signal; the LED requires a linear, high-power and high-frequency controllable current sink in order to enable reliable IM/DD communications [Kahn and Barry, 1997]. In the following, we describe the design of a low-cost prototype for such a driver that we built in our lab for experimental proof-of-concept studies on vehicular VLC.

2.1.1 Our Prototype Low-Cost Vehicular VLC Transmitter

An LED driver that satisfies the vehicular VLC TX design constraints described above was not commercially available at the time of the experimental studies conducted in our lab in collaboration with Ford Otosan (2019). For this reason, we decided to build our own current-mode universal LED driver. The driver is simply connected in series between the main vehicle battery and the LED head/tail light and provides both illumination and communication. A picture of the driver and its layout are provided in Fig. 2.3.

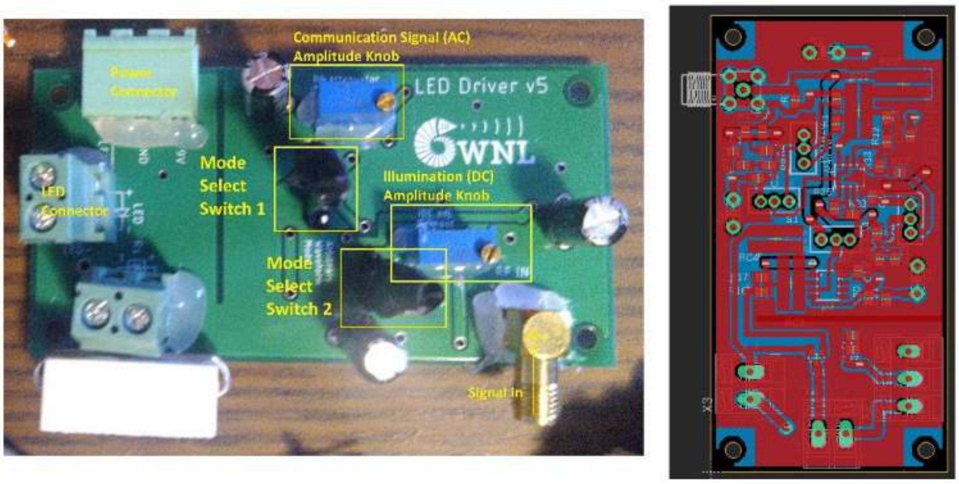

Figure 2.3: Prototype vehicular VLC TX LED driver developed in our lab in collaboration with Ford Otosan [Soner et al., 2020].

This universal driver can be customized for different LEDs (at its output) and for different signal generators (at its input) by changing the value of the shunt resistor (white block, bottom left on the picture) and by adjusting the mode select switches, as will be described. The schematic for the driver is in Fig. 2.4.

The main working principle of the driver circuit is as follows: The ground-referenced voltage input to the circuit (through the SMA connector) acts as a reference for the feedback loop which controls the current flowing over the LED. This signal input can come from various sources including Universal Software Radio Peripherals (USRP) and arbitrary waveform generators. The drive op-amp (lower

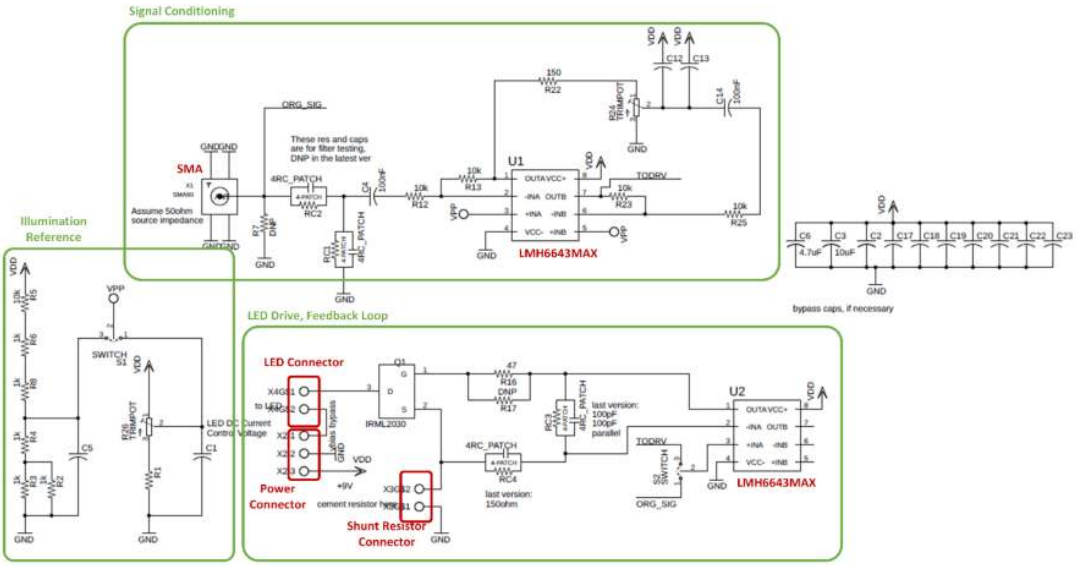

Figure 2.4: Schematic for the prototype driver in Fig. 2.3.

LMH6643MAX in Fig. 2.4) compares the voltage on the shunt resistor to the input reference voltage and drives the gate of the MOSFET (IRML2030), which realizes a current through the LED. Since there is no signal conditioning on the feedback signal from the shunt resistor (only a simple compensator, no level shift), assuming stable operation, at steady state, the realized current is the reference voltage divided by the shunt resistance. However, there are two modes for connecting the input signal to the drive circuit: the input signal can be regarded as AC-coupled and can be added on top of a DC illumination signal before feeding the drive circuit (mode A) and the input signal can be fed directly to the drive circuit as an arbitrary waveform (mode B). In mode A, a switch selects between a variable DC illumination controlled with a trim-pot versus a fixed illumination (i.e., center point of allowable range, 1V/shunt resistor). The variable illumination trim-pot allows for adjusting for both the maximum signal swing (note that the maximum of the DC+AC signal should not exceed LED limitations) and for illumination restrictions.

The AC-coupled + fixed DC illumination (mode B) was predominantly used for the USRP experiments with most LEDs in our lab (only exception is unipolar OFDM experiments where the signal was not actually AC-coupled). The arbitrary

Figure 2.5: Our prototype drivers on the fog lights of the Fiat Linea in our lab.

waveform mode was predominantly used for LED characterization with narrow pulse widths (<20ns). As an example: in the AC-coupled + fixed DC illumination mode, with a 3.3 Ω shunt resistor, the DC illumination current without any signal input is 1 V / 3.3 Ω ≈ 300 mA. Assuming a sinusoidal input signal with an amplitude of ±1V (such as a USRP output on a 1 MΩ load), the 0V point gets translated to the DC illumination point (1 V) and the signal swings in the 0 V - 2 V range, corresponding to a positive illumination for all time instants. This complies with the unipolar signaling principle in VLC: VLC signals can only have a positive sign since the intensity of light is modulated rather than the electromagnetic field itself, as in RF communications, and the intensity of light is positive definite.

The driver itself (without connection to an LED) was observed to provide a flat (±1 dB) frequency response from baseband up to 10 MHz and a ≈ -10 dB/decade decaying response after 10 MHz. This is desired behavior since the flat band of the driver is much wider than most commercially available high-power LEDs and thus for

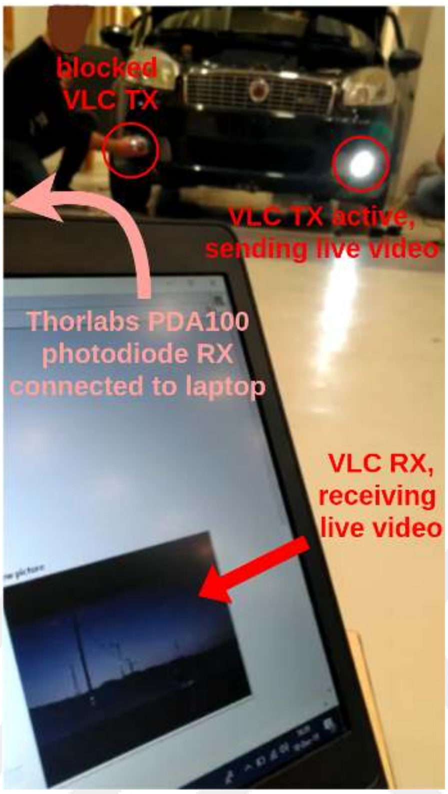

Figure 2.6: Video streaming using our prototype drivers at 880 kbps. One TX blocked just to show that the two TX signals match.

frequencies over ≈1-2 MHz, the LED response dominates; the driver therefore only acts like a wideband amplifier. While the driver gets supplied from the 12 V main vehicle battery, it requires a step-up converter in between since the shunt resistor and the MOSFET drain-source terminal requires finite potential differences during operation. To address this, an additional power supply unit capable of supplying two LED lights (fog lights on a Fiat Linea) and USRP units with a connection to the main 12V vehicle battery was developed, as shown in Fig. 2.5. During performance testing, the custom driver + Linea LED fog light setup achieved a reliable communication rate of 880 kbps over a distance of approximately 20 m in a parking garage scenario. To demonstrate this capability we streamed a live video feed from the Linea fog lights to a laboratory grade photodiode receiver (Thorlabs PDA100) connected to a laptop in LabView environment, as shown in Fig. 2.6.

2.2 Vehicular VLC Receivers

Vehicular VLC receiver design is much less constrained compared to TX unit design since there are effectively no regulations that limit applicable technologies. The optical and electrical configurations used for vehicular VLC receivers and their placement on the vehicle are still open research topics [Eldeeb and Uysal, 2019]. While there are many different types of optical detectors that have previously been used as VLC receivers in non-vehicular indoor and outdoor domains such as silicon or GaAs photodiodes, cameras, photomultiplier tubes (PMTs) and solar cells [Turan et al., 2019], only photodiode-based receivers are suitable for vehicular VLC and VLP in collision avoidance and platooning applications. More specifically, PMTs, which enable amplification of a single photoelectron to series of electrons with gains up to 100 million units, are unsuitable because they are very sensitive to ambient light [Liu et al., 2016]. Solar cells provide opportunity for simultaneous energy harvesting and communications, but detector device and read-out circuit design and for those two tasks are conflicting, and results in sub-optimal communication performance compared to even simple silicon p-i-n photodetectors [Wang et al., 2015]. Camera-VLC approaches are also not suitable since they either provide very low (<kbps [Căilean and Dimian, 2017]) communication rates [Yamazato and Haruyama, 2014] or require costly high-frame-rate cameras [Yamazato et al., 2014], which beats the purpose of using VLC and VLP as low-cost and low-complexity complementary technologies.

On the other hand, photodiode-based VLC receivers (both p-i-n and avalanche types) are suitable for the applications of interest here since they provide higher bandwidth communication without significant additional cost or complexity, thus, allow for shifting system complexity to more important functionalities [Memedi and Dressler, 2020, Gonçalves et al., 2021]. Various front-end designs that explore different optical and electrical trade-offs exist for photodiode-based VLC receivers. Some interesting examples include angular diversity optical configurations that unlock multiple-input-multiple-output VLC systems [He et al., 2019], designs utilizing blue filters to boost reliable channel bandwidth by canceling the slow phosphorescent modulated intensity component coming from LEDs [Stepniak et al., 2015], designs that use imaging optics to improve receiver field-of-view [Kahn et al., 1998], and electronics designs that adapt to the changes in the environment (e.g., via automatic gain control to control saturation) [Căilean and Dimian, 2016, Căilean et al., 2020]. We discuss existing optical designs for vehicular VLC receivers in Chapter 3 for motivating our own receiver design, the "QRX". We assume photodiode-based vehicular VLC receivers in the rest of the discussions in this thesis.

2.3 VLP: Relative Vehicle Positioning using VLC Signals

This section first presents the vehicular VLP system model which considers the use of VLC signals exchanged between TX and RX units on two vehicles for the relative positioning of those vehicles, then defines the associated vehicular VLP positioning problem, and finally describes the mathematical model of the received vehicular VLC signals that are used in this process.

2.3.1 System Model Assumptions

The system model is based on the following assumptions for collision avoidance and platooning applications ($A\#$):

- *A1:* Vehicles cruise on piecewise-flat roads, i.e., their pitch angles with the horizon is the same. This assumption, which reduces the 3D positioning problem to 2D (i.e., the road plane), is reasonable for collision avoidance and platooning scenarios where vehicles are within 1-20 m of each other driving at $\geq$30 km/h [Kusano and Gabler, 2012b, American Association of Highway and Transportation Officials (AASHTO), 2011b].

- *A2:* Vehicles contain VLC units with LED TXs and photodiode-based RXs on their head and tail lights (i.e., 4 VLC units in total), sustaining reliable LoS communication. A minimal setup (2 RXs on each face) is assumed to assess worst case performance, and TX separation distance is assumed to be equal to RX separation distance L for simpler analysis, without loss of generality.

- *A3*: VLC TX units are assumed to be point sources. This assumption holds for the intended applications since the photometric distance for vehicle LED head/tail lights (a maximum of approximately 50 cm [IALA E-122, 2001, Ma et al., 2019, Jacobs et al., 2015]), is smaller than the 1 m minimum distance between the vehicles considered in (*A1*).

- *A4:* Transmissions by the VLC units do not interfere. This can be achieved via special medium access control mechanisms, e.g., by assigning each unit to a separate transmission frequency band [Wu et al., 2002].

We call the vehicle that is being positioned the "target vehicle", and the vehicle that is estimating the position the "ego vehicle". Fig. 2.7 depicts this system model for the case of a target vehicle (green) being followed by an ego vehicle (red). However, both vehicles can take either role at a given time, in any orientation, since they have the same configuration.

2.3.2 Vehicular VLP Problem Definition

Vehicular VLP methods use RX VLC signals to estimate TX relative positions, which are denoted as $(x_{ij},\ y_{ij})$ in this thesis with regards to the indices $i, j \in \{1, 2, 3, 4\}$ for vehicular VLC RXs and TXs, respectively. For determining the exact 2D relative location of the target vehicle, positioning two TX units on the target vehicle with respect to two RX units on the ego vehicle is necessary. However, since the two ego RX units are, by definition, simply separated by L in the lateral axis of the ego frame of reference, estimating positions with respect to only one RX is sufficient, e.g., only (x_{11}, y_{11}) and (x_{12}, y_{12}) for RX 1 in Fig. 2.7. For this reason, the i subscript in $(x_{ij},\ y_{ij})$ can be dropped when describing TX position coordinates,

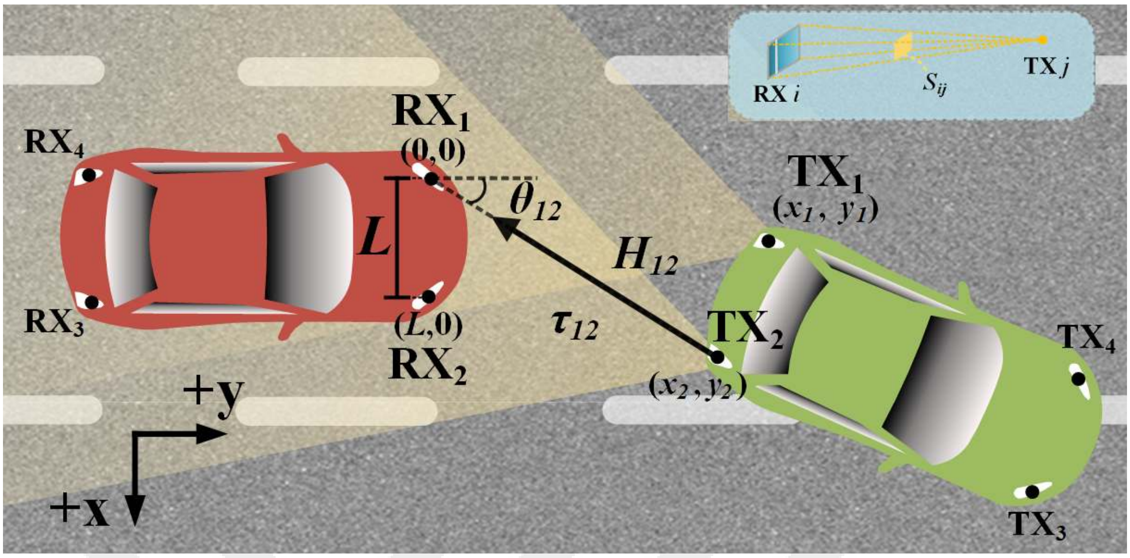

Figure 2.7: System model: The ego vehicle (red) estimates the 2D relative positions of two VLC TXs on the target vehicle (green), i.e., (x_1, y_1) and (x_2, y_2), for vehicle localization. Channel characteristics between TX 2 and RX 1 are depicted as an example: H_{12} is the channel gain, τ_{12} is the propagation delay and θ_{12} is the AoA from TX 2 to RX 1. S_{ij} is the angle subtended by RX i with respect to point source TX j, and L is the RX separation.

i.e., $(x_j,\ y_j) = (x_{1j},\ y_{1j})$ for TX j, $j \in \{1, 2\}$, as in Fig. 2.7. Additionally, if vehicles are longitudinally parallel, the following dependency relationship holds: $(x_2, y_2) = (x_1 + L,\ y_1)$, and estimating only one position independently, i.e., estimating (x_1, y_1), is sufficient.

Accordingly, although estimating position for the two TX units is necessary for completely characterizing localization performance, analyses in this thesis will show results and derivations for only one TX due to the following reasons: 1) Extending the analyses to a second TX is straightforward, 2) the position estimation error for one TX does not differ significantly from that of the other due to the physical proximity between the two, and 3) this allows fair comparison with methods that assume longitudinally parallel vehicles (e.g., [Roberts et al., 2010]) which converge to the closest solution that satisfies the parallel assumption even when the actual orientations of vehicles do not. Therefore, estimation error is defined as:

$$e = \sqrt{(x_1 - \widehat{x_1})^2 + (y_1 - \widehat{y_1})^2}\ , \tag{2.1}$$

where $(\widehat{x_1},\ \widehat{y_1})$ is the position estimation for TX 1 ($\widehat{\ }$ denotes measured or estimated quantities in the rest of the text), and e is the associated error for a given estimate. However, since the vehicles are in continuous relative movement and localization occurs at a finite rate, such a static accuracy definition is not sufficient, and rate should also be considered in determining the localization performance.

Let f_u be the localization rate and $T_u = 1/f_u$ be the localization update period, i.e., the time between the k^{th} and the $(k+1)^{\text{th}}$ estimate, where $k \in \{0, 1, 2, ...\}$. Localization accuracy continuously varies since the relative target location does not stay constant between consecutive estimates; this is illustrated with exaggeration in Fig. 2.8c. Assuming that an estimate at time $t = kT_u$ has sufficient accuracy for the location at $t = kT_u$, f_u needs to be higher than $\nu_u/(10\ cm)$ for ensuring cm-level accuracy until the next estimate at $t = (k+1)T_u$, where ν_u is the relative target speed. To satisfy this in most feasible collision avoidance and platooning scenarios, f_u should be at least 50 Hz, constituting the associated requirement for estimation rate [Vandi et al., 2013, Shladover and Tan, 2006]. Accordingly, the maximum e value within the interval $t = kT_u$ to $t = (k+1)T_u$ should be considered as the error for an estimation period. Furthermore, since the main source of error in this system alongside the mobility-induced error is VLC channel noise, which is random, a distribution of e values sampled over the noise process should be evaluated rather than individual e samples. Therefore, the term "cm-level accuracy" in this thesis refers to the distribution of e having one standard deviation above the mean smaller than 10 cm (note that in the zero-mean case (i.e., unbiased estimation), this corresponds directly to standard deviation being less than 10 cm). This vehicular VLP problem definition is depicted in Fig. 2.8.

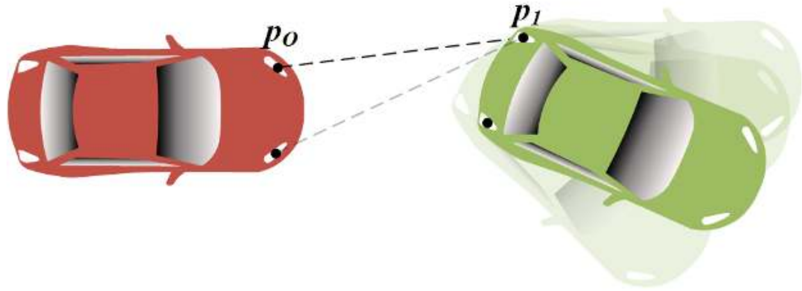

(a) 1 TX position → indefinite but bounded location set

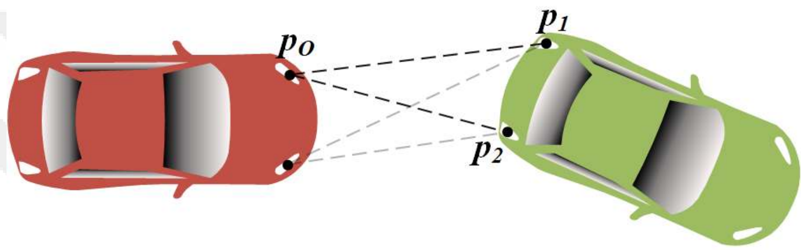

(b) 2 TX positions → definitive vehicle localization

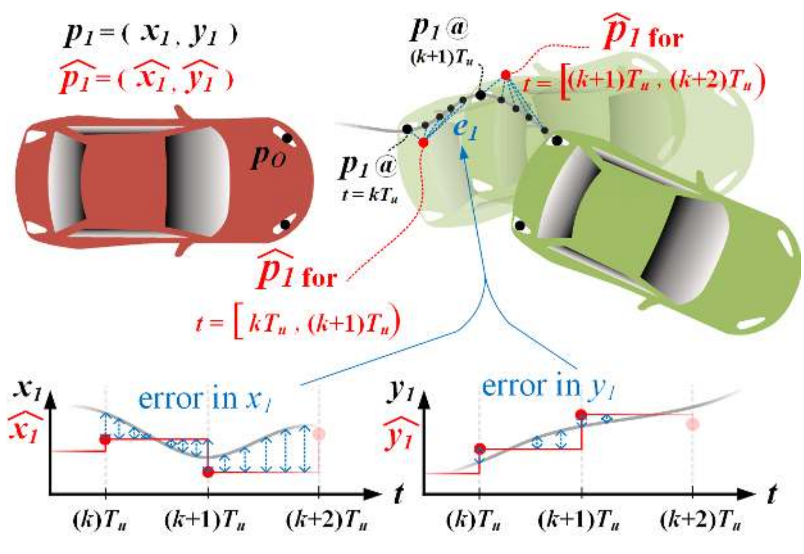

(c) Accuracy and rate jointly determine localization performance

Figure 2.8: Problem definition. p_1, p_2 and $\widehat{p_1}$, $\widehat{p_2}$ are actual and estimated positions for TX 1, TX 2, respectively, relative to the ego vehicle origin, p_O.

2.3.3 Mathematical Model of Received VLC Signals

The following received VLC signal model is considered:

$$r_i(t) = \sum_j r_{ij}(t) + \mu_i(t) \quad , \quad r_{ij}(t) = H_{ij} \cdot s_j(t - \tau_{ij}) \tag{2.2}$$

where t is time, r_i is the total received photocurrent signal, s_j is the transmitted photocurrent signal, r_{ij} is the contribution of s_j to r_i, μ_i is the photocurrent AWGN, and H_{ij} and τ_{ij} are respectively the geometric channel gain and the finite propagation time from TX j to RX i. Since TX signals are directional, only two TXs on a given face of the target vehicle contribute to Eqn. (2.2) for a given RX on the ego vehicle, i.e., j is either $\in \{1, 2\}$ or $\in \{3, 4\}$ for a given $i \in \{1, 2, 3, 4\}$ depending on vehicle orientation, and the two TX components arriving at RX i can be processed separately as r_{ij} in Eqn. (2.2) as per assumption (*A4*).

Expressions for H_{ij}, τ_{ij} and μ_i rely on the point-source approximation of TXs from the perspective of RXs: The minimum RX-TX distance at which the inverse square law for received optical power for point-sources starts to hold (i.e., photometric / far-field / cross-over distance) is ≈50 cm for automotive LED lights [IALA E-122, 2001, Ma et al., 2019, Jacobs et al., 2015]. Since this is smaller than the 1 m minimum distance assumed in *A1*, TXs are assumed as point sources in this thesis (*A3*), which simplifies expressions for H_{ij} and τ_{ij}, and indirectly, also μ_i. Accordingly, the channel gain H_{ij} can be expressed as:

$$H_{ij} = \gamma_i \rho_i(\theta_{ij}) \iint_{S_{ij}} \gamma_j \rho_j(S) \; dS \; , \; S_{ij} \propto \frac{A_i \cos(\theta_{ij})}{d_{ij}} \tag{2.3}$$

where d_{ij} and θ_{ij} are the relative distance (i.e., range) and AoA (i.e., bearing) of TX j relative to RX i, respectively; ρ_j and ρ_i are the normalized positive-definite TX beam pattern and RX "reception" pattern, respectively; γ_j and γ_i are the TX electrical-to-optical gain and RX optical-to-electrical, i.e., photodiode sensitivity respectively; and S_{ij} is the solid angle subtended by the active area of the RX i ($\triangleq A_i$) with respect to TX j [Mathar, 2015]. Lambertian source models turn Eqn. (2.3) into a closed form expression. However, since non-Lambertian beam patterns can also be used, we provide the more general Eqn. (2.3), which can easily be converted to an approximate Lambertian model when necessary, as done so in [Steendam et al., 2016a, Viriyasitavat et al., 2013, Béchadergue et al., 2016]. θ_{ij} and d_{ij} in Eqn. (2.3), and τ_{ij} in Eqn. (2.2) are expressed as:

$$d_{ij}=\sqrt{{x_{ij}}^2+{y_{ij}}^2} \quad , \quad \theta_{ij}=\arctan\left(\frac{x_{ij}}{y_{ij}}\right) \quad , \quad \tau_{ij}=\frac{d_{ij}}{c} \tag{2.4}$$

where c is the speed of light. μ_i is composed of shot noise on the receiving p-i-n photodetector (PD) and thermal noise on the FET-based front-end transimpedance amplifier (TIA) that follows the PD [Smith and Personick, 1980]. The combined noise is zero mean additive white Gaussian (AWGN) with variance [Kahn and Barry, 1997, Eqn. (18)]:

$$\sigma^2_{\mu_i}=\sigma^2_{shot_i}+\sigma^2_{thermal_i} \tag{2.5a}$$

$$\sigma^2_{shot_i}=2q\gamma_i P_i B_i+2qI_{bg,i}I_{B2}B_i \tag{2.5b}$$

$$\sigma^2_{thermal_i}=4kT_i\left(\frac{1}{R_i}I_{B2}B_i+\frac{(2\pi C_i)^2}{g_i}\Gamma I_{B3}B_i^3\right) \tag{2.5c}$$

where q is the Coulomb electron charge, k is the Boltzmann constant, P_i is the optical signal power on RX i, $I_{bg,i}$ is the background illumination current, B_i is the front-end bandwidth, T_i is the circuit temperature, R_i is the front-end resistance (i.e., TIA feedback gain term), C_i is the input capacitance due to the photodiode and the FET, g_i is the FET transconductance, and Γ, I_{B2} and I_{B3} are unitless factors for FET channel noise and noise bandwidth determined by the signal shape

[Kahn and Barry, 1997]. For an optimal TIA (i.e., proper loop compensation and impedance matching such that bitrate is equal to B_i [Smith and Personick, 1980]), Eqn. (2.5c) is typically reorganized using $R_i = G/(2\pi B_i C_i)$ where G is the "open-loop voltage gain", and the front-end circuit gain is independent of transistor parameters, i.e., R_i determines the transimpedance gain which turns the received photocurrent r_i into a voltage signal.

We ignore the following minor effects: Popcorn noise due to silicon defects are absent in modern components. Flicker, i.e., $1/f$ noise, is also ignored since VLC operation is not near DC. Furthermore, random fluctuations on H_{ij} and τ_{ij} due to atmospheric turbulence are ignored since LEDs are non-coherent. Similarly, Doppler effects, which would make τ_{ij} time-dependent, are also ignored since they were shown to have a negligible effect on positioning performance [Béchadergue et al., 2019].

Chapter 3

QRX: A NOVEL ANGULAR DIVERSITY RECEIVER FOR VISIBLE LIGHT POSITIONING

This section presents the VLP-friendly improvement that we propose to the vehicular VLC physical layer: a novel angle-of-arrival (AoA) sensing VLC RX design named “QRX”, the associated AoA measurement procedure used for positioning purposes, and a proof-of-concept experimental study that validates the QRX optical design. The design promises high-rate communication, and high-accuracy and high-rate AoA measurement, simultaneously, and is also low-cost since it considers commercial-off-the-shelf (COTS) components only, enabling the practical realization of bearing-based vehicular VLP solutions at low cost and complexity.

3.1 Motivation for a New AoA-sensing Receiver

AoA-based VLP methods promise high accuracy without imposing restrictive requirements such as limited vehicle orientations, presence of road-side/traffic lights, and high-bandwidth circuit and VLC modulation constraints [Keskin et al., 2018]. However, their vehicular implementations have so far been limited to camera-VLC based methods, which are not suitable due to low communication rates and the necessity of costly high-frame-rate cameras for high-rate positioning [Yamazato et al., 2014]. Therefore, a low-cost and small-size photodiode-based VLC receiver design that can provide high-rate VLC and high-accuracy, high-resolution and high-rate AoA measurement, is needed.

Existing photodiode-based VLC receiver designs that can be used for AoA measurement fall into four main categories [He et al., 2019]: aperture-based, lens-based, prism-based and tilted-photodiode-based designs. Tilted-photodiode designs

[Zhu et al., 2019a, Arafa et al., 2012, Lee and Jung, 2012a, Lu and Chen, 2013] and special prism-based designs [Wang et al., 2014] are not suitable for vehicular use since they are not low-cost/size and typically provide limited AoA resolution (i.e., coarsely quantized AoA intervals as estimates). Aperture-based designs using commercially available low-cost/size quadrant-photodiodes (originally proposed for angular diversity in multiple-input-multiple-output (MIMO) indoor VLC [Aparicio-Esteve et al., 2019, Cincotta et al., 2017, Kahn and Barry, 1997]) can be used for accurate and resolute AoA measurement but the aperture limits the field-of-view (FoV). Using an imaging architecture, e.g., a lens rather than an aperture, provides larger FoV [Wang et al., 2013a]. Such quadrant-photodiode-based imaging designs, traditionally used for laser target tracking [Carbonneau et al., 1986] and transceiver pointing [Kaymak et al., 2018], are also promising for AoA measurement. A low-cost/size realization of this architecture with commercial-off-the-shelf components would enable the restriction-free AoA-based high accuracy and rate vehicular VLP method. We propose such a receiver design in this chapter.

3.2 QRX Receiver Design

A conceptual diagram of the QRX and its optical configuration are shown in Fig. 3.1 and a prototype of the QRX built by our group with low-cost COTS components is shown in Fig. 3.2. The design of the QRX is inspired by the MIMO VLC RX in [Wang et al., 2013a] but the QRX is specifically designed for high-resolution AoA measurement in VLP rather than simply achieving angular diversity. The QRX contains a plano-convex lens placed at a certain distance above a quadrant photodiode (QPD), converging the rays from the TX LED into a defocused spot. The spatial irradiance distribution on the QPD due to the spot, which depends on AoA by the ray optics relations that define $\rho_i(\theta_{ij})$ in Eqn. (2.3) for each quadrant, determines the received signal power on each quadrant as depicted in Fig. 3.1. Let f_{QRX} be the function that relates the AoA from TX j to QRX i, i.e., θ_{ij}, to the signal power ratio for signal s_j from TX j between horizontally separated quadrants, Φ_{ij}, by

$$\Phi_{ij} = f_{QRX}(\theta) = \frac{(\epsilon_{ij,B} + \epsilon_{ij,D}) - (\epsilon_{ij,A} + \epsilon_{ij,C})}{\epsilon_{ij,A} + \epsilon_{ij,B} + \epsilon_{ij,C} + \epsilon_{ij,D}} \ , \tag{3.1}$$

where $\epsilon_{ij,q}$ represents the power of the received signal in quadrant $q, q \in \{A, B, C, D\}$ of QRX i, and Φ_{ij} is bound to the [-1, 1] interval by definition. Choosing an f_{QRX} function is the main task in QRX design since the inverse of f_{QRX}, which we call g_{QRX}, is used for measuring θ_{ij}; g_{QRX} is computed to sufficient precision by ray optics simulations offline and is stored as a look-up table on the ego vehicle.

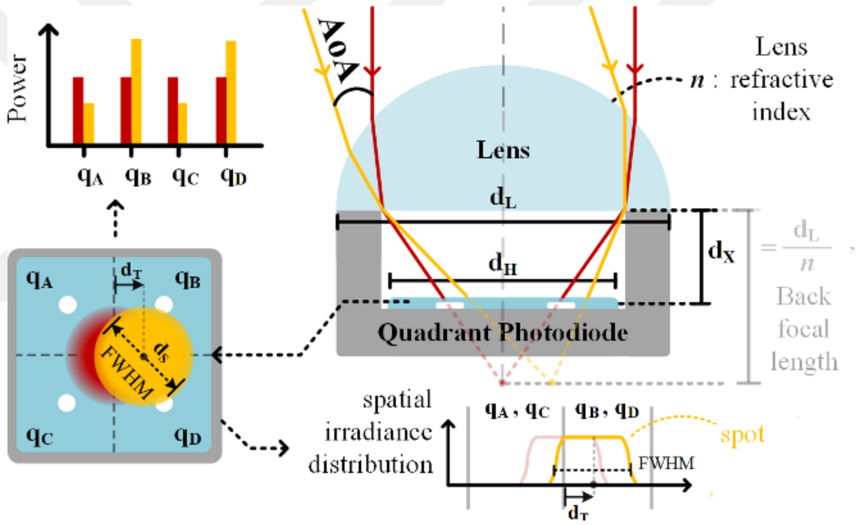

Figure 3.1: Diagram of the AoA-sensing VLC RX, i.e., QRX. The red and yellow colors represent conditions for zero and non-zero AoA, respectively.

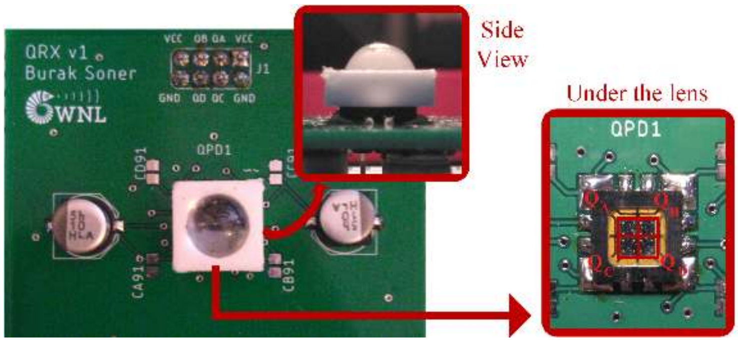

Figure 3.2: Picture of the QRX prototype.

f_{QRX} is determined by the size of the spot and the range of its displacements from the QPD center due to non-zero θ_{ij}: Both are determined by the optical configuration parameters, i.e., lens diameter, lens refractive index, QPD size and lens-QPD distance, denoted by d_L, n, d_H, d_X, respectively, as also shown in Fig. 3.1. In the following, we first provide design principles for the QRX based on first order optics [Sasián, 2019], and then verify our design procedure with a realistic ray optics simulator that takes lens thickness, reflection and Fresnel losses into account and uses design files for real lenses from the Edmund Optics catalog.

Regarding the first order principles, d_L, n and d_X determine the size of the spot denoted by d_S, the full-width at half-maximum (FWHM) of its intensity distribution, which is computed by [Edmund Optics, 2019]:

$$d_S = \frac{(d_L)(d_L/n - d_X)}{d_L/n} = d_L - (n)(d_X) \ . \tag{3.2}$$

This holds as long as the spot is approximately uniform, which is mostly the case for relatively thin lenses since 1) the QRX subtends a very small portion of the total non-uniform TX beam, thus, the beam arriving at the lens is truncated to an approximately uniform (i.e., "flat-top") intensity distribution [Urey, 2004], and 2) the flat-top distribution experiences negligible diffraction artifacts after the lens since d_X is significantly smaller than d_L/n [Ozaktas and Mendlovic, 1995]. Moreover, d_T, i.e., the displacement of the spot from the QPD center for a given θ_{ij}, is determined by d_X alone, as follows:

$$d_T = d_X \tan(\theta_{ij}) \ . \tag{3.3}$$

The relative magnitudes of d_S and d_H, and the range of d_T values that allow θ_{ij} measurement for a given configuration determine the conformance of f_{QRX} to its design goals, which are: high FoV (ideally $\pm 90°$), high linearity, and bijection, i.e., being one-to-one and onto. The FoV, denoted by θ_{FoV}, is equal to the maximum measurable θ_{ij} value which is determined by a spot displacement of $d_T = d_S/2$ as per Eqns.

(3.2) and (3.3), i.e., $\theta_{FoV} = \pm \arctan(d_S/(2d_X))$, since all θ_{ij} outside the $\pm\ \theta_{FoV}$ interval result in $|\Phi_{ij}| = 1$ due to two of the four quadrants receiving zero signal power, which renders θ_{ij} measurement impossible. Hence, larger d_S or smaller d_X provides larger FoV, however, this degrades linearity [Carbonneau et al., 1986]. Furthermore, $d_S > d_H\sqrt{2}$ violates bijection since in such configurations, all quadrants remain completely within the effective spot area and receive equal signal power for $|d_T| \approx 0$ [Manojlović, 2011], i.e., θ_{ij} values around zero become undetectable since they all result in $\Phi_{ij}=0$, as in the blue curve in Fig. 3.3. Therefore, recognizing these trade-offs, 1) a lens-QPD pair, i.e., $\{d_L, n, d_H\}$, and 2) the lens-QPD distance, i.e., d_X, should be chosen to obtain the best compromise for the three design goals.

3.2.1 Choosing a lens-QPD pair

The primary objective while choosing a lens-QPD pair is ensuring bijection. First, a low-cost and high-bandwidth COTS QPD is chosen to set d_H. Then, a lens is chosen to set d_L and n such that $d_S < d_H\sqrt{2}$ is ensured: Since $\{d_L, d_X, d_S, n\} > 0$ in Eqn. (3.2), d_L upper-limits d_S, thus, setting $d_L < d_H\sqrt{2}$ guarantees bijection alone and makes n a free parameter. Hence, a large d_L that satisfies $d_L < d_H\sqrt{2}$ is chosen to also avoid constraining d_S, thus, the FoV, and n is chosen solely with regards to low cost.

3.2.2 Choosing the lens-QPD distance

After setting $\{d_L, n, d_H\}$, d_X is chosen to set d_S as per Eqn. (3.2) for the best compromise between FoV and linearity. $d_H < d_S$ provides the highest FoV but the mapping is highly non-linear (red curve in Fig. 3.3). $d_S \approx d_H$ still results in high FoV ($\approx\pm 80°$) and milder non-linearity (yellow curve in Fig. 3.3). While $d_S < d_H$ linearizes the full dynamic range (green curve in Fig. 3.3), this radically decreases the FoV [Carbonneau et al., 1986, Steendam et al., 2016a], thus, is not desirable. Therefore, $d_X \approx (d_L - d_H)/n$ is chosen since $d_S \approx d_H$ provides the best compromise, where $d_L < d_H\sqrt{2}$ to ensure bijection.

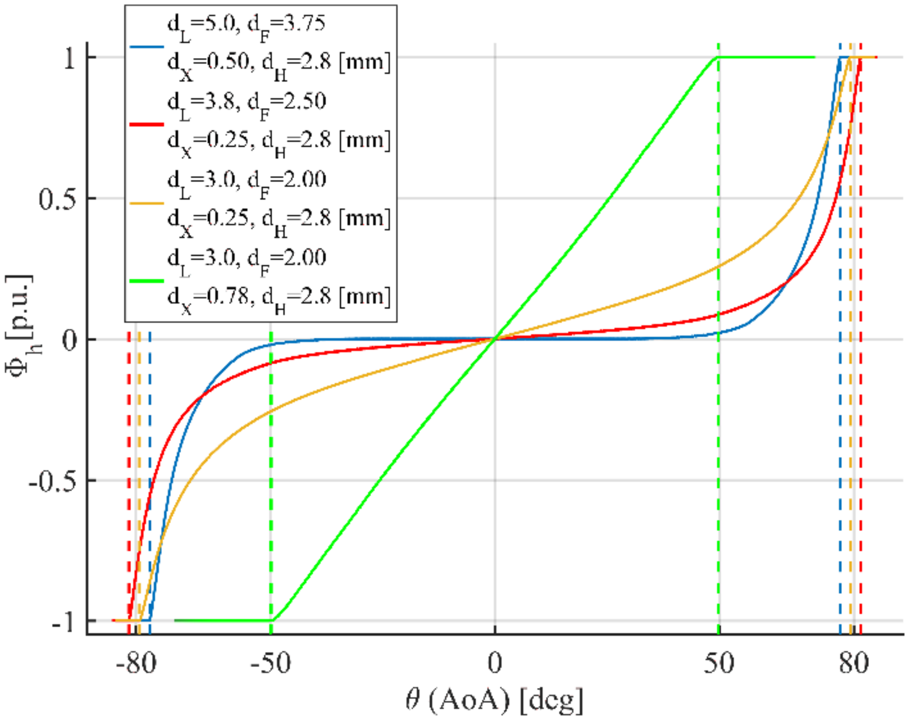

Figure 3.3: Representative f_{QRX} curves for different example configurations using first order design. Yellow curve provides the best compromise for the three design goals: bijection, high FoV and minimal non-linearity. Blue curve is not bijective, red curve is bijective does not use the dynamic range effectively due to aggresive non-linearity, and the green curve is linear but has low FoV.

3.2.3 Design Verification with Ray Optics Simulations

Although the first order principles described in the previous sections guide QRX design to some extent, ray optics simulations with CAD files of actual COTS optical components is necessary for verifying the optical characteristics of the QRX. To this end, we take the CAD files for two lenses from the Edmund Optics Catalog (8.0mm Diameter N-BK7 Half-Ball Lens #45-936, and 9.0mm Dia. x 90.0mm FL Uncoated Plano-Convex Lens #67-149) and conduct ray optics simulations [1] to compute f_{QRX} for QRX setups that these lenses and tune d_X and aperture stop

[1]We use an extended version of the "*mjhoptics/ray-optics*" package for the simulations that takes reflection and Fresnel losses into account as described in this link.

size (corresponds to sensor size) to meet the design requirements. The pictures of the two lenses and the resulting f_{QRX} curves are shown in Fig. 3.4. Both designs have an aperture stop diameter of 6.3 mm, and the d_X values are 0.55 mm and 1.90 mm for the hemispherical and plano-convex setups, respectively. The results show that the plano-convex lens is a much better fit for the QRX design since it provides bijection, better linearity and higher FoV. The hemispherical design fails to provide better performance because its aggressively curved surface reflects much of the rays arriving at the lens surface at high entrance angles, creating excessive loss; this effect, which does not manifest itself in the first order analysis where relatively thin lenses and uniform spots are assumed, makes the hemispherical lens a bad choice for the QRX.

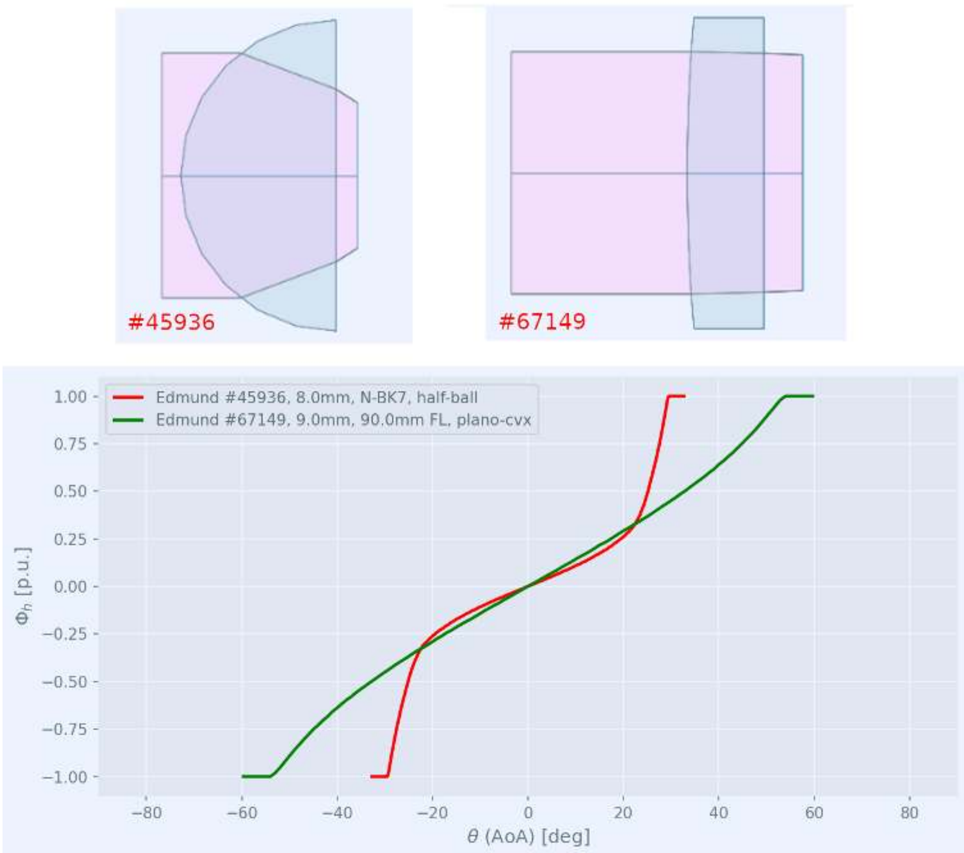

Figure 3.4: Simulated f_{QRX} curves for the two QRX designs using hemispherical and plano-convex lenses, respectively. The plano-convex design is a much better fit.

3.3 Angle-of-Arrival Measurement with the QRX

For measuring AoA from TX j to QRX i, first, the quadrant readings, i.e., the voltage signal produced by the TIA after amplifying r_i for each quadrant q, are sampled at the Nyquist rate of the TX VLC waveform s_j, i.e., $1/T_s$, where T_s is the sampling period. Then a number of h_{buf} samples are buffered, which are used for both communication and AoA measurement purposes as follows: The VLC subsystem first demodulates the buffered noisy samples for obtaining the communication symbols. Then, it re-modulates the symbols to generate clean samples $\widehat{s_j}[w]$, which represent the contribution of s_j in each buffer sample; $\widehat{s_j}[w]$ are used for estimating the signal power for s_j on each quadrant of QRX i, i.e., $\epsilon_{ij,q}$, where $q \in \{A, B, C, D\}$, as $\widehat{\epsilon_{ij,q}}$ by:

$$\widehat{\epsilon_{ij,q}} = \frac{1}{h_{buf}} \left(\sum_{w=w_0}^{w_0+h_{buf}-1} \left(Q_{i,q}[w]\right) \left(\widehat{s_j}[w]\right) \right) , \tag{3.4}$$

where w_0 marks the sample time at the beginning of the buffer, and $Q_{i,q}[w]$ is the reading sample in quadrant q at time wT_s. The estimations $\widehat{\epsilon_{ij,q}}$ are used for obtaining the AoA measurement, i.e., $\widehat{\theta_{ij}}$, as follows:

$$\widehat{\theta_{ij}} = g_{QRX} \left(\frac{(\widehat{\epsilon_{ij,B}} + \widehat{\epsilon_{ij,D}}) - (\widehat{\epsilon_{ij,A}} + \widehat{\epsilon_{ij,C}})}{\widehat{\epsilon_{ij,A}} + \widehat{\epsilon_{ij,B}} + \widehat{\epsilon_{ij,C}} + \widehat{\epsilon_{ij,D}}} \right) . \tag{3.5}$$

Eqns. (3.4) and (3.5) provide successful AoA measurement based on the following principle: Since $Q_{i,q}[w]$ are samples for r_i which consist of the signal component and zero-mean AWGN as per Eqn. (2.2), the product $(Q_{i,q}[w])(\widehat{s_j}[w])$ results in a factor of the actual signal power scaled by the channel gain and contaminated by AWGN where the channel gain is not known. However, since Eqn. (3.5) considers a ratio of the estimated signal powers for each quadrant and the ratio values are tabulated for different AoA values, AoA measurement is possible even without knowing the exact channel gain as long as the ratio values are unique (i.e., f_{QRX} is bijective). Furthermore, note that this measurement procedure does not dictate shape or bandwidth limitations for s_j, thus, does not impose any restrictive requirements. The only requirement, as also denoted in assumption (*A2*), is that the VLC subsystem successfully demodulates the received signal and generates samples $\widehat{s}_j[w]$.

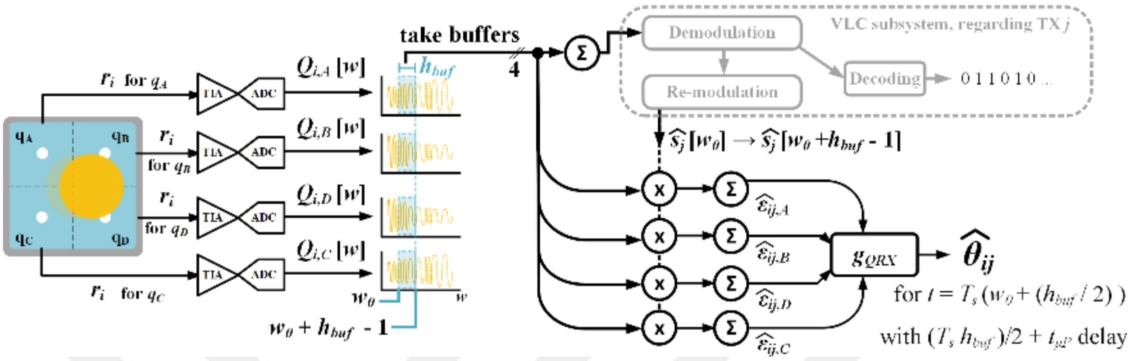

Figure 3.5: Measurement procedure for AoA of TX j to QRX i. Photocurrent received signals at each quadrant, $r_{i,q}$, $q \in \{A, B, C, D\}$, are converted to voltage signals via TIAs and sampled via ADCs to obtain the quadrant readings $Q_{i,q}[w]$, for sample time w. An h_{buf} number of buffered samples are used for de/re-modulating the VLC TX signal to get $\widehat{s}_j[w]$, estimating $\epsilon_{ij,q}$, i.e., obtaining $\widehat{\epsilon_{ij,q}}$, and then for computing the AoA measurement, $\widehat{\theta_{ij}}$.

Overall, this procedure, depicted in Fig. 3.5, produces AoA measurements for the buffer mid-points, i.e., for time $t = T_s(w_0 + (h_{buf})/2)$ due to the non-weighted averaging operation in Eqn. (3.4), and the measurement rate is determined by h_{buf}, i.e., $f_u = 1/(T_s \cdot h_{buf})$, since w_0 is incremented by h_{buf} for consecutive measurement cycles. However, since the time at which a measurement becomes available is $t = T_s(w_0 + h_{buf}) + t_{\mu P}$ due to buffering and a finite processing time of $t_{\mu P}$, the measurement has a fixed delay of $(T_s \cdot h_{buf})/2 + t_{\mu P}$. Despite this delay, the AoA measurement can be done in real-time: The first term, $(T_s \cdot h_{buf})/2$, is negligible when rate is higher than 50 Hz as discussed in the problem definition. The second term, $t_{\mu P}$, which relates to the computational complexity of the procedure, is computed by:

$$t_{\mu P} = \overbrace{T_{FP}\left(k_\alpha h_{buf}\left(\log_2(h_{buf})\right) + k_\beta\right)}^{t_{VLC}} + \overbrace{T_{FP}\left(2h_{buf} + h_{LU}\right)}^{t_{VLP}}, \tag{3.6}$$

where t_{VLC} is VLC demodulation and re-modulation time, $(k_\alpha,\ k_\beta)$ are scalars to account for implementation-specific variations of the FFT-based modulation complexity, t_{VLP} is the VLP processing time, h_{LU} is the number of operations required for the g_{QRX} table look-up, and T_{FP} is the processor clock period. Considering modern processor speeds, known FFT-based modulation techniques [Baltar et al., 2011], and a T_s of 1 μs and 50 Hz rate in the worst case (i.e., $h_{buf} = 1/(50 \cdot 10^{-6}) = 20.000$) , $t_{\mu P}$ is only around a few μs, which is also negligible.

The accuracy of the AoA measurements is affected by two main factors: AWGN on the quadrant reading samples $Q_{i,q}[w]$, and the integrity of the samples $\widehat{s_j}[w]$ generated by the VLC subsystem. Since $\widehat{s_j}[w]$ does not have exact information on H_{ij}, it cannot track the RX signal envelope within the buffer, which means that considering Eqn. (3.4), $\widehat{\epsilon_{ij,q}}$ estimation, thus, AoA measurement, may not be exact for a non-constant signal envelope throughout an estimation cycle; this is depicted with exaggeration in Fig. 3.6. However, this effect, which is due to target vehicle movement within the buffer time interval, never becomes significant in practice since even the fastest vehicle transients, which are around 50 ms because of high inertia [Vandi et al., 2013], do not fit within a single buffer time interval, which needs to take less than 20 ms considering the greater than 50 Hz rate requirement. Therefore, AoA measurements are contaminated predominantly by the AWGN on the VLC channel.

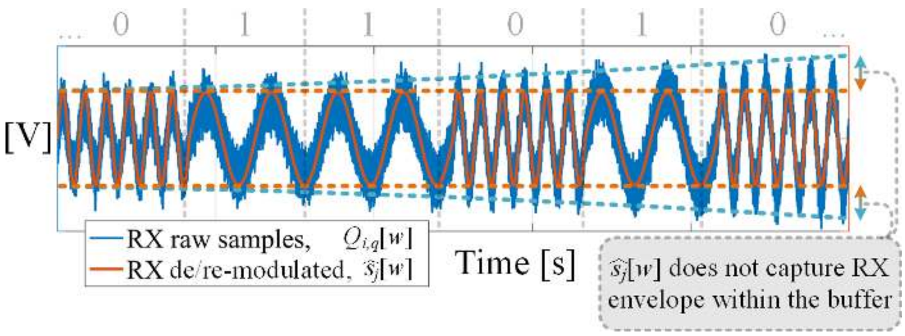

Figure 3.6: Exaggerated depiction of the "envelope effect" on $\widehat{s_j}[w]$ and $Q_{i,q}[w]$ for a single buffer with binary frequency shift keying modulated samples as an example.

3.4 Proof-of-Concept Study: VLC Beam Tracking with QRX

To experimentally verify the QRX design concept, we conduct a proof-of-concept study in which we use the QRX as a beam tracker for physically secure VLC (i.e., TX beam is highly directional, does not spill outside the RX region). Showing that the QRX works with low-cost COTS components in this mode of operation, which is how quadrant-photiode based detectors are traditionally used (e.g., laser target tracking [Carbonneau et al., 1986] and transceiver pointing [Kaymak et al., 2018]), proves that the QRX will also be able to carry out the AoA measurement task since the only difference between the two modes is software manipulation. Therefore, although this study does not quantify AoA measurement accuracy, it is an important verification step for QRX design.

As an example application for this physically secure VLC transceiver (TRX) enabled by the QRX, we describe UAV VLC communications and the role QRX can take there for signal reception and tracking-pointing-alignment. To this end, this section initially discusses the system model for medium-range (<100 m) physically secure UAV communications with VLC, presents the design of a QRX-based low-SWaP, low-cost VLC TRX which is feasible for use in this system, and presents full implementation details for a proof-of-concept prototype for this design realized with cheap, COTS components.

3.4.1 Physically Secure UAV VLC with QRX

The abstract system model, depicted in Fig. 3.7, comprises of two UAVs, <100 m apart, which carry VLC TRX with 360°rotation pan-tilt-type gimballed pointing mechanisms [Khan and Yuksel, 2015] capable of synchronous communication with each other as long as energy from the TX beam reaches the RX detector. TRXs contain LEDs with standard radially symmetric polar beam patterns (TX), a QRX for signal reception, associated drivers and optics and the pan-tilt gimbal mechanism that allows for them to point their LED towards the other's photodetector and track each other's LoS throughout their trajectories for sustained communication.

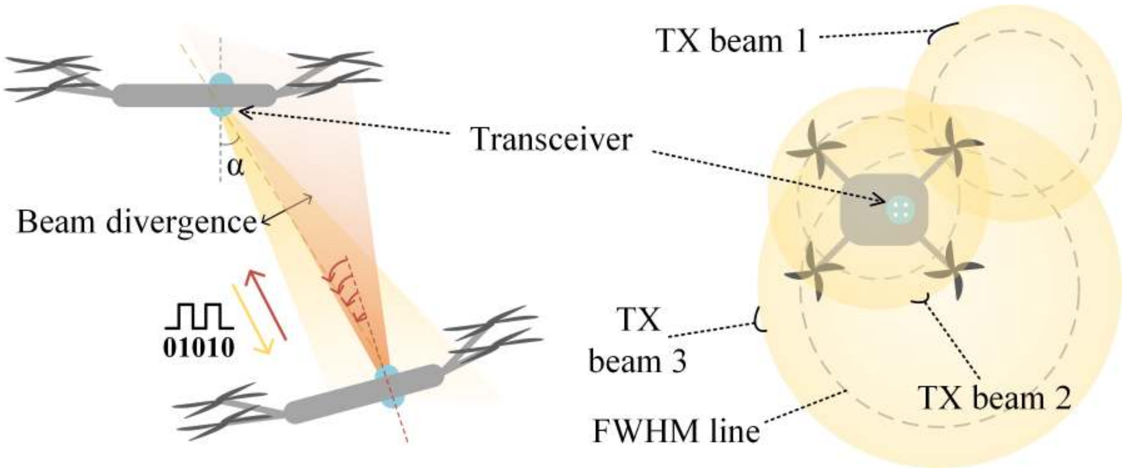

Figure 3.7: Investigated abstract system model for medium-range (<100 m) UAV communications with VLC.

A tracker/pointer (TP) can be considered to have obtained a LoS link if the RX detector stays within the full width at half maximum (FWHM) of the TX beam foot-print on the RX plane, and its accuracy can be measured by how well the beam central axis is aligned with the RX detector surface normal vector. A higher TP accuracy brings higher signal-to-noise-ratio and thus more reliable communication. Furthermore, the physical security level of a beam can be measured by what % of the total energy emanating from the TX falls onto the RX detector. These concepts are demonstrated in Fig. 3.7 where TX beam 1 is not in LoS, beam 3 is in LoS but not very accurate, and beam 2 has the highest accuracy. Beam 2 is also more secure than 3 since a much larger % of the total TX beam falls onto the RX detector, leaking out much less energy for potential eavesdroppers. The most stringent TP accuracy requirement for this system occurs when complete physical security (FWHM of TX beam is fully inside RX detector area) is required at the furthest distance (100 m). This spatial beam confinement requirement, depicted in Fig. 3.8, is common in long-range FSO applications and requires large and costly telescopes and ultra-high precision TP stages for >km ranges since the TP accuracy requirement becomes sub-μrad. The medium-range UAV VLC application can be treated with much lower SWaP and cost solutions since the required accuracy is inherently lower at smaller distances and furthermore the accuracy requirement can be traded for minor compromises in physical security, like shown in Fig. 3.7.

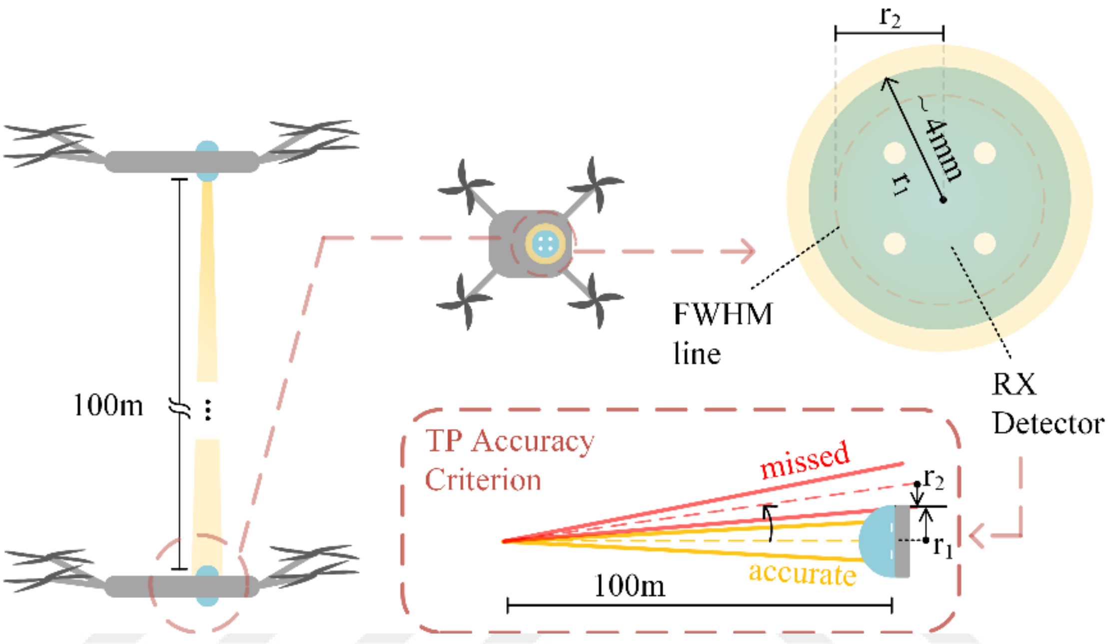

Figure 3.8: Tracking/pointing (TP) accuracy requirements for complete physically security at 100 m.

It is not uncommon for the two TRX to lose LoS due to bad TP or environmental conditions. When LoS is lost between two TRX, an acquisition mechanism is necessary to regain LoS and resume TP for sustained communication. The requirements for acquisition mechanisms vary too much depending on the individual application requirements and are thus left out of this investigation. A summary on state-of-the-art acquisition methods can be found in [Kaymak et al., 2018].

3.4.2 Proof-of-Concept QRX VLC Beam Tracker Demo Setup

We next propose a transceiver which can be used for physically secure VLC between UAVs in <100 m distances as described previously. The low-SWaP and low-cost transceiver utilizes a simple standard VLC TX subsystem and a single QRX on the RX subsystem for both TP and VLC purposes.

Transmitter Subsystem

The TX subsystem of the proposed TRX simply consists of the TX LED, its driver circuitry and beam-shaping optics which is either composed of static lenses for a given beam divergence, or a set of moveable lenses in order to accommodate for different conditions with dynamic beam divergence control. The TX beam contains AC-coupled VLC signals modulated around a DC bias intensity level by methods like Manchester-coded on-off-keying, frequency shift keying or variable-pulse-position to reduce message-content-dependent flicker. This is basically a highly simplified version of our low-cost vehicular VLC TX prototype presented in Section 2.1.1.

QRX-based Receiver

The RX subsystem of the proposed TRX uses the QRX. Rather than sensing the AoA explicitly though, the QRX here is used simply as a differential sensor in the TRX controller which constantly tries to keep AoA at zero by moving the TRX with the pan-tilt and balancing the relative intensity on the QPD cells. To converge the incoming beam onto the QPD as a suitably sized spot, a hemispherical lens is used (since it's very easy to come by), and each QPD cell reading is amplified and fed to the TRX microcontroller for both TP and VLC purposes. Since the VLC signal content of the TX beam is AC-coupled, the QPD amplifier for each cell is also AC-coupled, rejecting the DC ambient noise and conveying the TX signal for that cell as clearly as possible to the microcontroller (MCU). The MCU then uses the QPD readings for both VLC and TP.

Tracking and Pointing with the QRX

Most long-range FSO ATP solutions separate the communication and ATP subsystems since the two require individual optical designs in order to meet the stringent sub-μrad TP requirements. While some previous works have used separate "beacon" beams for TP [Walther et al., 2010], others have used a single beam for both but separated it with beam splitters and processed the beam for the TP PD and the beam for the communication PD separately [Guelman et al., 2004]. These designs address their application's needs, but they have resulted in high SWaP gimballed telescopes with high cost. The simple, single-PD-single-beam TRX design proposed in this section meets the requirements for the application investigated in this section and is low-SWaP and low-cost.

The QRX in the proposed TRX utilizes the TX beam shining on it for both VLC and TP purposes. Using these QPD cell readings, the microcontroller runs one task for VLC and one task for TP. The VLC task takes the sum of the cells, demodulates this to retrieve the VLC message and then responds to the message by modulating the TX LED. The TP task first measures the signal energy on each QPD cell and deduces the position of the TX beam's spot on the QPD x-y frame. Then it commands the pan-tilt to turn the TRX accordingly to align the TX beam center with the QPD center, achieving accurate LoS tracking between the two TRXs. The functional block diagram for complete TRX operation is shown in Fig. 3.9.

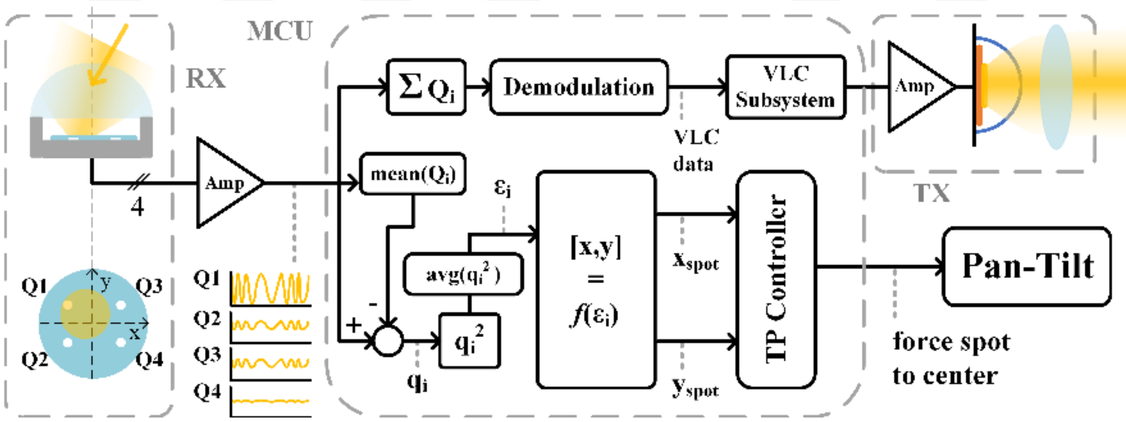

Figure 3.9: TRX functional block diagram. "avg":average.

The signal energy for a certain duration is computed by the TP task by making each QPD reading for that duration zero-mean, taking its square, and calculating the average value of the result. While increasing the duration over which the signal energy is computed brings better robustness against noise, too large a duration slows the controller down. The signal energies are then used for computing the x-y position of the spot on the QPD using the well-known equation for these applications

[Carbonneau et al., 1986], referring to the cell indexing and QPD x-y axis convention shown in Fig. 4. For accurate alignment of the TRX LoS, the spot needs to be exactly on the center of the QPD. The TP controller thus always has a zero reference for x_{spot}, y_{spot} while turning the TRX pan-tilt towards the incoming TX beam center.

Hardware Realization

This section presents a realization of the transceiver proposed in the previous section using completely COTS components and provides in-depth implementation details. The prototype is pictured in Fig. 3.10 and a demo video can be found in [2]. The prototype consists of one small-scale RX and TX unit built as testing platforms for further designs of complete TRXs. Due to the ultra-cheap components used and visible errors in mounting/build (e.g. Fig. 3.10c, lens/QPD axis skew), performance and TP accuracy of this prototype does not reflect the limits of the proposed transceiver. It's merely an example which demonstrates the potential uses of QRX.

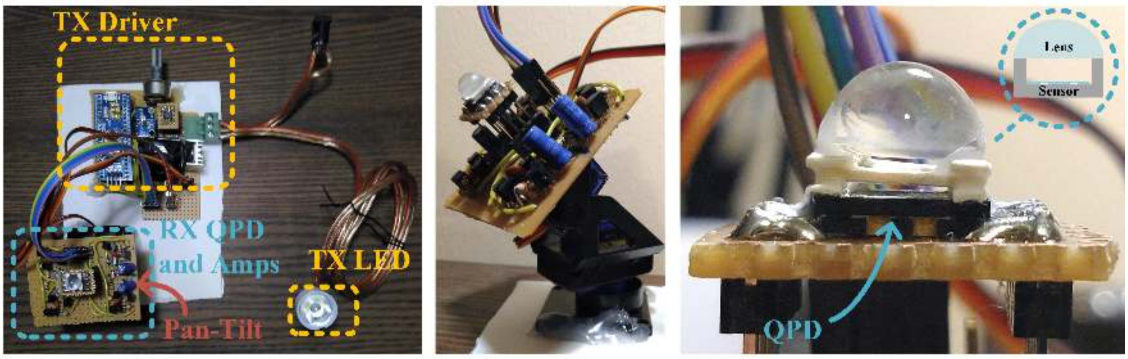

Figure 3.10: Proof-of-concept setup.

The transmitter consists of a standard 3 W white TX power LED, a 5° divergence angle focusing lens and the TX driver electronics. The 5° FWHM beam divergence from the source results in a moderate physical security level (beam radius is 8.7 cm at 1 m distance). While lower divergence beam-shaping optics are possible with more aggressive off-the-shelf lenses, the lens used in this prototype is a parabolic

[2]Demo video of the proof-of-concept prototype: `https://youtu.be/wQPWQB3W_JM`

design with great form factor and holds the LED in place perfectly. The TX driver schematic, the QRX schematic, and the components used in both designs are shown in Fig. 3.11. The operating principle of the TX is the same as the prototype TX in Section 2.1.1. The LED bias (illumination) intensity, around which the modulation waveform swings, was set manually by a 100 kΩ potentiometer on R_1 and R_2 to fully utilize the LED dynamic range without turn-off or saturation/clipping. V_{in} was fed from an AD9833 Digital Direct Synthesizer which generated the binary frequency shift keying waveform that modulated the LED intensity for encoding VLC messages. The binary symbols used were 3 kHz → 0 and 2 kHz → 1 with a bit-rate of 1kbps, and the output voltage swing was 0.7 V pk-pk.

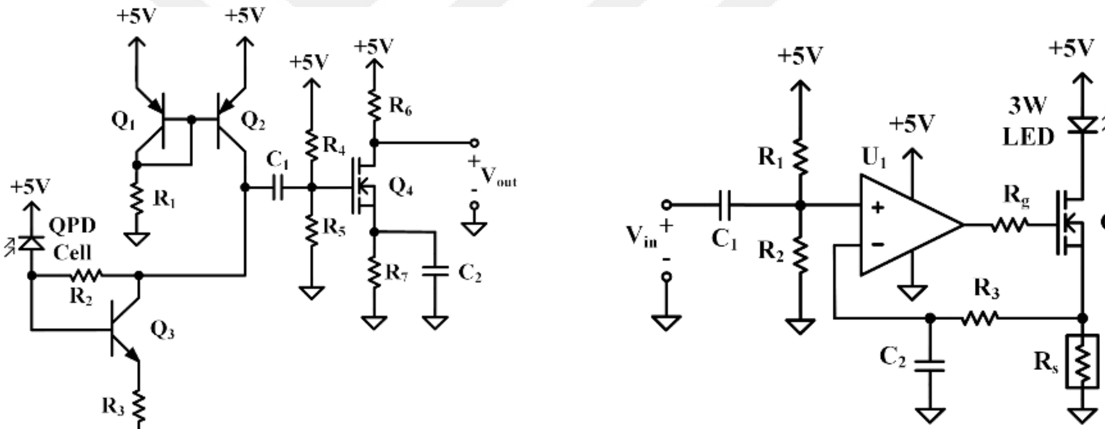

Components for transmitter electronics

R_1	R_2	R_3	R_g	R_s	C_1	C_2	Q_1	U_1
100 kΩ pot		100 Ω	10 Ω	4.2 Ω*	10 uF	100 pF	IRF530	LMH6643

*R_s is a sandstone resistor

Components for receiver electronics

R_1	$R_{2,6}$	R_3	$R_{4,5}$	R_7	C_1	C_2	$Q_{1,2}$	Q_3	Q_4
560 Ω	1 kΩ	100 Ω	100 kΩ	200 Ω	100 nF	10 uF	2N3906	2N3904	2N7000

Figure 3.11: Proof-of-concept TX and QRX schematics. The TX design is a highly simplified version of the prototype in Section 2.1.1, and the QRX read-out circuit design is not an especially optimized one, just tests the idea.

The Adafruit mini pan-tilt kit with standard "micro-servos" (angular resolution of 0.5°) was chosen for the TP subsystem since the prototype was simply built for testing the principles set forth in the previous sections using the QPD.

An STM32F103C8T6, commonly known as the "blue pill", is used as the MCU. The MCU has a 12-bit ADC which was clocked at 50kSPS. Following the tracking procedures described earlier, the MCU takes a 400-sample buffer from each QPD (corresponding to 8 ms), subtracts the mean, takes the square, finds the average of the buffer for each QPD for that 8 ms duration, which is then used for finding x_{spot} and y_{spot}. A simple proportional controller then tries to keep the spot on the QPD center. While <8 ms buffers gave faster TP response, values that approached the full wave periods of BFSK carriers created oscillating average values, hence oscillating x spot /y spot . Larger buffer sizes gave better stability and noise resilience but the MCU memory limited the size to 15 ms. Screenshots from a two-axis demo video are shown in Fig. 3.12.

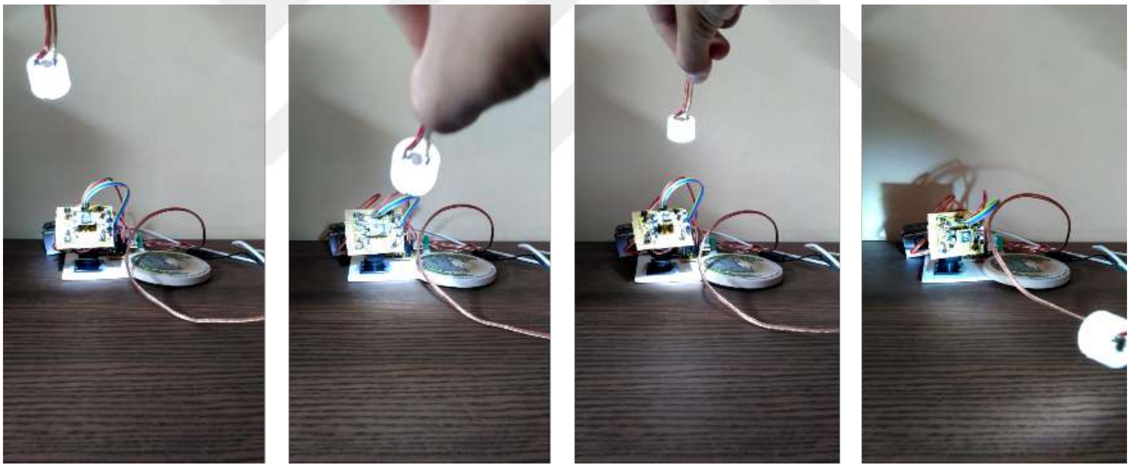

Figure 3.12: Screenshots from the two-axis demo video.

Chapter 4

VEHICULAR VLP FOR COLLISION AVOIDANCE AND PLATOONING

In this chapter, we first review parameter measurement techniques and existing algorithms that use those techniques for position estimation in vehicular VLP. Then, we propose four new positioning algorithms that utilize bearing or range measurements from either single-RX and dual-RX setups; bearing-based methods are exclusively enabled by the QRX presented in the previous chapter. Next, we derive the Cramer-Rao lower bound (CRLB) on positioning accuracy for all existing algorithms to assess the theoretical robustness of the estimations produced by each positioning algorithm against VLC channel noise.

4.1 *Parameter Measurement from Received VLC Signals*

Vehicular VLP methods utilize parameter measurement techniques that use received VLC signal samples to produce bearing/range measurements. Specifically, these techniques make observations on H_{ij} or τ_{ij}, which are then translated to direct relative TX bearing (θ_{ij}) or range (d_{ij}) measurements to one RX, or their differential versions between two RXs when direct measurements are not available. Differential range and bearing are respectively defined as

$$\Delta d_{il/j} = d_{ij} - d_{lj} \quad \text{and} \quad \Delta\theta_{il/j} = \theta_{ij} - \theta_{lj} \ , \tag{4.1}$$

where $l \in \{1, 2, 3, 4\}$, $l \neq i$, denotes the index for the second RX unit on the same face as RX i. This type of signal-based physical parameter measurement has long been an active area of research due to its useful applications in communication (channel estimation [Jiang et al., 2019, Coleri et al., 2002, Chen and Jiang, 2016]) as well as radio-navigation (i.e., RADAR). While the main challenges in the area arising from fading and other multi-path effects are highly pronounced when RF signals are used, vehicular VLC signals are practically devoid of these effects since intensity modulation and direct detection (IM/DD [Pathak et al., 2015]) is used and the channel is LoS-dominant for the distances relevant in collision avoidance and platooning [Turan et al., 2018], enabling high-accuracy measurement [Keskin and Gezici, 2016, Keskin et al., 2018, Wang et al., 2013b, Steendam et al., 2017]. Techniques used for bearing and range measurement in vehicular VLP, categorized by their use of H_{ij} or τ_{ij}, are reviewed in the following.

4.1.1 Techniques Using Propagation Delay Observations (τ_{ij})

Observations on propagation delay are a perfect fit for range measurements since TX-RX distance is directly proportional to τ_{ij} as per Eqn. (2.4). In VLC systems employing multi-carrier modulation strategies like orthogonal frequency division multiplexing (OFDM), observations on τ_{ij} can be made via measuring phase difference over individual carriers or pilot symbols [Şayli et al., 2016, Sandell and Edfors, 1996, Van Welden et al., 2009]. Without loss of generality, we assume a constantly available simple sinusoidal symbol or pilot (i.e., pure tone) for simplifying the analyses in this thesis, boiling the τ_{ij} computation problem down to estimation of the phase shift between that sinusoid and its propagation-delayed version. There are numerous techniques available for this computation [Sedlacek and Krumpholc, 2005], and some of them have been utilized in vehicular VLP literature for range measurements [Liu et al., 2007b, Béchadergue et al., 2016, Roberts et al., 2010]. Note that the typical matched-filter approach for digital phase measurement is not feasible for vehicular VLP since cm-level accuracy would require >10 GHz sampling rates, increasing system cost beyond practical levels.

For direct range measurements, [Béchadergue et al., 2016] presents an auto-digital based technique [Liu et al., 2007b]: VLC units on the ego and target vehicles exchange a high frequency square wave back and forth, and the ego vehicle measures the phase shift between the initial TX signal and the round-trip-propagated RX signal. The channel-corrupted RX signal on the ego vehicle first gets converted to a logic signal by a high-speed comparator [Béchadergue et al., 2019] (i.e., zero-crossing detection) and then gets heterodyned to a lower frequency along with the original TX signal. Since heterodyning increases phase resolution considerably, the shift can be measured in high precision by sampling the logical XOR of the two signals with a high-frequency clock and counting the number of high pulses. While this means the quantized measurement resolution is fundamentally limited by the clock frequency and the heterodyning factor, the quantization intervals can be made small with high-frequency hardware components, e.g., <1 cm for a 100 MHz clock. Although this technique requires high-frequency digital circuits, it has very low complexity and can be completely integrated into a CMOS pipeline since logic (i.e., virtually 1-bit) signals are used. Moreover, sine waves of the same frequency can be transmitted over the channel instead of square waves when narrow band-pass filters are utilized since comparators already convert them to logic signals on the RX end; this makes the technique realizable with current low-bandwidth high-power automotive LEDs and multi-carrier wide-band VLC modulation strategies.

For differential range measurements to two RXs (RX i and RX l) from one TX, [Roberts et al., 2010] presents a DFT-based technique: The upper DFT sideband of one RX signal (RX i) is multiplied with the complex conjugate of its counterpart for the other RX signal (RX l), and the mean of the phase for the result is an estimate of the phase shift between the two RX signals, for the same TX. Although previously unexplored in vehicular VLP, this technique can also be used for direct range measurement when the scenario presented in [Béchadergue et al., 2016] is used (i.e., RX i and RX l are replaced by an known TX signal and its round-trip-propagated RX version). To emphasize this, these two measurement techniques are depicted on the same block diagram in Fig. 4.1. While the complexity of the DFT-based technique [Roberts et al., 2010] is much higher than the auto-digital technique [Béchadergue et al., 2016] due to DFT use and the analog-to-digital conversion requirement (ADC, much higher than 1-bit precision), it typically provides higher accuracy against noise due to averaging as will be shown via simulations. Similarly, the auto-digital measurement principle [Béchadergue et al., 2016] can be applied for differential range measurement, but since differential values are very small, using this technique would be impractical due to the extremely high clock speed required for that level of precision.

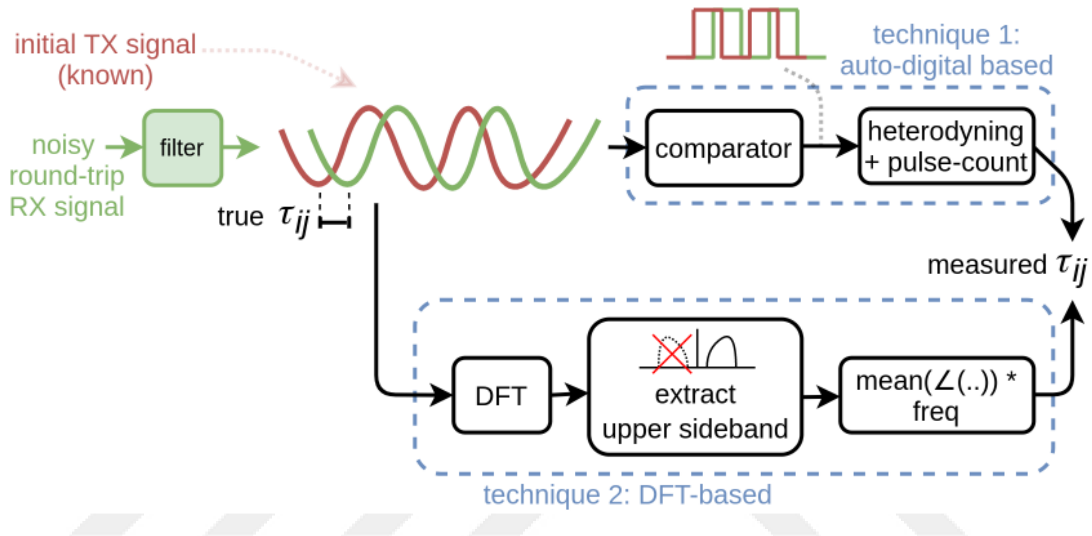

Figure 4.1: Direct range measurement techniques using observations on τ_{ij} and Eqn. (2.4). These techniques can also be used for measuring differential range between filtered RX signals, but the auto-digital method becomes impractical in that case due to extremely high clock speed requirements.

Lastly, τ_{ij} observations do not provide means for bearing measurement as evident from Eqn. (2.3). While derivative measurements are possible, e.g., differential bearing measurement using direct range to two RXs, L and the law of cosines, this simply transfers the uncertainty from one measurement type to the other, thus, is not a dedicated technique.

4.1.2 Techniques Using Channel Gain Observations (H_{ij})

The relationship between H_{ij} and the relative TX-RX distance is straightforward for the LoS vehicular VLC channel: H_{ij} is inversely proportional to the square of the propagation distance [Turan et al., 2018]. Accordingly, for sinusoidal signals, an accurate observation on H_{ij} can be made via computing received signal strength (RSS) by integrating the square of $r_{ij}(t)$ over an interval that captures many $s_j(t)$ cycles [Steendam et al., 2017]. However, extracting range information from that RSS info requires exact knowledge of instantaneous TX power (cf. Eqn. (2.3) and [Keskin and Gezici, 2016, Eqn. (4)]). This is highly unlikely even after a potential future standardization of vehicular VLC TX power since the reference battery voltage on a vehicle is subject to broadband random fluctuations (both in combustion [Yamamoto and Ozeki, 1983] and electrical vehicles [Antoniali et al., 2013]), making exact instantaneous knowledge of TX power infeasible. Therefore, RSS-based direct ranging is not feasible for use in vehicular VLP.

RSS-based differential range measurement is also not feasible in vehicular VLP for a similar reason: In order to extract $\Delta d_{il/j}$ from RSS values, the technique would require exact knowledge of the TX radiation pattern (ρ_j) and of the instantaneous solid angles subtended by each RX (i and l) to the TX. Since this is not realistic, RSS-based differential range measurement is also not feasible for use in vehicular VLP.

RSS can still be used for bearing measurements via angular diversity receivers: An RX that employs closely-packed detectors with different angular “reception” patterns (i.e., ρ_i) will have the same AoA values and different RSS values at all detectors, enabling precise AoA measurement. Accuracy of these measurements fundamentally depend on how close the detectors are[1] and how different their ρ_i patterns are[2]. While there have been many such RX designs in indoor multiple-input-multiple-output (MIMO) VLC [He et al., 2019, Wang et al., 2013a, Wang et al., 2014, Lee and Jung, 2012a] and associated AoA measurement techniques for indoor VLP [Aparicio-Esteve et al., 2019, Cincotta et al., 2019, Arafa et al., 2012, Steendam et al., 2016b, Cincotta et al., 2017, Aparicio-Esteve et al., 2021], only a few of these

[1]Distance between the detectors should be much smaller than their distances to the TX to keep both the bearing and the S_{ij} the same for all detectors.

[2]RSS differences only depend on ρ_i patterns because small-scale fading is insignificant due to detector sizes being millions of wavelengths [Kahn and Barry, 1997, Fig. 2a]

design ideas are feasible in the vehicular domain due to high mobility and harsh road conditions. Specifically, early works have considered pyramidal detectors [Lu and Chen, 2013], but such tilted-detector based techniques, which have also been studied in indoor cases [Zhu et al., 2019b, Lee and Jung, 2012b, Shen et al., 2020, Yang et al., 2014b], suffer in precision and field-of-view (FoV). On the other hand, the QRX design presented in Chapter 3 is a suitable one. It utilizes a planar quadrant-photodiode with front-end optics, and can be used for high-precision and high-FoV direct bearing measurement in vehicular localization.

RSS-based differential bearing measurement techniques are still unexplored in vehicular VLP. Therefore, to enable performance evaluations for the differential bearing based VLP methods later in the thesis, subtraction of two direct bearing measurements will be considered as a differential bearing measurement even though it is a derivative measurement.

4.2 Existing Positioning Algorithms in Vehicular VLP

Positioning algorithms in vehicular VLP use the available parameter measurements described in the previous section and combine them to estimate position. Based on system model assumption (*A2*), only two RXs are considered in this thesis for positioning. The measurements from the two RXs, together with the known baseline L in between, form a determined set of equations, thus, allow for finding a position "fix" in the classical sense, i.e., triangulation or trilateration with a fixed baseline. A different position fixing method, heavily used in other navigation disciplines (e.g., marine and aviation), is the so-called "running" fix, which uses two consecutive measurements from only one RX to a moving TX for position fixing, assuming that the TX relative heading (α_v) and distance traveled (d_v) within that time can be determined. Classical position fixing for direct and differential bearing/range measurements, and running position fixing with direct range measurements, are pictured in Fig. 4.2a, Fig. 4.2b and Fig. 4.2c, respectively. While using measurements from more than two RXs and/or more than two consecutive measurements from the same RXs for a single estimation, thus, forming over-determined systems of equations, could potentially improve performance (e.g., via least squares), the analyses in this thesis only consider the minimal configuration as discussed in the system model description. We discuss other such complex algorithms and the benefits they can bring for the widespread deployment of vehicular VLP later in the thesis, as part of the open questions and future challenges in this field.

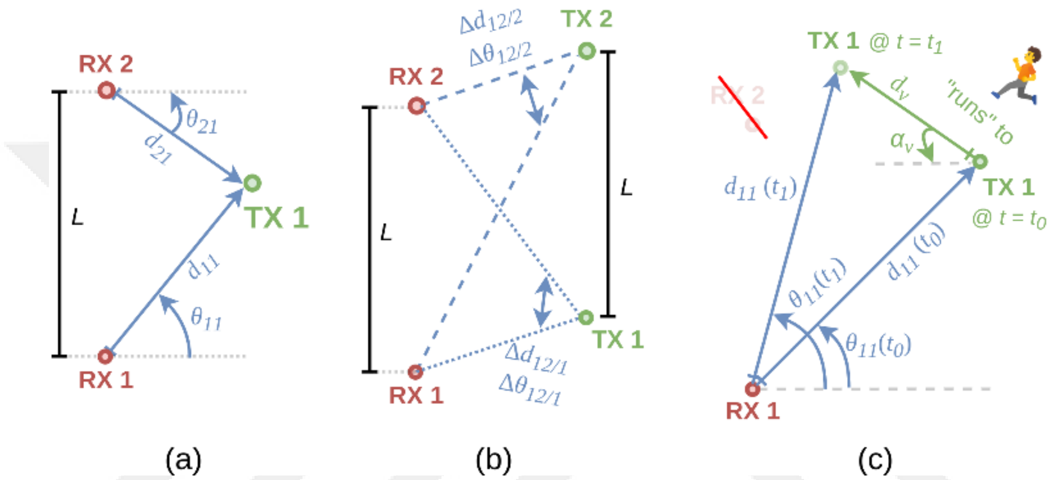

Figure 4.2: (a) classical fix with direct measurements from 2 RXs to 1 TX. (b) classical fix with differential measurements from 2 RXs to 2 TXs that are longitudinally parallel. (c) A running fix with direct measurements only needs 1 RX and 1 TX, but it also needs extra information (i.e., relative target heading, α_v, and travel distance, d_v) to estimate position for two time instants (i.e., $t = t_0$ and $t = t_1$).

Therefore, considering the individual parameter measurement techniques presented in the previous discussions, positioning algorithms that use a minimal configuration in the currently considered system model can be categorized with respect to their use of the following:

- differential (as in Eqn.(4.1)) vs. direct measurements,
- for bearing vs. range parameters, and
- classical vs. running position fixing.

Accordingly, we describe existing positioning algorithms in the following: Since the system model considers 2 RX units on a given face and a known baseline in between, the most straightforward strategy is classical position fixing with direct measurements. This has only been explored for the range parameter in the literature, i.e., trilateration as in [Béchadergue et al., 2017]; a bearing-based version of this algorithm is proposed later in this chapter. Classical position fixing with differential measurements for the 2 RX case requires 2 TXs on the target vehicle that are longitudinally parallel to the 2 RXs for a determined solution. This has only been explored for the range parameter so far in the literature by [Roberts et al., 2010]; a positioning algorithm for differential bearing measurements will be proposed later in this chapter. When the target TX is not in sight of one of the RXs, a running position fix can be made with a single RX and a single TX via direct measurements. This was not explored in the literature before this thesis; both bearing and range based versions of the running position fixing algorithm will be proposed later in this chapter. Note that a running position fix with differential measurements is not feasible because it would require the target vehicle to move sideways a significant distance, conflicting with the Ackermann steering rules on which modern 4-wheel road vehicles are pre-dominantly based (i.e., no side-slip [Ackermann, 1994]).

4.3 Novel Positioning Algorithms

We now formulate four new positioning algorithms that were previously unexplored in the vehicular VLP literature:

1. classical position fixing using direct bearing measurements,

2. running position fixing using direct bearing measurements,

3. running position fixing using direct range measurements, and

4. classical position fixing using differential bearing measurements,

4.3.1 Classical Fix, Direct Bearing Measurements

The classical position fixing algorithm using direct bearing measurements computes the relative position of two target TX units which define the vehicle location, via triangulation: TXs are located at the apexes of the triangles defined by two AoA measurements from two QRXs and the distance L between them. Specifically, the position estimation for TX j, (x_j, y_j), where $j \in \{1, 2\}$, is computed by using $\widehat{\theta_{1j}}$, $\widehat{\theta_{2j}}$ and L, and the law of sines, as follows:

$$\begin{bmatrix} \widehat{x_j} \\ \widehat{y_j} \end{bmatrix} = \begin{bmatrix} L\left(1 + \dfrac{\sin(\widehat{\theta_{2j}}) \times \cos(\widehat{\theta_{1j}})}{\sin(\widehat{\theta_{1j}} - \widehat{\theta_{2j}})}\right) \\ L\left(\dfrac{\cos(\widehat{\theta_{2j}}) \times \cos(\widehat{\theta_{1j}})}{\sin(\widehat{\theta_{1j}} - \widehat{\theta_{2j}})}\right) \end{bmatrix}, \tag{4.2}$$

and the localization rate is equal to the AoA measurement rate. The geometry for Eqn. (4.2) is depicted in Fig. 4.3.

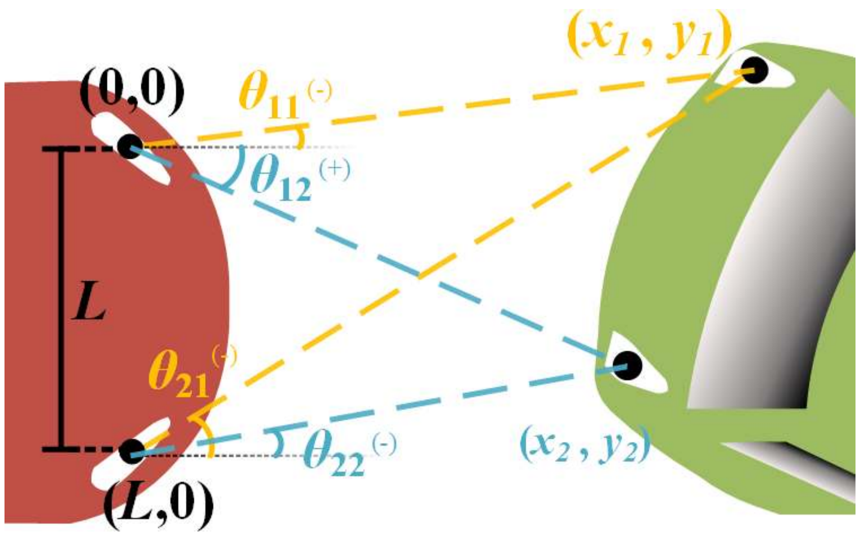

Figure 4.3: The triangulation geometry used for dual-AoA-based VLP.

4.3.2 Running Fix, Direct Bearing Measurements

Running position fixing methods utilize measurements from 1 RX to 1 TX only. A single AoA measurement does not define a TX position, but it constrains the solution set to positions on a line, as shown in Fig. 4.4a. Rather than using two distinct spatially separated AoA measurements from different nodes, it's also possible to use two distinct temporally separated AoA measurements ($\theta_{ij}(t)$) from the same node. This transforms the solution set from single positions to tuples of positions for two time instants, still unbounded, as shown in Fig. 4.4b.

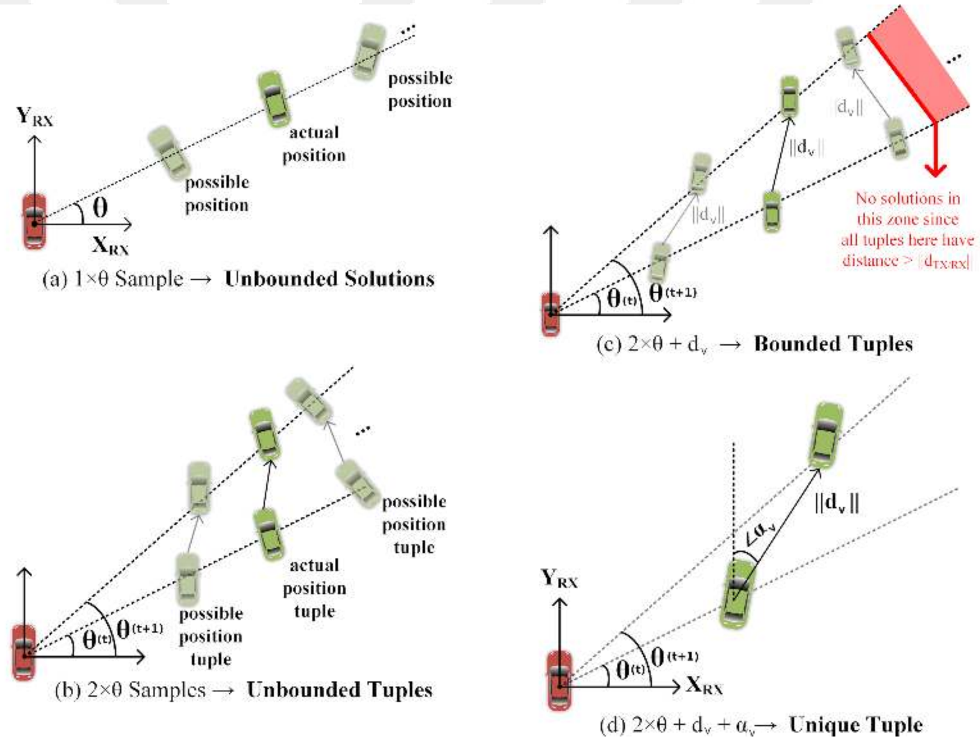

Figure 4.4: Single-RX running position fixing using bearing measurements.

Adding the information of relative distance travelled by the target vehicle (d_v) puts a bound on the solution set of tuples. The tuples which contain positions further apart than the shortest distance between the two lines defined by the two AoA measurements are eliminated (Fig. 4.4c). For a given target vehicle relative heading angle (α_v), there exists a unique tuple within this bounded set in Fig. 4.4c, which gives the position of TX relative to the RX during the two time instants at which the AoA measurements were taken (Fig. 4.4d). Hence, with a single AoA-measurement-capable VLC receiver on the ego vehicle, finding the relative position of the TX is possible if the relative heading angle of and distance traveled by target vehicle, both with respect to the ego frame of reference, can be inferred from the VLC signal. Specifically, the VLP method first uses:

- ego and target vehicle global heading (ψ), measured by on-board sensors, target ψ transmitted to ego vehicle via VLC, and
- ego and target vehicle speeds (v), measured by on-board sensors, target v transmitted to ego vehicle via VLC,

to find:

- target relative heading in ego frame of reference (a_v), and
- target relative distance traveled in ego frame of reference (d_v).

Next, using two consecutive AoA measurements (θ for time instants $t = t_0$ and $t = t_1$), d_v and α_v, the method computes the position of the TX unit at the two consecutive time instants.

Find Relative Target Vehicle Heading

The relative heading of target vehicle in the ego vehicle frame (α_v) can be deduced from the global headings (ψ) of and the distance traveled by ego and target ($d_{RX/RX}$ and $d_{TX/TX}$) within the time interval between two consecutive AoA measurements ($\Delta t = t_1 - t_0$). Ego speed, measured by the ego vehicle sensor, and target speed, measured by the target vehicle sensor and sent over the VLC channel to the ego vehicle, are multiplied by Δt to get the respective ego and target distances. The target global heading, measured by the target vehicle sensor, is also included in the same VLC message. Defining $\zeta = \psi_{TX} - \psi_{RX}$, the right triangles shown in Fig. 4.5 are used to find a_v, resulting in the following relationship:

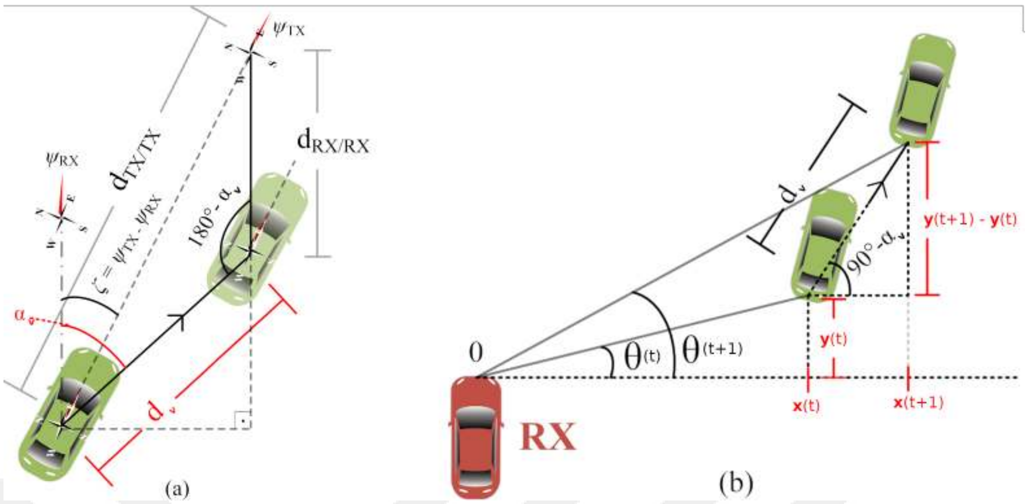

Figure 4.5: Running position fixing algorithm using direct bearing measurements. Geometry (a) used for finding α_v and d_v. Geometry (b) used for finding the relative target TX position.

$$\alpha_v = 90^\circ - \arctan\left(\frac{d_{TX/TX}\left(\sin(\vartheta)\right) - d_{RX/RX}}{d_{TX/TX}\left(\cos(\vartheta)\right)}\right), \tag{4.3}$$

where $\vartheta = 90^\circ - \zeta$.

Find Target Vehicle Relative Distance Traveled

After finding α_v, the distance traveled by target in ego frame (d_v) is needed. Solving the smaller right triangle in Fig. 4.5a gives d_v:

$$d_v = \sqrt{\left(d_{TX/TX}\left(\cos(\vartheta)\right)\right)^2 + \left(d_{TX/TX}\left(\sin(\vartheta)\right) - d_{RX/RX}\right)^2}. \tag{4.4}$$

Find Target TX Relative Position

Finally, with d_v and α_v known, right triangles shown in Fig. 4.5b are used for deducing relative target TX position. Solving the following system of equations:

$$C1 = \frac{y(t)}{x(t)} \quad , \quad C2 = \frac{y(t+1)}{x(t+1)} \quad , \quad x(t+1) - x(t) = \sin(d_v) \quad , \quad y(t+1) - y(t) = \cos(d_v)$$

(4.5)

results in the following solutions for the position coordinates:

$$x(t) = d_v \left(\frac{\cos(\alpha_v) - C2 \cdot \sin(\alpha_v)}{C2 - C1} \right) \quad , \quad y(t) = C1\,(x(t)) \tag{4.6}$$

$$x(t+1) = d_v \cdot \sin(\alpha_v) + x(t) \quad , \quad y(t+1) = C2\,(x(t+1)) \tag{4.7}$$

Note that "t" refers to time instant t_0 and "$t+1$" refers to time instant t_1 in the preceding equations.

4.3.3 Running Fix, Direct Range Measurements

The previous section solved a triangular geometry for running position fixing using direct bearing measurements using also relative distance traveled by the target vehicle and its relative heading information, $\widehat{d_v}$ and $\widehat{\alpha_v}$ respectively. Since it does running position fixing, the algorithm in the previous section uses measurements for a single TX-RX link at two consecutive time instants (i.e., $\widehat{\theta_{11}}(t_0)$ and $\widehat{\theta_{11}}(t_1)$ for time instants $t = t_0$ and $t = t_1$ respectively) and produces estimates for TX position at those two time instants (i.e., $(\widehat{x_1}(t_0), \widehat{y_1}(t_0))$ and $(\widehat{x_1}(t_1), \widehat{y_1}(t_1))$). In similar fashion, we provide the following positioning algorithm for running position fixing using direct range measurements:

$$\varphi = \alpha_v + \cos^{-1} \left(\frac{\widehat{d_v}^{\,2} + \left(\widehat{d_{11}}(t_0)\right)^2 - \left(\widehat{d_{11}}(t_1)\right)^2}{2 \cdot \widehat{d_v} \cdot \left(\widehat{d_{11}}(t_1)\right)} \right) \quad , \tag{4.8a}$$

$$\begin{bmatrix} \widehat{x_1}(t_1) \\ \widehat{y_1}(t_1) \end{bmatrix} = \begin{bmatrix} \widehat{d_{11}}(t_1) \cdot \cos(\varphi) \\ \widehat{d_{11}}(t_1) \cdot \sin(\varphi) \end{bmatrix} \quad , \quad \begin{bmatrix} \widehat{x_1}(t_0) \\ \widehat{y_1}(t_0) \end{bmatrix} = \begin{bmatrix} \widehat{x_1}(t_1) - \widehat{d_v} \cdot \cos(\alpha_v) \\ \widehat{y_1}(t_1) - \widehat{d_v} \cdot \sin(\alpha_v) \end{bmatrix} \tag{4.8b}$$

where $\widehat{d_{11}}(t_0)$ and $\widehat{d_{11}}(t_1)$ are the direct range measurements.

4.3.4 Classical Fix, Differential Bearing Measurements

The vehicular VLP method in [Roberts et al., 2010] solves the quadrilateral geometry formed by two RXs and two TXs that are parallel to each other and provides the highly complex position coordinate estimation expressions based on "delta lengths", i.e., the differential range measurements, for classical position fixing using those measurements. In similar fashion, we solve the same quadrilateral geometry for angle-difference-of-arrival (ADoA, as in [Zhu et al., 2017, Fig. 1]), i.e., differential bearing measurements, and provide the following related positioning algorithm:

$$K = \frac{1}{2}\left(\frac{1}{\tan\left(\Delta\theta_{12/2}\right)} - \frac{1}{\tan\left(\Delta\theta_{12/1}\right)}\right) \tag{4.9a}$$

$$\begin{bmatrix} \widehat{x_1} \\ \widehat{y_1} \end{bmatrix} = \begin{bmatrix} K \cdot y_1 \\ \left(\frac{L}{1+K^2}\right)\left(\frac{1}{\tan\left(\Delta\theta_{12/2}\right)} - K\right) \end{bmatrix} \tag{4.9b}$$

Considering this last formulation, it is important to emphasize that algorithms using differential measurements ([Roberts et al., 2010] for range, and Eqn. (4.9) for bearing measurements) produce position estimates based on the assumption that the target and ego vehicles are parallel to each other. Therefore, even when this condition is not met, the methods interpret the input measurements as though they came from a target vehicle that is longitudinally parallel to the ego vehicle, and produce estimations accordingly. Although such an estimation obviously has systematic error when the vehicles are not parallel to each other, thus, results in biased estimates, this error can be acceptably small in practice for certain scenarios where heading difference between the two vehicles is small (e.g., during high speed cruise on a highway). For this reason, we do not discard the estimations from these methods even when the two vehicles are not longitudinally parallel, which happens very frequently in real driving scenarios due to high mobility.

The existing state-of-the-art vehicular VLP positioning algorithms and the algorithms that were just described, are summarized in Table 4.1.

Table 4.1: State-of-the-Art Positioning Algorithms in Vehicular VLP

	direct meas.		differential meas.	
	classical fix	running fix	classical fix	running fix
range	✓, [Béchadergue et al., 2017]	✓[b], Section 4.3.3	✓, [Roberts et al., 2010]	× [a]
bearing	✓[b], Section 4.3.1	✓[b], Section 4.3.2	✓[b], Section 4.3.4	× [a]

[a] not feasible since it strictly requires the vehicle to move only sideways.

[b] feasible, but was previously unexplored, proposed in this thesis.

4.4 Statistical Analysis of Positioning Algorithms

We now provide statistical analysis for the positioning algorithms that were discussed so far by deriving their respective CRLBs on positioning accuracy. However, before deriving the CRLBs, we first briefly show that all of the vehicular VLP positioning algorithms discussed so far, and also the existing state-of-the-art algorithms ([Roberts et al., 2010, Béchadergue et al., 2017]), provide maximum likelihood estimates for the respective sets of measurements they utilize.

4.4.1 Maximum Likelihood Position Estimation

Let $\mathbf{P}$ be a vector containing the true values of the quantities that are to be estimated (i.e., true position coordinates), let $\mathbf{G}$ be a vector containing the deterministic system model equations that relate the true values of quantities that are to be estimated to a set of measurements, let $\mathbf{M}$ be a vector containing that set of N_H measurements, let N_H be the number of measurements in that set, let $\mathbf{W}$ be zero-mean AWGN terms with variance $\sigma^2_{\mathbf{W}}$ that contaminate the true values of those measurements, and let M_h, G_h and W_h be the element number h for vectors $\mathbf{M}$, $\mathbf{G}$ and $\mathbf{W}$, respectively, where $h \in \{1, 2, ..., N_H\}$. This measurement set (i.e., set of M_h values) can be expressed as:

$$M_h = G_h(\mathbf{P}) + W_h \quad , \quad h \in \{1, 2, ..., N_H\} \quad . \tag{4.10}$$

Since W_h are AWGN, M_h are independent Gaussian random variables (r.v.) with mean $G_h(\mathbf{P})$ and variance $\sigma^2_{W_h}$. Thus, the log-likelihood function ($\ln p(\mathbf{M};\mathbf{P})$), which is the logarithm of the joint probability density function (PDF) for the r.v.s, is:

$$\ln p(\mathbf{M};\mathbf{P}) = -\frac{\sum_{h=1}^{N_H} \ln 2\pi\sigma^2_{W_h}}{2} - \sum_{h=1}^{N_H} \frac{(M_h - G_h(\mathbf{P}))^2}{2\sigma^2_{W_h}} \quad . \tag{4.11}$$

MLE occurs at the global maximum of this unimodal distribution, which is at the position that makes the first partial derivatives of the log-likelihood function with respect to each quantity equal to 0. Thus, the MLE positioning algorithm for a given measurement set can be formulated by solving the following for each element in vector $\mathbf{P}$:

$$\frac{\delta \ln p(\mathbf{M};\mathbf{P})}{\delta P_m} = \sum_{h=1}^{N_H} \frac{M_h - G_h(\mathbf{P})}{\sigma^2_{W_h}} \cdot \frac{\delta G_h(\mathbf{P})}{\delta P_m} = 0 \ , \tag{4.12}$$

where $P_m, \ m \in \{1, 2, ..., N_M\}$ is m^{th} element in vector $\mathbf{P}$, i.e., the true value for the m^{th} quantity that is to be estimated, and N_M is the number of quantities to be estimated. Conversely, an algorithm can be shown to provide MLE by simply replacing P_m with $\widehat{P_m}$, the estimation for the m^{th} quantity, and showing that Eqn. (4.12) holds. We next demonstrate this for a chosen algorithm as an example. The positioning algorithm in Section 4.3.1 is based on triangulation with bearing measurements from two fixed anchors [Nguyen and Shin, 2013], i.e., it is the exact functional inverse of the system model equations that constitute its measurement set. Note that this is possible due to $N_H = N_M$, i.e., due to the set of equations being determined. The coordinate estimates, which are derived using the law of sines, are expressed as in Eqn. (4.2).

Using Eqn. (2.4) to form the $G_h(\mathbf{P})$ terms, replacing the (x_1, y_1) terms in those equations with $(\widehat{x_1}, \widehat{y_1})$ from Eqn. (4.2), and noting that M_h terms correspond to $\widehat{\theta_{11}}$ and $\widehat{\theta_{21}}$, the first term of the multiplication inside the sum in Eqn. (4.12) becomes 0 for all $h \in \{1, 2\}$ after simplifications, thus, proves that the algorithm in Eqn. (4.2) provides MLE for its measurement set since Eqn. (4.12) holds. Following from this demonstration, we make the following generalization here, which holds for all other existing state-of-the-art vehicular VLP positioning algorithms: For a set of measurements that provides a determined set of equations (i.e., $N_H = N_M$), if the position estimation algorithm for that model is formulated using the functional inverse of the related system model equations, that algorithm provides maximum likelihood position estimations as long as the measurement set can be expressed with Eqn. (4.10), i.e., when parameter measurements are contaminated with AWGN.

4.4.2 Cramer-Rao Lower Bound on Positioning Accuracy

The CRLB lower bounds the mean-squared-error (MSE) for an unbiased estimate of a quantity considering related noisy measurements. It is a suitable tool for analytically evaluating the performance of a vehicular VLP positioning algorithm under noise since individual parameter measurements in vehicular VLP are contaminated by AWGN due to channel noise of the same statistical nature [Kay, 1993, Yu et al., 2013, Béchadergue et al., 2018]. For this reason, we derive the bound for each algorithm here with respect to their bearing/range measurements. The resulting CRLB thus expresses the robustness of unbiased estimates against errors in parameter measurement, and is applicable to all individual parameter measurement techniques, including those proposed for different RX designs.

The derivation procedure first computes the Fisher information matrix (FIM), $\mathbf{F}$, for the considered measurement set (a.k.a. the "dataset" [Kay, 1993]). The diagonal elements of the inverse of the FIM correspond to the lower bound of MSE (i.e., minimum variance around the true value) for each estimation:

$$var(\widehat{P_m}) \geq \left(\mathbf{F}^{-1}\right)_{m,m'} , \tag{4.13}$$

where $var()$ denotes variance, $m, m' \in \{1, 2, ..., N_M\}$ denote row and column indices for the FIM respectively and $m = m'$ in Eqn. (4.13) (recall that N_M is the number of quantities that are to be estimated and that $\widehat{P_m}$ is the estimation for the m^{th} quantity). The elements of the FIM are computed by:

$$\mathbf{F}_{m,m'} = -\sum_{h=1}^{N_H} \frac{1}{\sigma^2_{W_h}} \left(\frac{\delta G_h(\mathbf{P})}{\delta P_m} \cdot \frac{\delta G_h(\mathbf{P})}{\delta P_{m'}} \right) , \tag{4.14}$$

Since the final symbolic CRLB expressions (i.e., after inverting the FIM in Eqn. 4.13) are unnecessarily complex, we present only the computation of the FIM elements during the derivations based on Eqn. 4.14, and the final CRLBs are numerically computed during simulations using the terms provided here. For each algorithm, we first point to the relevant system model equations that constitute the $G_h()$, $h \in \{1, 2, ..., N_H\}$ functions, and then provide the $\delta G_h()/\delta x_1$ and $\delta G_h()/\delta y_1$ terms for each of the N_H measurements, which are used for building the FIM via Eqn. (4.14) since $\mathbf{P} = [x_1 \;\; y_1]$.

CRLB, Classical Fix, Direct Measurements

These algorithms use measurements $(\widehat{d_{11}}, \widehat{d_{21}})$ for range and $(\widehat{\theta_{11}}, \widehat{\theta_{21}})$ for bearing. These are measurements for the actual direct range and bearing values from TX 1 to RX 1 and to RX 2 respectively (cf., Eqn. (2.4)), contaminated by AWGN of variance $(\sigma^2_{d_{11}}, \sigma^2_{d_{21}})$ for range and $(\sigma^2_{\theta_{11}}, \sigma^2_{\theta_{21}})$ for bearing, respectively. Noting that $N_H = N_M = 2$, i.e., that a minimal configuration is present (cf., (*A2*)), the derivative terms necessary for constructing the associated FIM using Eqn. (4.14) for range measurements are:

$$\frac{\delta d_{11}}{\delta x_1} = \frac{x_1}{\sqrt{x_1^2 + y_1^2}} \;, \;\; \frac{\delta d_{21}}{\delta x_1} = \frac{(x_1 - L)}{\sqrt{(x_1 - L)^2 + y_1^2}} \tag{4.15a}$$

$$\frac{\delta d_{11}}{\delta y_1} = \frac{y_1}{\sqrt{x_1^2 + y_1^2}} \;, \;\; \frac{\delta d_{21}}{\delta y_1} = \frac{y_1}{\sqrt{(x_1 - L)^2 + y_1^2}}. \tag{4.15b}$$

Repeating this for the bearing measurements yields:

$$\frac{\delta\theta_{11}}{\delta x_1} = \frac{y_1}{x_1^2 + y_1^2} \,, \; \frac{\delta\theta_{21}}{\delta x_1} = \frac{y_1}{(x_1 - L)^2 + y_1^2} \tag{4.16a}$$

$$\frac{\delta\theta_{11}}{\delta y_1} = -\frac{x_1}{x_1^2 + y_1^2} \,, \; \frac{\delta\theta_{21}}{\delta y_1} = -\frac{(x_1 - L)}{(x_1 - L)^2 + y_1^2}. \tag{4.16b}$$

CRLB, Classical Fix, Differential Measurements

These algorithms use measurements ($\widehat{\Delta d_{12/1}}$, $\widehat{\Delta d_{12/2}}$) for range and ($\widehat{\Delta\theta_{12/1}}$, $\widehat{\Delta\theta_{12/2}}$) for bearing. These are measurements for the differences in actual range/bearing values of TX 1 to RX 1 and RX 2 and the same for TX 2 as governed by Eqn. (4.1). These measurements are contaminated by AWGN of variance ($\sigma^2_{\Delta d_{12/1}}$, $\sigma^2_{\Delta d_{12/2}}$) for range and ($\sigma^2_{\Delta\theta_{12/1}}$, $\sigma^2_{\Delta\theta_{12/1}}$) for bearing, respectively. Note that $N_H = N_M = 2$, and that the model only allows unbiased estimates when $(x_2, y_2) = (x_1 + L,\; y_1)$, i.e., when the target vehicle and ego vehicle are longitudinally parallel to each other.

The derivative terms necessary for constructing the associated FIM using Eqn. (4.14) for range measurements are:

$$\frac{\delta\Delta d_{12/1}}{\delta x_1} = \frac{x_1}{\sqrt{x_1^2 + y_1^2}} - \frac{(x_1 - L)}{\sqrt{(x_1 - L)^2 + y_1^2}}, \tag{4.17a}$$

$$\frac{\delta\Delta d_{12/2}}{\delta x_1} = \frac{x_1 + L}{\sqrt{(x_1 + L)^2 + y_1^2}} - \frac{x_1}{\sqrt{x_1^2 + y_1^2}}, \tag{4.17b}$$

$$\frac{\delta\Delta d_{12/1}}{\delta y_1} = \frac{y_1}{\sqrt{x_1^2 + y_1^2}} - \frac{y_1}{\sqrt{(x_1 - L)^2 + y_1^2}}, \tag{4.17c}$$

$$\frac{\delta\Delta d_{12/2}}{\delta y_1} = \frac{y_1}{\sqrt{(x_1 + L)^2 + y_1^2}} - \frac{y_1}{\sqrt{x_1^2 + y_1^2}}. \tag{4.17d}$$

Repeating this for the bearing measurements yields:

$$\frac{\delta \Delta\theta_{12/1}}{\delta x_1} = \frac{y_1}{x_1^2 + y_1^2} - \frac{y_1}{(x_1 - L)^2 + y_1^2}, \tag{4.18a}$$

$$\frac{\delta \Delta\theta_{12/2}}{\delta x_1} = \frac{y_1}{(x_1 + L)^2 + y_1^2} - \frac{y_1}{x_1^2 + y_1^2}, \tag{4.18b}$$

$$\frac{\delta \Delta\theta_{12/1}}{\delta y_1} = \frac{(x_1 - L)}{(x_1 - L)^2 + y_1^2} - \frac{x_1}{x_1^2 + y_1^2}, \tag{4.18c}$$

$$\frac{\delta \Delta\theta_{12/2}}{\delta y_1} = \frac{x_1}{x_1^2 + y_1^2} - \frac{(x_1 + L)}{(x_1 + L)^2 + y_1^2}. \tag{4.18d}$$

CRLB, Running Fix, Direct Measurements

The running position fix is fundamentally different from the classical fix: It explicitly requires target vehicle relative movement since it estimates position at two consecutive time steps (4 quantities in total), i.e., for $\mathbf{P} = [x_1(t_0) \;\; y_1(t_0) \;\; x_1(t_1) \;\; y_1(t_1)]$, where t_0 and t_1 denote the two consecutive time instants separated by the VLP update period. Thus, it requires two extra measurements for a determined system: The relative target vehicle heading (α_v) and distance traveled (d_v). The relations between α_v and d_v and the position are as follows:

$$\alpha_v = \arctan\left(\frac{x_1(t_1) - x_1(t_0)}{y_1(t_1) - y_1(t_0)}\right) \tag{4.19a}$$

$$d_v = \sqrt{(x_1(t_1) - x_1(t_0))^2 + (y_1(t_1) - y_1(t_0))^2} \tag{4.19b}$$

where, ideally, a_v and d_v should be constant between time instants t_0 and t_1 as discussed in Section 4.3.2. The measurements for α_v and d_v, i.e., $\widehat{\alpha_v}$ and $\widehat{d_v}$ respectively, can be computed from on-board inertial sensor information transmitted over the VLC channel from the target to the ego. The measurements can be assumed to be contaminated by AWGN and standard deviation values can be obtained from sensor datasheet information. These are combined with two consecutive direct measurements of bearing ($\widehat{\theta_{11}}(t_0)$ and $\widehat{\theta_{11}}(t_1)$) or range ($\widehat{d_{11}}(t_0)$ and $\widehat{d_{11}}(t_1)$) for position estimation (i.e., $N_H = N_M = 4$ in both cases). The derivative terms for the direct bearing and range measurements were already derived in Eqns. (4.16a) and (4.16b) and Eqns. (4.15a) and (4.15b) respectively, and the derivation of the terms for α_v and d_v are straightforward using the same primitives.

Before concluding this section, we also discuss two more statistical properties common for all of the MLE positioning algorithms presented above: 1) At extremely low signal-to-noise-ratio (SNR), the symmetrical Gaussian distributions at the algorithm inputs (i.e., parameter measurements) naturally get transformed into asymmetrical ones at the outputs (i.e., position estimations) due to the non-linearity of the algorithms, making the position estimations biased. However, as discussed in detail in [Kay, 1993, Ch. 7.2], estimates are still strongly unbiased at moderate to high SNR, which reinforces the usefulness of the CRLB analyses under most conditions. Moreover, 2) these estimators converge to the minimum variance unbiased estimators (MVUE) for their respective problems in the same moderate to high SNR regime. While showing this via the CRLB theorem, i.e., by showing that the algorithm expressions satisfy [Kay, 1993, Eqn. (3.7)], is not straightforward due to the non-linearity involved, it is straightforward to show this using the Rao-Blackwell-Lehmann-Scheffé (RBLS) theorem [Kay, 1993]. The proof for each algorithm is the same, and follows from [Kay, 1993, Example 5.6] by noting the following:

- the estimator is unbiased for moderate to high SNR levels,
- the input parameter measurement set (i.e., "dataset") itself is a sufficient statistic for the problem, and
- this sufficient statistic is also complete. The set of input parameter measurements for the algorithms is not exactly of the same nature as the "dataset" in [Kay, 1993, Example 5.6]: The algorithms here are all nonlinear and in vector

form. However, Gaussian parameter noise PDFs ensure that those statistics are also complete, like in [Kay, 1993, Example 5.6].

The preceding holds for all algorithms, thereby proving that they converge to MVUE for their respective problems at higher SNR. We next evaluate these deductions about statistical performance and support our analyses with empirical evidence via simulations.

Chapter 5

SIMULATED PERFORMANCE BENCHMARK FOR VEHICULAR VLP

In this chapter, we provide results for three simulation campaigns:

1. Evaluation of the running position fixing algorithm that uses direct bearing measurements from the QRX (Section 4.3.2).

2. Evaluation and statistical analysis of the classical position fixing algorithm that uses direct bearing measurements from the QRX (Section 4.3.1).

3. Evaluation, fair comparison and statistical analysis of all positioning algorithms discussed in this thesis, including both the newly proposed ones (Sections 4.3.1, 4.3.2, 4.3.3 and 4.3.4), and the previous state-of-the-art [Béchadergue et al., 2017, Roberts et al., 2010].

to prove the eligibility of VLP for use as a complementary relative vehicle positioning technology in collision avoidance and platooning applications.

5.1 *Evaluation of the Direct Bearing-based Running Position Fixing Algorithm*

5.1.1 Performance Attributes

The performance of the direct bearing-based running position fixing algorithm described in Section 4.3.2 is dependent on the following attributes (PA#):

- PA1: Accuracy of the positioning algorithm inputs: θ, ψ and υ measurements. While these metrics depend on sensor/hardware specifications for all three,

θ is additionally subject to signal-to-noise ratio (SNR) on the additive white gaussian noise (AWGN) VLC channel since it's inferred from the received waveform.

- PA2: The relative magnitudes of vehicle dynamics ($\frac{\Delta\alpha_v}{\Delta t}$ and $\frac{\Delta v}{\Delta t}$), sensor measurement rates, VLC message rate and VLP positioning rate.

The method finds the exact relative target TX position if it receives exact θ, ψ and v input data (perfect PA1) and the relative vehicle dynamics is constant for the two consecutive time instants t_0 and t_1 (perfect PA2, i.e. $\frac{\Delta\alpha_v}{\Delta t}$ and $\frac{\Delta v}{\Delta t}$ are 0). Non-idealities in realistic road and channel conditions and practical constraints on the system cause deteriorations in PAs, and thus degradation of VLP performance. While the ψ and v sensor inaccuracies and SNR-dependent θ measurement inaccuracy constitutes PA1-related degradations, PA2 deteriorates as the following condition weakens:

$$\min\left(sensing\ rate,\ VLC\ rate\right) \geq\ VLP\ Rate\ \gg\ \left(\frac{\Delta\alpha_v}{\Delta t}, \frac{\Delta v}{\Delta t}\right) \tag{5.1}$$

Since the VLP method running on the ego vehicle requires real-time ψ and v, the limit for maximum VLP rate is the minimum of the ψ and v sensing rate and the VLC link data rate (over which the ego vehicle receives target ψ and v information). On the lower side of Eqn. (5.1), since the VLP method assumes constant relative vehicle dynamics over the two consecutive θ samples on which it operates, VLP performance degrades as the difference between the VLP rate and the vehicle dynamics gets narrower for non-constant vehicle dynamics. For constant vehicle dynamics, there is no hard limit on the minimum VLP rate.

5.1.2 Performance Evaluation

The goal of the simulations in this section is to demonstrate the performance of the proposed VLP method under practical system constraints and realistic road and VLC channel conditions by introducing realistic deteriorations to the PAs. Each deterioration is applied in turn by tuning the others to their realistic minimums to maintain the clarity of presentation.

An end-to-end vehicular VLC system simulator was built in MATLAB©for generating the RX VLC signal, from which the proposed VLP method infers the only input information it needs: θ, ψ and υ. The simulator considers an automotive grade standard 1000 lumen power LED (typical for taillights and low-intensity headlights) as TX. The LED intensity is modulated with binary frequency shift keying (BFSK) for simplicity, and the VLC link rate is chosen as 25 kbps, larger than the requirement for collision avoidance [CAMP Vehicle Safety Communications Consortium, 2005] which is approximately 5 kbps [Căilean and Dimian, 2017]. First order ray-optical simulation of the AoA-sensing QRX receiver are considered, and AC-coupled amplifiers on each QRX cell reject ambient low frequency noise and feed the signal to the ADCs on the ego vehicle microcontroller. The readings from the four cells carry the same TX VLC signal with different power, which is used for deducing AoA. Combination of the four cells is used for VLC.

PA1 - Effect of SNR on θ Measurement Performance and VLP

The target vehicle movement with respect to the ego causes the intensity reaching ego RX to change, resulting in a dynamic SNR. Therefore, while evaluating VLP performance sensitivity to θ by changing SNR, the "worst-case SNR" over a trajectory is considered as the signal integrity metric. Fig. 5.1 demonstrates the effect of VLC SNR on θ and thus on VLP performance (PA1) for a straight and steady target vehicle trajectory relative to the ego vehicle (i.e. $\frac{\Delta\alpha_v}{\Delta t}$, $\frac{\Delta\upsilon}{\Delta t} = 0$, therefore no effect from PA2) and perfect ψ and υ sensor measurements.

Target vehicle is slightly faster than ego vehicle, which is cruising at 36 km/h, moving away from it in an oblique direction ($\alpha_v = 16.7°$) for 2 seconds. Fig. 5.1c is drawn in ego frame, therefore ego movement is not depicted. Performance becomes worse towards the end of the trajectory, where SNR is lower. In order to combat noise in the proposed VLP method, the ADC samples used for θ measurement can be averaged over time. This action decreases θ sample rate and thus VLP rate since

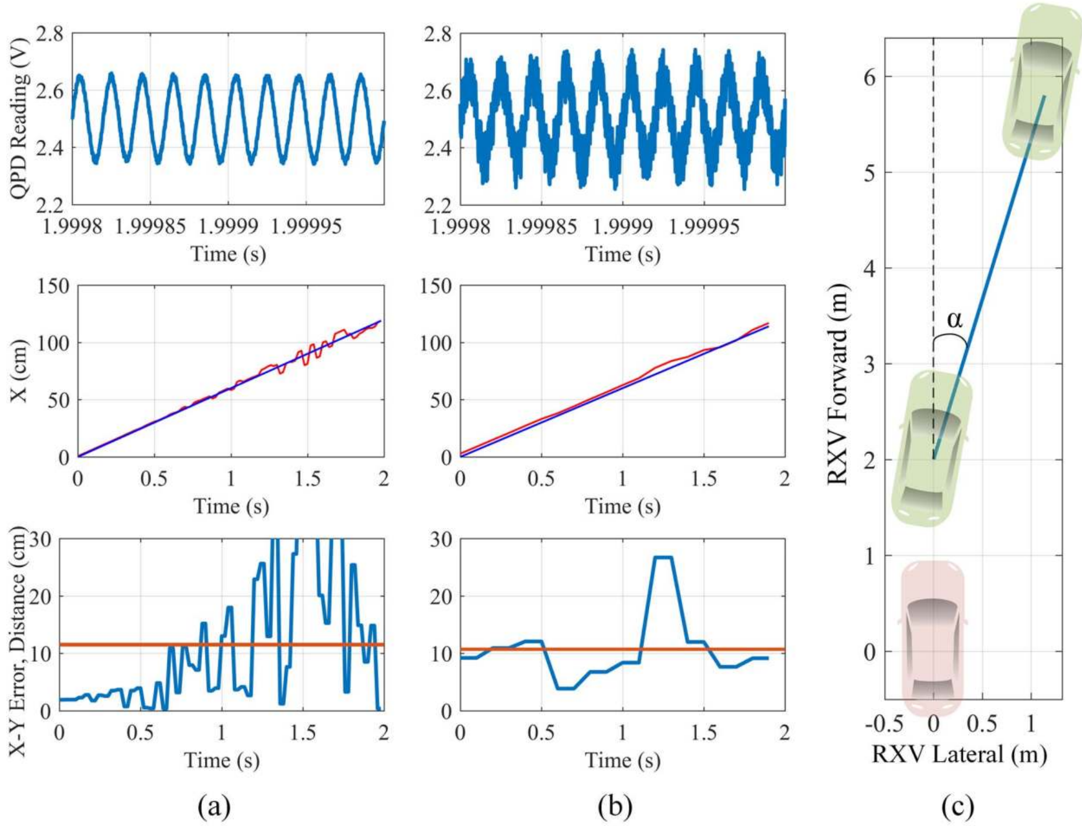

Figure 5.1: PA1, assessment of θ-SNR sensitivity. Target vehicle travels trajectory shown in (c) in 2 seconds ($\alpha_v = 16.7°$). Worst case SNR 20dB and VLP rate 50Hz in (a). Worst case SNR 2dB and VLP rate 10Hz in (b). Since the proposed VLP method infers the Y position result from X, their error performance is similar. Thus, only the time plot of X is shown. Mean error is ≈11 cm (orange line) under both the typical (a) and the extra noisy (b) channel conditions.

it needs an increased buffer time to average out the zero-mean AWGN component, but it increases positioning accuracy and stability. While the upper VLP rate limit is 500 Hz due to the sensing rate as stated in 5.1, there is no practical lower limit since vehicle dynamics are constant throughout this straight trajectory. The general lower limit for VLP rate can be regarded as the safety application requirement, which is ≥10 Hz for cooperative collision avoidance [Căilean and Dimian, 2017].

Fig. 5.2 summarizes effects of VLC SNR on VLP performance, showing that acceptable performance can be achieved even for very low worst-case SNR levels and very high VLP rates ($\gg$50 Hz) when the accuracy-rate trade-off is well utilized.

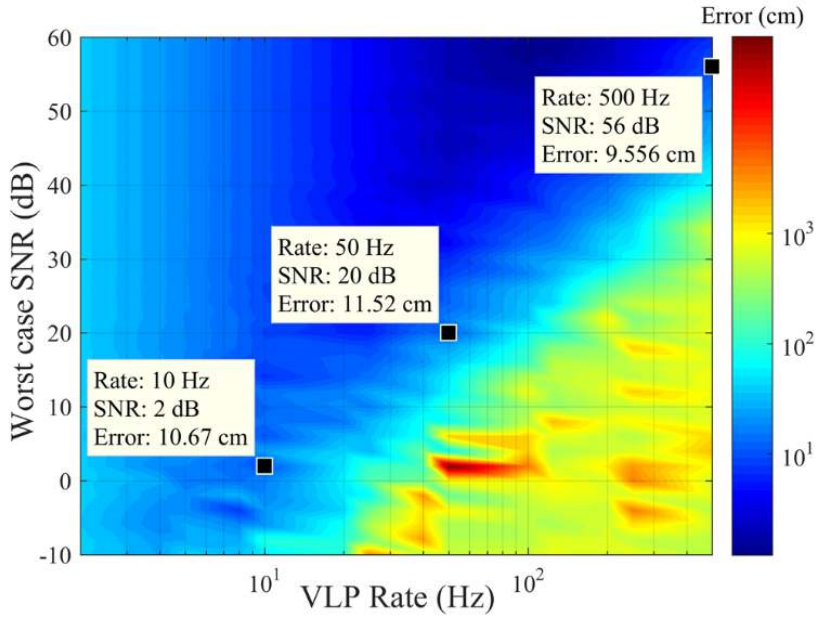

Figure 5.2: PA1, summary of the simulation in Fig. 5.1. Performance over different VLP rate and worst case SNR values are shown. The lower two data points belong to the results shown in Fig. 5.1.

PA1 - Effect of ψ and υ Sensor Inaccuracies on VLP

A large set of feasible target vehicle "mini-trajectories" within crash proximity of the ego vehicle (i.e., $\approx$10 m radius within the field-of-view of the RX) are tested in this simulation. For each mini-trajectory, which consists only of two consecutive relative target vehicle positions over Δt, the VLP error for a typical 50 Hz VLP rate and for different ψ and υ accuracy values are calculated, and average error over all mini-trajectories are saved. Mini-trajectories where $\frac{\Delta\theta}{\Delta t} \approx 0$ are excluded from this simulation since the term $(C2 - C1)$ in the denominator of Eqn. (4.6) approaches 0 when $\frac{\Delta\theta}{\Delta t} \to 0$, rendering the method numerically unstable. As stated before, the proposed VLP method requires two distinct consecutive θ measurements to function properly.

Fig. 5.3 demonstrates the effects of ψ and υ sensor accuracy on VLP performance (PA1) for all mini-trajectories, assuming perfect θ. Commercially available sensors provide accuracy levels of ≈0.3 km/h for speed and up to 0.02°- 0.1°for heading [Gade, 2016] at $\geq$ 500 Hz rates. The lower data point in Fig. 5.3 shows that for the best realizable ψ and υ accuracy (0.02°and ≈0.3 km/h respectively), the method provides cm-level accuracy at 50 Hz rate. Since ψ error is dominant and it multiplies with the distance traveled between consecutive samples, higher VLP rates decrease error. Hence, higher VLP rates would enable the use of even lower grade sensors for the same performance.

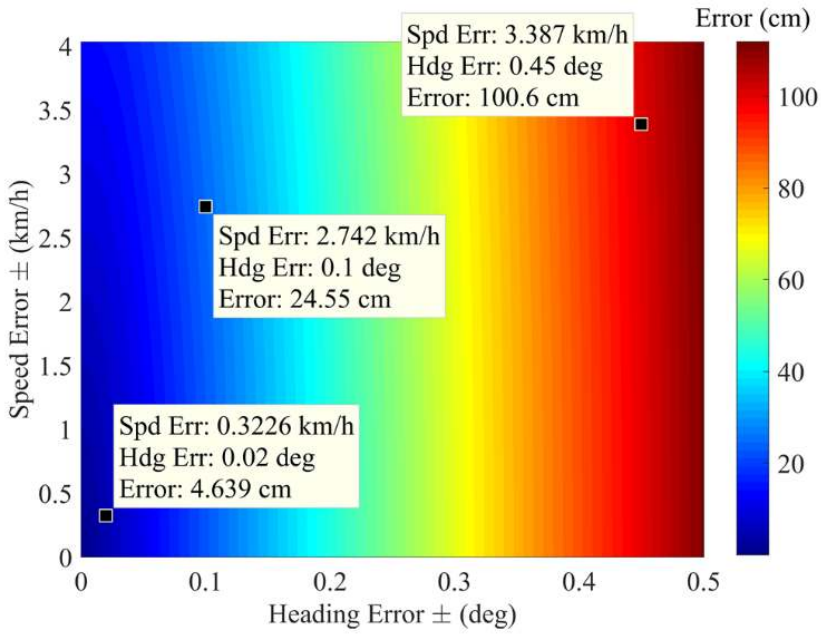

Figure 5.3: PA1, assessment of VLP sensitivity to ψ and υ accuracy. Data points are average VLP errors over all feasible mini-trajectories for each ψ and υ accuracy level.

PA2 - Sensing, VLC, VLP Rates vs. Vehicle Dynamics

Fig. 5.5 and Fig. 5.4 demonstrate the effects of PA2 on VLP performance for a partially curved trajectory where $(\frac{\Delta \alpha_v}{\Delta t}, \frac{\Delta v}{\Delta t}) = 0$ does not hold for all consecutive θ sample pairs on the trajectory. Worst-case SNR is set to 40 dB and ψ and v are assumed perfect to realistically minimize effects of PA1 and focus only on PA2, and a relatively fast VLP rate of 100 Hz is chosen for clearer demonstration of the condition in Eqn. (5.1). While the method performs well during Part I and III where vehicle dynamics are slower than VLP rate, the method starts to lose stability in Part II when the $\gg$ condition in Eqn. (5.1) starts to narrow for consecutive θ samples (i.e. $\frac{\Delta \alpha_v}{\Delta t}$ starts to increase), as shown in the middle part of the trajectory. Therefore, for faster vehicle dynamics, a higher VLP rate needs to be chosen while sacrificing noise mitigation. Additionally, the last part (IV) of the trajectory is arranged so that $\frac{\Delta \theta}{\Delta t} \approx 0$ to show that the method becomes numerically unstable under that condition.

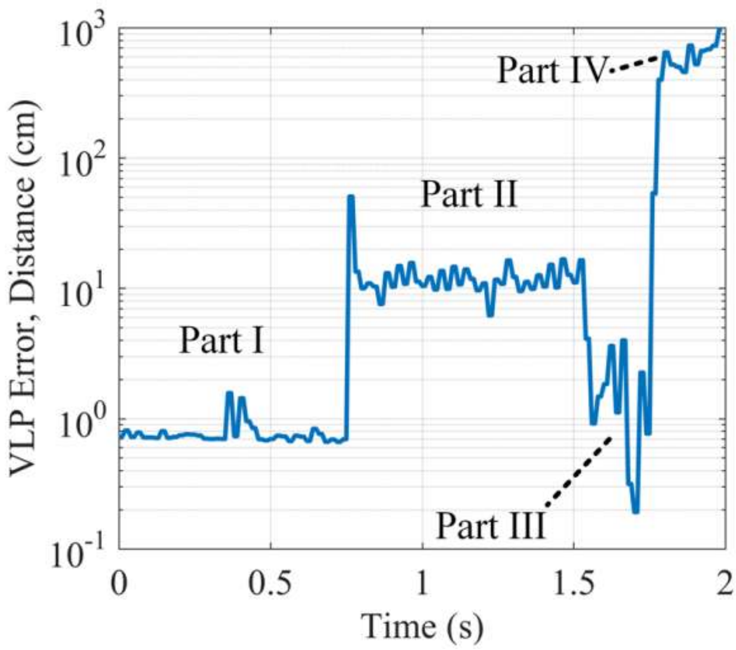

Figure 5.4: Simulation for the deterioration of PA2, VLP error.

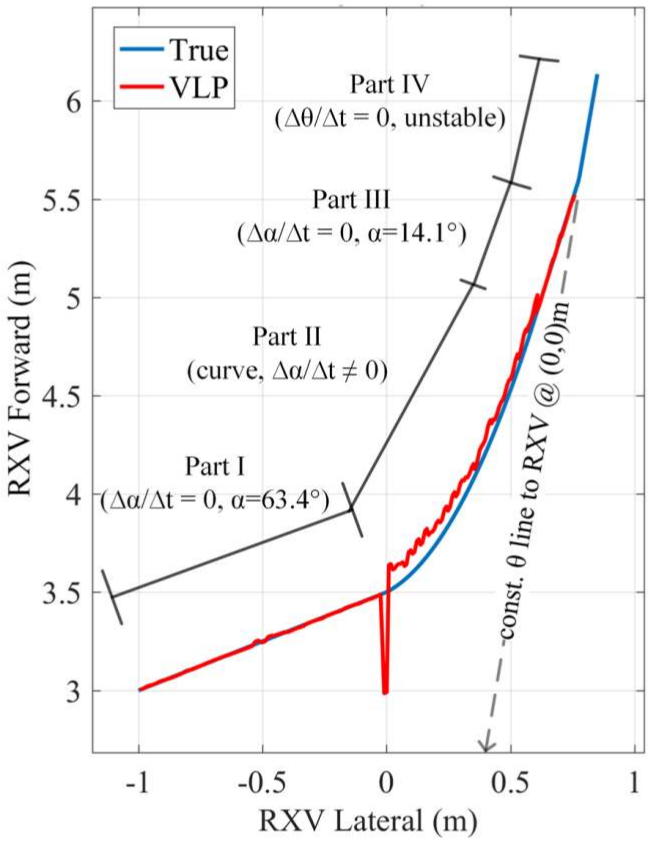

Figure 5.5: Simulation for the deterioration of PA2, trajectory.

5.2 *Evaluation and Analysis of the Direct Bearing-based Classical Position Fixing Algorithm*

The simulations in this section demonstrate the performance of the classical position fixing algorithm that uses direct bearing measurements from QRX, under realistic road and VLC channel conditions in typical collision avoidance and platooning scenarios as well as comparing its simulated performance to the theoretical CRLB on localization accuracy with dual-AoA-based VLP. First order ray optics are considered for the simulation of the QRX. A custom MATLAB©-based vehicular VLC simulator was built for this purpose, which is made available on GitHub [Soner and Coleri, 2021a]. The simulator utilizes ego and target vehicle trajectories for different scenarios and generates the signals that emanate from the two target TXs and reach the two ego QRXs, for the whole trajectory. The proposed method first uses the simulated received signals to measure the AoA from the TXs to the QRXs, and then provides relative localization based on these AoA measurements.

Simulator setup parameters are given in Table 5.1. The QRX design corresponds to the "best compromise" configuration, i.e., the yellow curve f_{QRX} in Fig. 3.3, but the photodiode dimensions in [Béchadergue et al., 2017] are used for fair comparison with existing results. In all simulations, the target vehicle leads the ego vehicle, thus, the target vehicle transmits through its tail light (similar to Fig. **??**). While the opposite configuration is equally valid, this configuration was chosen since it is the worst case scenario; the tail light has the lowest TX power among the vehicle lights. The simulated tail lights have 2 W optical power each and beam patterns are approximated by a Lambertian term of 20° half-power angle (order m=11) to be comparable to the setup in [Béchadergue et al., 2017], which utilizes a total of two 2 W head lights and a 1 W tail light for VLP. The TX modulation scheme (binary frequency shift keying, BFSK) and bitrate complies with vehicle safety application requirements [Căilean and Dimian, 2017, CAMP Vehicle Safety Communications Consortium, 2005]. A wide range of channel conditions, i.e., night-time versus day-time (indirect sunlight) light conditions, as well as clear versus foggy or rainy weather, are considered. Sunlight increases shot noise power as described in [Moreira et al., 1997], and fog and rain attenuates the signal power as described in [Grabner and Kvicera, 2013]. We present four simulated driving scenarios to demonstrate that the proposed solution is eligible for collision avoidance and platooning applications under all of these channel conditions:

- *SM1* - dynamic, collision avoidance. A target vehicle leading an ego vehicle on a highway brakes dangerously during a lane change and risks collision. Results for different estimation rates are shown to demonstrate the effect of rate on localization accuracy for a highly dynamic target vehicle.

- *SM2* - dynamic, platooning. A target vehicle joins a platoon by moving in front of the ego vehicle from the left lane, drives on the same lane for a short while, and then exits the platoon towards the right lane. Results under all combinations of day-time and night-time light, and clear, foggy and rainy weather are shown for 100 Hz localization rate to demonstrate the performance of the method against adverse conditions for typical vehicle trajectories that

Table 5.1: Simulator Setup Parameters

TX	Signal	BFSK, s_1, s_2: 5/6, 12/13 kHz
	Power	$\gamma_j \cdot \max(\lvert s_j \rvert) = 2$ W (tail light)
	Pattern	Lambertian, m = $\left\lfloor \frac{-\ln 2}{\ln(\cos(20°))} \right\rfloor = 11$
	Attenuation	clear: -
		heavy rain (≈10 mm/hr): 0.1 dB/m
		dense fog (≈200 m): 0.3 dB/m
QRX TIA	γ_i, g_m	0.5 A/W, 30 mS
	A_i (active) [a]	50 mm^2
	B, C_T, R_F	10 MHz, 45 pF, 2.84 kΩ, i.e., $G \approx 10$
	Factors	Γ=1.5 , I_{B2}=0.562 , I_{B3}=0.0868
	Temperature	T=298 K
	I_{bg}	night-time: 10 μA
		day, indirect sun: 750 μA
QRX Optics	Lens	PMMA (n=1.5), $d_L = 7.1$ mm
	QPD	$d_H = 6.3$ mm , $d_X = 0.55$ mm
	FoV	±50°linear, ±80°total (yellow, Fig. 3.3)
Vehicle	Dimensions	Length = 5 m. $L, D = 1.6$ m
	Steering	Ackermann (small sideslip angles)

[a] Detection area is 50 mm^2 in [Béchadergue et al., 2017] but converging/diverging optics usage is not specified. For fair comparison, QRX lens area, which is the detection area, is chosen as 50 mm^2 here, thus, QPD area is 39.7 mm^2 as per the design guidelines for QRX, and C_T is scaled accordingly.

occur during platooning.

- *SM3* - static, comparison with state-of-the-art (SoA) VLP. We simulate our method for the static vehicle locations described in [Béchadergue et al., 2017] under the same channel conditions. Results show that our method provides higher TX positioning accuracy for the high signal-to-noise ratio (SNR) regime under fair comparison, but [Béchadergue et al., 2017] is more resilient against low SNR. Additionally, the CRLB of the VLP algorithm is also evaluated for these locations to compare the theoretical and simulated performances.

- *SM4* - static, characterizing the operational range. This scenario considers the ego vehicle on the center of a 3-lane road and exhaustively simulates all feasible relative target locations under chosen favorable (i.e., night-time, clear) and challenging (i.e., day-time light, rain) channel conditions, characterizing the static accuracy of the method over its complete feasible operational range.

5.2.1 SM1 - Dynamic Scenario, Collision Avoidance

Fig. 5.6 demonstrates the performance of the proposed method in a collision avoidance scenario under day-time, clear weather conditions for different estimation rates. Results show that cm-level accuracy is achieved for all rates greater than 100 Hz for the middle part of the trajectory, which has the maximum risk of collision. Furthermore, when the relative target vehicle movement is slow, decreasing the estimation rate increases accuracy in the case of low SNR; this can be seen in the results for the beginning of the trajectory where the target tail lights are facing away from the ego vehicle, decreasing received SNR, and lower rates provide better accuracy. However, lower rates decrease estimation accuracy when the target is highly dynamic due to the phenomenon described in the problem definition; this can be seen in the results for the middle of the trajectory. These results demonstrate that the proposed method provides cm-level accuracy for a typical collision avoidance scenario under high noise channel conditions, and estimation rate can be adjusted with respect to the SNR and the relative mobility of the vehicles for improving performance.

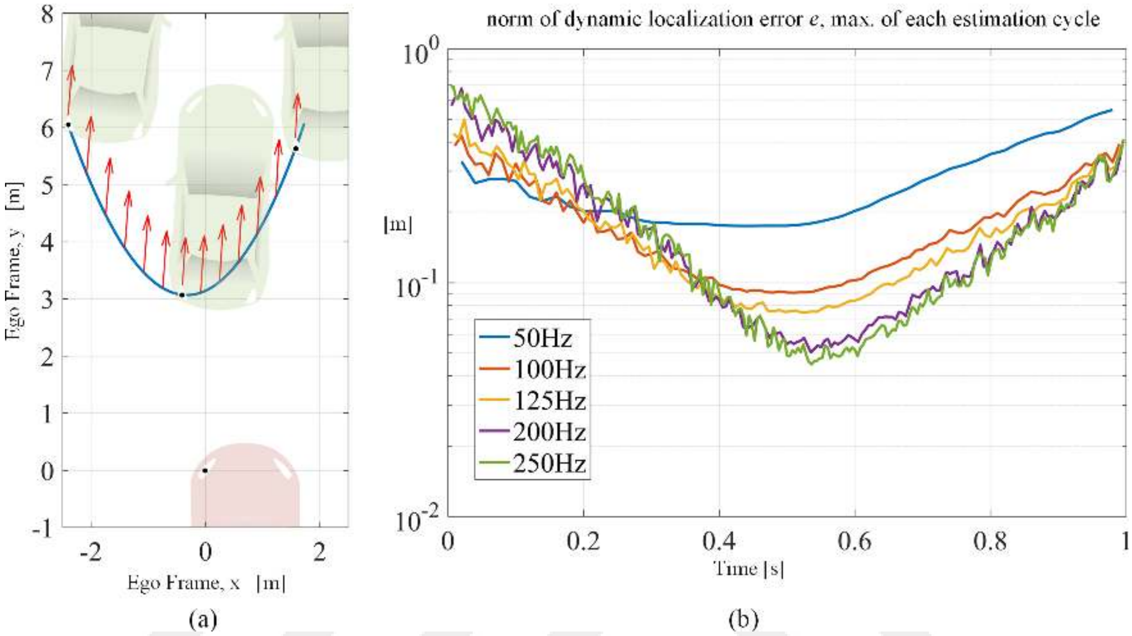

Figure 5.6: *SM1* - A typical collision avoidance scenario, dynamic vehicles. (a) Relative target vehicle trajectory. (b) Localization error, i.e., $||e||$ as per Eqn. (2.1), over the trajectory that runs for a simulation time of 1 s, for different estimation rates under day-time (indirect sunlight) clear weather conditions.

5.2.2 SM2 - Dynamic Scenario, Platooning

Fig. 5.7 demonstrates the performance of the proposed method for a platooning scenario (formation, straight road platooning, and dispersion) under clear, rainy and foggy weather conditions, and night and day ambient light for 100 Hz localization rate. Results show that while accuracy degrades severely due to sunlight and less severely due to fog and rain, cm-level accuracy is attained under all conditions for straight road platooning. Additionally, two practical irregularities of the proposed method are explicitly shown: 1) In the middle part of the trajectory, the SNR is very high and attenuation due fog and rain actually improves performance with respect to the clear weather case; this is because under night-time conditions, the signal power component in Eqn. (2.5b) is the dominant noise source, which decreases significantly with attenuation. 2) Towards the end of the scenario, the TX units start pointing away from the QRX units and cause loss of estimation, demonstrating a practical limit of the proposed method due to the small angular coverage by tail lights. These results collectively demonstrate that the proposed method is capable of sustaining the accuracy and rate required for localization in a comprehensive platooning scenario under adverse weather and noise conditions, despite practical limitations.

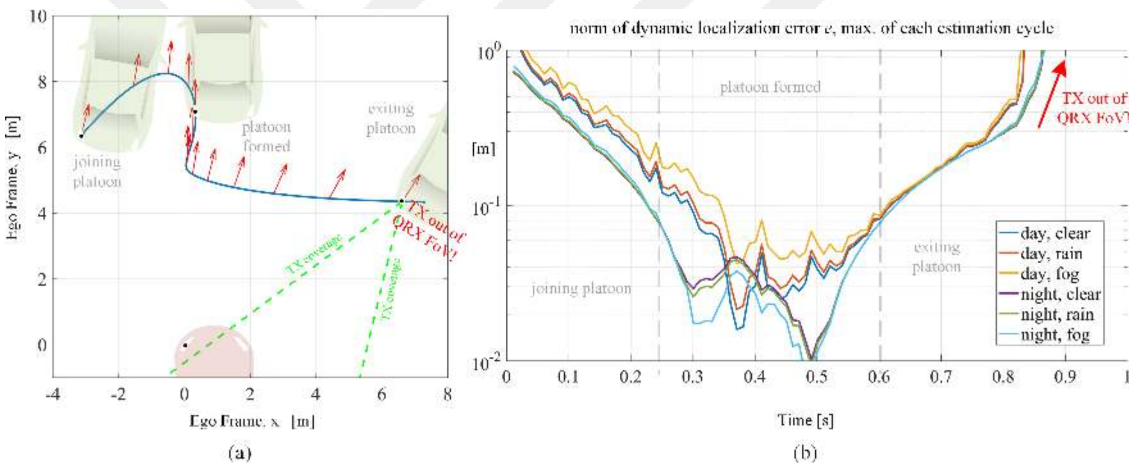

Figure 5.7: *SM2* - A typical platooning scenario, dynamic vehicles. (a) Relative target vehicle trajectory: Platoon formation, straight road platooning, and platoon dispersion over a simulation time of 1 s. (b) Localization error, i.e., $||e||$ as per Eqn. (2.1), over the trajectory, for different weather and ambient light conditions.

5.2.3 SM3 - Static Scenario, Comparison with Previous SoA VLP

This scenario demonstrates the performance of the proposed method for the static ego and target locations described in [Béchadergue et al., 2017] and depicted in Fig. 5.8a, under the same channel conditions. The following are addressed to ensure fair comparison:

- In [Béchadergue et al., 2017], vehicles are assumed to stay parallel throughout this scenario, which involves the target vehicle slowly moving from 0 to 3.5 m of lateral distance: This does not define a realistic vehicle movement since a non-zero heading difference is required unless the target vehicle drifts sideways throughout the whole trajectory. Hence, we assume that the vehicles are static at each location, and separately simulate performance at each location.

- In [Béchadergue et al., 2017], only results for a single TX on the target vehicle is provided. Therefore, we only consider the estimation of TX 1, i.e., $\widehat{p_1}$, for comparison, thus, the error vector in Eqn. (2.1) consists of e_1 only.

- The method in [Béchadergue et al., 2017] is evaluated for 2 kHz rate, and our method is evaluated for 50 Hz. We do not evaluate our method at 2 kHz (or equivalently, [Béchadergue et al., 2017] at 50 Hz) since lower rate improves the static accuracy of our method but degrades that of [Béchadergue et al., 2017] due to heterodyning as explained in [Béchadergue et al., 2017]. We therefore evaluate both methods with their best reported configuration that is acceptable as per collision avoidance and platooning requirements.

Fig. 5.8b demonstrates the x and y estimation performances of the proposed method, and Figs. 5.8c and 5.8d show the histogram of associated errors over the trajectory, sampled over 1000 iterations for higher statistical significance. While [Béchadergue et al., 2017] provides higher accuracy in the y axis on average over the whole trajectory, i.e., 6.2 cm error in [Béchadergue et al., 2017] versus 12.4 cm error in ours, our method provides superior accuracy in the x axis, i.e., 11.3 cm error in [Béchadergue et al., 2017] versus 3.2 cm error in ours. The difference in x and y estimation performance for our method is due to the difference in the sensitivities of the sin/cos non-linearities in Eqn. (4.2). In terms of overall 2D accuracy, our method provides better performance for the beginning of the trajectory, where the SNR is higher as shown in Fig. 5.8e, i.e., approximately 12.9 cm error in [Béchadergue et al., 2017] versus less than 10 cm error in ours. However, [Béchadergue et al., 2017] is

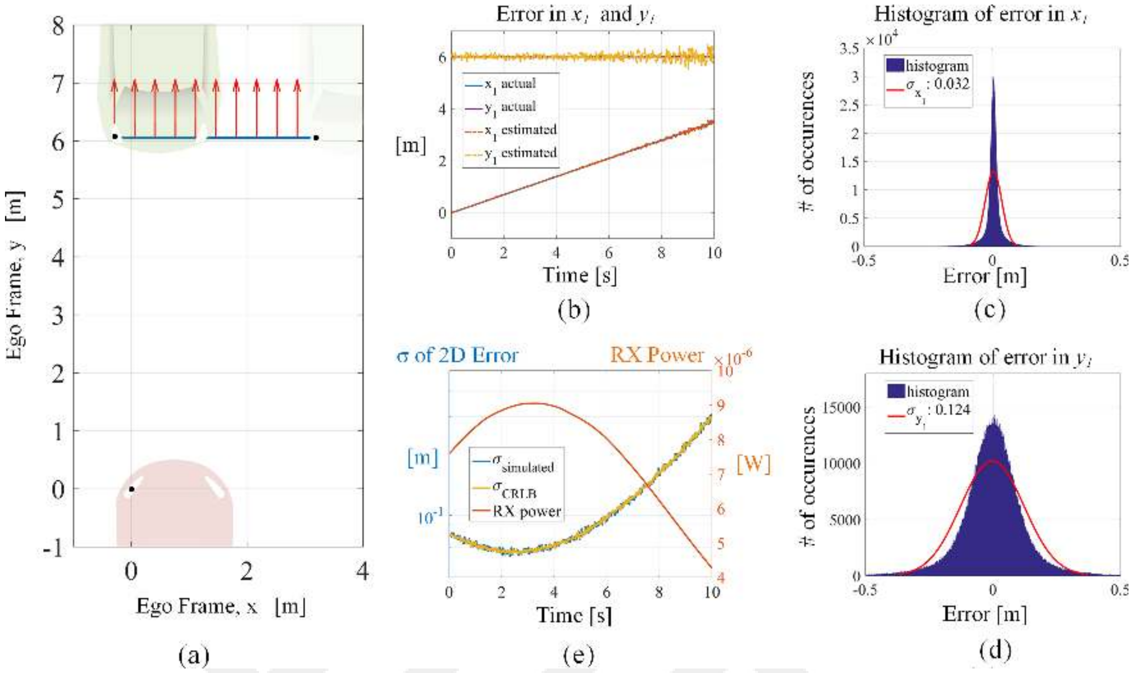

Figure 5.8: *SM3* - Comparison with SoA VLP. (a) Locations in [Béchadergue et al., 2017]: Vehicles are parallel and static at each simulation time step. (b) x and y estimation results for only $\widehat{p_1}$, under the same noise conditions in [Béchadergue et al., 2017]. (c) Localization error and the associated theoretical CRLB. Histogram of errors in (d) x, and (e) y.

more resilient against noise and sustains this performance for also the lower SNR regime at the end of the trajectory, contrary to our method. Additionally, the CRLB of our method is evaluated since static locations are considered. Simulated accuracy meets the CRLB as shown in Fig. 5.8e, demonstrating that the proposed VLP algorithm is an efficient estimator, i.e., the minimum variance unbiased estimator for the dual-AoA vehicular VLP problem. These results show that our proposed method advances the state-of-the-art for vehicular VLP with cm-level localization accuracy and 50 Hz rate under realistic road and channel conditions except for very low SNR. Furthermore, our proposed method does not impose any high-bandwidth circuit requirements like [Béchadergue et al., 2017] and is therefore feasible for general use.

5.2.4 SM4 - Characterizing the Operational Range

The procedure for this scenario is as follows: Estimation accuracy for sampled relative target vehicle locations over three lanes (±3 m horizontal distance from ego vehicle bumper center) and 15 m longitudinal distance are evaluated to characterize the feasible operational range of the proposed method for collision avoidance and platooning scenarios, where the recorded performance for each location is an average of the results for all feasible target orientations at that location. The estimation rate is 50 Hz. Figs. 5.9a and 5.9b demonstrate localization accuracy under favorable and harsh conditions, i.e., night-time clear weather, and day-time heavy rain (10 mm/hr), respectively. The colorless zones in the graphs denote a loss of estimation for those locations due to QRX units being out of TX coverage, which occurs due to the target vehicle being either too close to the ego front bumper (less than 1 m), or at an angle too oblique to be considered as either a platoon element [Jootel, 2012] or a tangible collision threat [DESTATIS, 2017]. Therefore, these locations are not strictly relevant for collision avoidance and platooning scenarios. Fig. 5.9a shows that for favorable channel conditions the promised cm-level accuracy is attained within approximately a 7 m radius. Outside the 7 m radius, up until the 10 m mark, accuracy is still better than 1 m. On the other hand, under harsh channel conditions, cm-level accuracy is limited to a radius of approximately 5 m, as shown in Fig. 5.9b. The accuracy is still better than 1 m up to the 8 m mark. These results demonstrate that the proposed method provides cm-level accuracy with at least 50 Hz rate even under harsh channel conditions for configurations relevant for collision avoidance and platooning within approximately 10 m range.

Considering these results, a rough comparison of vehicle localization methods that considers the same distance range and FoV, in terms of computational complexity, accuracy and rate, is provided in Table 5.2. While RADAR-based methods can provide up to 10 cm accuracy, they have significantly high complexity, thus, typically low rate even with SoA computational optimizations, due to the large number of receiving elements used (typically more than 1000 antennas in phased-array form), as thoroughly described in [Li et al., 2019]. Camera-based methods

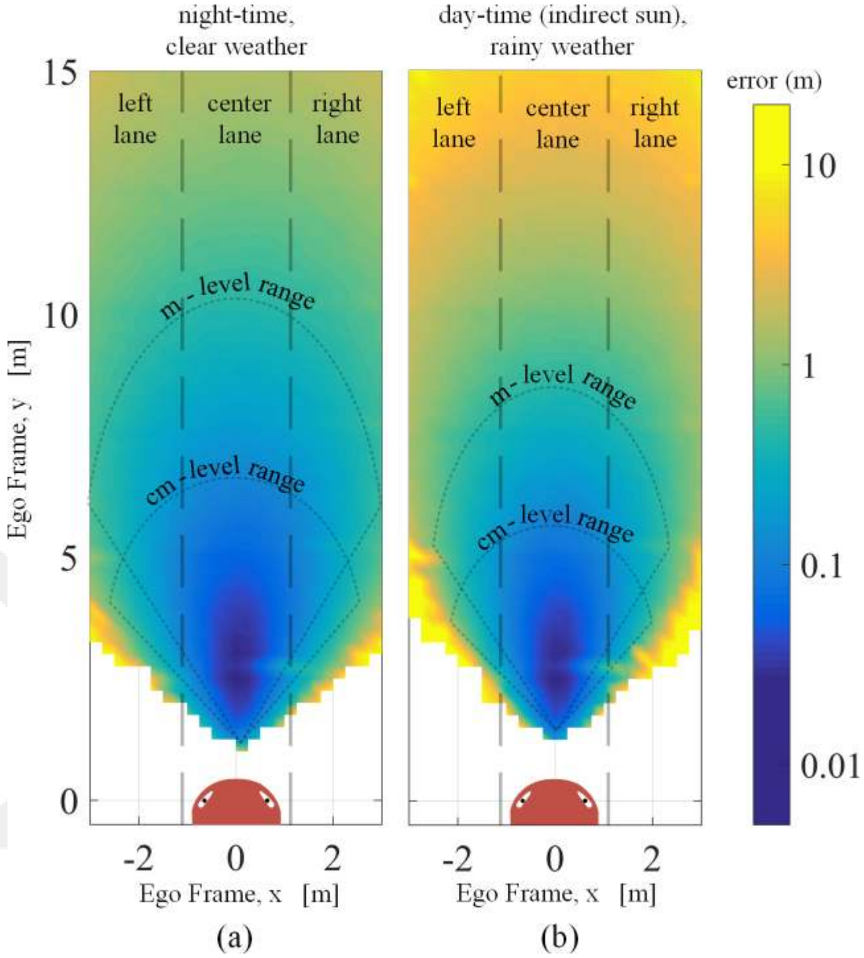

Figure 5.9: *SM4* – Characterizing the operational range for a 3-lane road scenario (static locations). Results for each location show average error over all feasible target orientations for 50 Hz localization rate, under (a) night-time, clear weather conditions, and (b) day-time, rainy weather conditions.

provide cm-level accuracy but suffer even more from the high number of receiving elements (i.e., typically more than a million pixels), thus, are fundamentally limited to low rates considering a feasible cost margin for automotive use [Janai et al., 2020b]. VLC-based methods are multiple orders of magnitude less complex than sensor-based methods since very few receiving elements, situated at known locations on the vehicles, are used, enabling real-time service; the complexity analysis of our proposed method provided in Eqn. (3.6) showcases the simplicity of VLC-based methods. Furthermore, our proposed VLC-based method attains similar accuracy as its best alternative, the RToF-based VLP in [Béchadergue et al., 2017], but without imposing requirements that restrict practical use as in [Béchadergue et al., 2017].

Table 5.2: Comparison of vehicle localization methods

Method	# of ops / cycle	Error	Rate
Our method	$\approx 10^5$	≤ 10 cm	≥ 50 Hz
RToF-VLP [Béchadergue et al., 2017]	$\approx 10^5$	≤ 10 cm	≥ 50 Hz
RADAR [Li et al., 2019]	$\approx 10^7$	≥ 10 cm	≈ 50 Hz
Camera [Janai et al., 2020b]	$\approx 10^9$	≈ 10 cm	≤ 50 Hz

5.3 State-of-the-Art Vehicular VLP Performance Benchmark

The performance benchmark simulations consist of numerical evaluations of the derived CRLBs as well as the actual estimations by all of the algorithms, under realistic collision avoidance and platooning scenarios and challenging weather and VLC channel noise conditions. These evaluations demonstrate the robustness of the positioning algorithms against VLC channel noise as well as the effects of mobility on estimation performance. A custom simulator was built for this purpose in Python language and all related source material (i.e., code and related documentation) is made available on GitHub [Soner and Coleri, 2021b].

Simulator setup parameters are given in Table 5.3. In all simulations, a leading target target vehicle transmits VLC signals from its tail light towards the ego vehicle (Fig. 2.7); this is the worst case scenario since taillights have lower power than headlights. The taillight has 2 W optical power, a Lambertian pattern with 20° half-power angle (order m=11) and pure tone modulation at 1 MHz [Béchadergue et al., 2016] which is the realistic pass-band limit for current high-power automotive LEDs.

The signal is band-pass filtered at 100 kHz bandwidth around the 1 MHz carrier on the RX end as in [Béchadergue et al., 2019]. To facilitate fair comparison and practical relevance, all methods are configured for 100 Hz positioning rate (i.e., the rate requirement is satisfied, and simulations test the accuracy requirement), ADCs have a moderate 10 MSPS conversion rate, and all methods utilize the "QRX" unit: QRX was designed for bearing-based positioning, but it can accommodate all of the algorithms since range-based methods can simply use the sum of the RX signals at all quadrants (Delay due to refraction on the lens is negligible compared to the channel propagation delay since the lens-sensor distance is on the order of millimeters). To further improve practical relevance, we choose a very simple plano-convex lens from the Edmund Optics catalog (#67-149) during QRX design, and accordingly tune for $\approx \pm 60°$ FoV using high-fidelity ray-optics simulations [1]. A wide range of realistic ambient light induced noise conditions (night, day, direct sunlight [Moreira et al., 1997]) and weather-induced attenuation conditions (clear, foggy, rainy [Grabner and Kvicera, 2013]) are considered in the simulations.

Accordingly, we present five evaluation scenarios (*ES#*):

- *ES1* - static scenario. We simulate the two range measurement techniques used in vehicular VLP, i.e., auto-digital [Béchadergue et al., 2016] and DFT-based [Roberts et al., 2010], for target vehicle locations on a 1-20 m straight test-track (i.e., bearing=0) to characterize and compare their performance.

- *ES2* - static scenario. We evaluate CRLBs of all classical position fixing methods at various target vehicle locations over the operational range for theoretical analysis of classical position fixing performance, where the vehicles stay longitudinally parallel for fair comparison between methods utilizing direct and differential measurements.

- *ES3* - dynamic scenario. We simulate running position fixing methods for direct bearing and range measurements under a typical lane change scenario

[1] https://github.com/mjhoptics/ray-optics, not a first order simulation this time.

to evaluate the effects of mobility on their performance.

- *ES4* - dynamic scenario. We simulate the best performing estimators from *ES1-ES3* for the platooning scenario described in Section 5.2.2 under various weather and noise conditions to characterize state-of-the-art vehicular VLP performance for platooning.

- *ES5* - dynamic scenario. We repeat *ES4* for a recorded collision threat scenario

Table 5.3: Simulator Setup Parameters

TX	Signal	pure tone, 1 MHz
	Power	$\gamma_j \cdot \max(\lvert s_j \rvert) = 2$ W (tail light)
	Pattern	Lambertian, m = $\left\lfloor \frac{-\ln 2}{\ln(\cos(20°))} \right\rfloor = 11$
	Attenuation	clear: -
		heavy rain (≈10 mm/hr): 0.1 dB/m
		dense fog (≈200 m): 0.3 dB/m
QRX	γ_i, g_i, A_i [a]	0.5 A/W, 30 mS, 31.2 mm^2
	B_i, C_i, R_i	10 MHz [b], 45 pF, 2.84 kΩ, i.e., $G \approx 10$
	Factors	Γ=1.5 , I_{B2}=0.562 , I_{B3}=0.0868
	Temperature	T=298 K
	$I_{bg,i}$	night-time: 10 μA
		day, indirect sun: 750 μA
	Lens	N-BK7 (n=1.52), diameter = 9.0 mm
	Detector	d_H = 6.3 mm , d_X = 1.9 mm
	FoV	±60°, see Chapter 3
Vehicle	Dimensions	Length = 5 m. L = 1.6 m
	Steering	Ackermann (small sideslip)

[a] This is the area of the aperture stop, which is 6.3 mm in diameter.

[b] This is ADC output, but effectively, B_i = 100 kHz due to filtering [Béchadergue et al., 2019].

extracted from the INTERACTION dataset [Zhan et al., 2019] to characterize state-of-the-art vehicular VLP performance for collision avoidance; A leading target vehicle brakes abruptly while merging onto a highway, risking collision with the ego vehicle that follows it. A video of this scenario is provided in [Soner, 2021].

5.3.1 ES1 - Characterizing Range Measurement Techniques

Fig. 5.10 shows the sampled standard deviation of the ranging error for the two range measurement techniques, i.e., auto-digital [Béchadergue et al., 2016] and DFT-based [Roberts et al., 2010], for static target vehicle locations on a 1-20 m straight test track under both favorable and adverse weather conditions. Since the auto-digital technique is susceptible to systematic error due to both quantization and heterodyning [Béchadergue et al., 2018], we make two arrangements to observe the effect of channel noise in isolation: 1) The true range values on the test track are chosen to be exact multiples of the resolution limit of the auto-digital technique to avoid systematic quantization error (statistical quantization error due to noise will still be present), and 2) each point on the test-track is simulated with a fixed time window that is free of heterodyning error by definition. The auto-digital technique is tuned to ≈0.75 cm resolution for 100 Hz measurement rate (r=5000, N=4, f_{clock}=100 MHz with the notation in [Béchadergue et al., 2016]), which results in a ≈10 ms simulation time window for each point on the test track.

Results show that the DFT-based technique is more accurate even in the face of SNR drop throughout the test-track (i.e., with increasing range since TX power is constant) and also with worsening weather conditions. Furthermore, the quantization effect of the auto-digital technique is also seen: At the 1 m true range mark in the clear-night scenario, the output of the auto-digital technique does not change among different samples since none of the noise samples are big enough to shift the output from the same quantization interval, causing standard deviation to be 0 (the 2.5 m mark sample shoots down towards negative infinity, which is virtually where the 1 m sample is on the logarithmic vertical axis). Therefore in this specific case, the auto-digital technique produces a perfect output, but this only happens because the target vehicle was positioned at an exact multiple of the resolution limit, which is a very scarce occurrence in high-mobility road scenarios. In summary, the more complex DFT-based technique is more accurate than the auto-digital technique against channel noise, making it a better fit for range measurements in vehicular VLP when complexity requirements are not stringent.

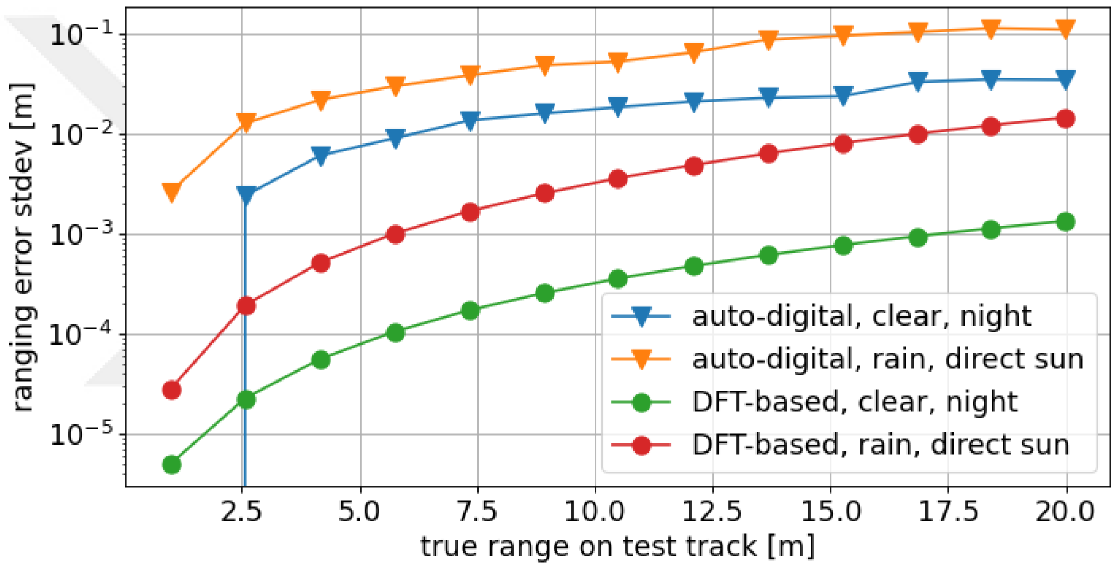

Figure 5.10: *ES1* - Performance of the two range measurement techniques [Béchadergue et al., 2016, Roberts et al., 2010] on a 1-20m straight test-track under various weather conditions.

5.3.2 ES2 - CRLBs for Classical Position Fixing

In this evaluation scenario, the target vehicle is positioned at various locations within a <20 m radius of the ego vehicle (i.e., bearing≠0) at longitudinally parallel orientation. At each target vehicle location, the parameter measurements are simulated over multiple iterations of the noise process, and the resulting parameter measurement distributions are used for evaluating the CRLB on positioning accuracy for each method. This is repeated under favorable and adverse noise and weather conditions like in (*ES1*) to observe performance under best and worst case scenarios.

Fig. 5.11a shows the test locations, Fig. 5.11b and c show the standard deviations as predicted by the CRLB in the lateral (x) and longitudinal (y) axes, respectively, for clear weather at night. Fig. 5.11d and e show the same for rainy weather and high noise due to direct sunlight exposure on the detectors. Moreover, the outputs of the MLE position estimation algorithms are also sampled to test the proposal about the MLE algorithms derived in this thesis converging to the MVUE for their respective problems. The results empirically support this MVUE claim since the sampled outputs of the MLE algorithms all approximately match their respective CRLBs. However, as also shown in the inset in Fig. 5.11e, the extremely high noise and attenuation at the farthest points on the track cause a significant non-zero bias on the methods based on differential measurements, which makes those methods virtually unusable at high noise.

In summary, the results show the following: 1) direct measurements provide higher robustness against channel noise, thus, are more suitable than differential measurements for high accuracy in vehicular VLP methods, and 2) range-based and bearing-based methods are complementary since the former provides the highest accuracy against noise in the y axis, while the latter does the same in the x axis.

5.3.3 ES3 - Characterizing Running Position Fixing Methods

Fig. 5.12 shows the sampled standard deviation and mean error for running position fixing methods using bearing and range measurements during a typical lane change maneuver by a target vehicle under favorable weather and noise conditions (clear weather, night-time). During the maneuver, the target vehicle first merges onto the lane of the ego vehicle (i.e., target relative heading and speed changes very slowly compared to the 100 Hz estimation rate up to the 0.5 s mark), and then starts to speed up while aligning itself onto the lane (i.e., heading and speed start changing significantly after 0.5 s).

Results for the first part of the trajectory, i.e., when vehicle dynamics are slowly

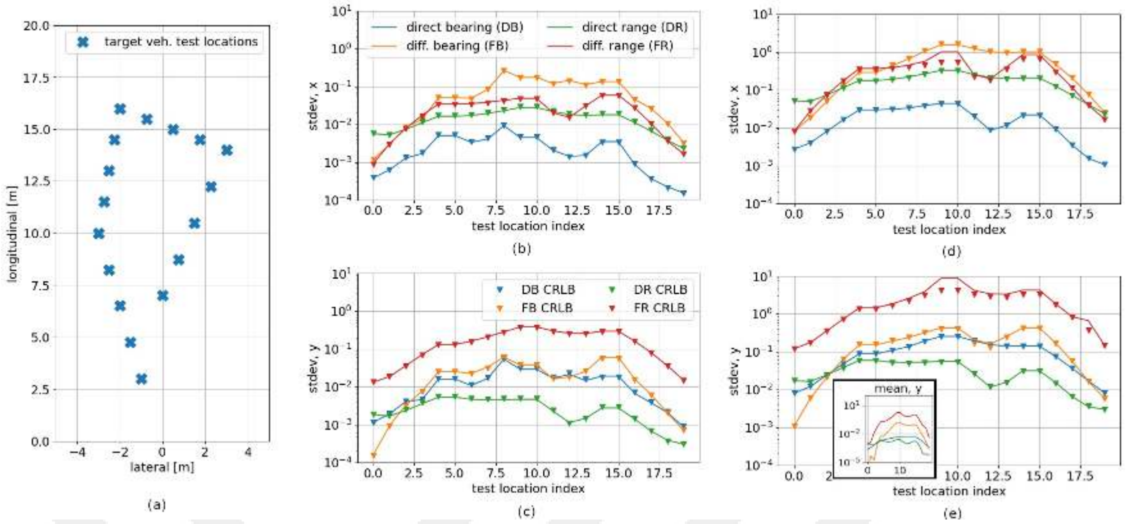

Figure 5.11: *ES2* - CRLBs and sampled estimator performances for classical position fixing methods evaluated for test locations shown in (a) under clear weather night time conditions in (b) and (c), and under heavy rain and direct sunlight exposure on the detectors in (d) and (e). Test location indices start from the bottom-most location shown in (a) and go around the track in clockwise direction.

changing, show that current running methods can provide high accuracy when bearing and range based positioning is used in complementary fashion for the x and y axes respectively, just like in the classical fix case. However, the second part of the trajectory induces a significant error for both bearing and range based methods irrespective of the noise conditions since these two-time-step methods inherently assume slowly changing vehicle dynamics. Therefore, these methods only provide sufficient accuracy when estimation rate is significantly faster than the change in vehicle dynamics. While vehicular VLP methods utilizing such measurement models can easily determine whether or not this condition is present at runtime by observing the trends in $\widehat{a_v}$, $\widehat{d_v}$ and SNR, it is clear that the existing running position fixing methods that only use two consecutive time steps for estimation do not provide satisfactory performance under all conditions.

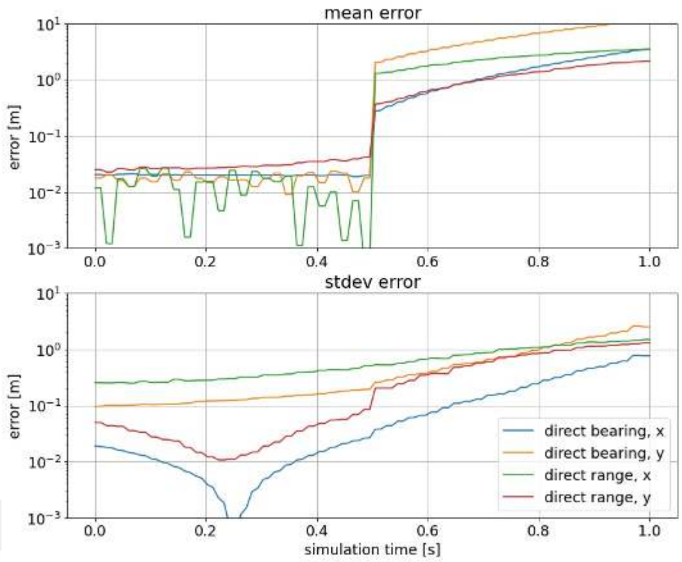

Figure 5.12: *ES3* - Evaluation for running position fixing methods under a dynamic lane change scenario

5.3.4 ES4 - High-Mobility Platooning Scenario Simulation

Fig. 5.13 shows the sampled standard deviation and mean of 2D error (as defined in Eqn. (2.1)) when classical position fixing is used with direct bearing measurements for estimating x and with direct range measurements for estimating y, during a high-mobility platooning scenario under all weather and noise conditions considered in this thesis. Each mean error data point shows the maximum error occurring within that estimation interval to show the effect of the finite-rate estimations not being able to "catch up" with the fast-moving target vehicle. This mobility-induced error appears only in the mean of the error since it is deterministic and unknown, i.e., it's the same for each iteration of the noise process; the standard deviation of the error shows the effect of channel noise.

Results show that despite the challenging conditions, the direct bearing-range hybrid classical fix method evaluated in this scenario provides nearly cm-level accuracy under all conditions, proving its eligibility for safe platooning applications.

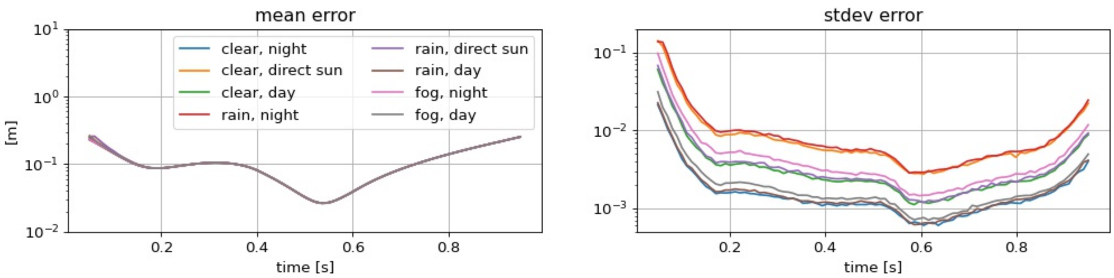

Figure 5.13: *ES4* - Evaluation of classical position fixing performance in a platooning scenario under all weather and noise conditions. The method uses direct range measurements for y estimation and direct bearing measurements for x estimation.

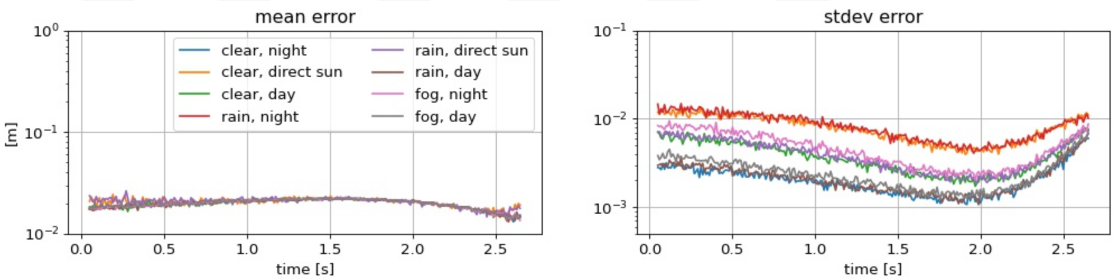

Figure 5.14: *ES5* - Repeating *ES4* for a recorded collision threat scenario from the INTERACTION dataset [Zhan et al., 2019, Soner, 2021].

5.3.5 ES5 - Collision Avoidance Scenario Simulation

Fig. 5.14 shows the results for *ES5*, which repeats *ES4* for a recorded collision threat scenario extracted from the INTERACTION dataset [Zhan et al., 2019]. A video of the scenario can be found in [Soner, 2021]. While the mobility level in this scenario is lower than that in *ES4*, the trajectory here is taken from actual vehicles on a road, which improves the practical relevance of the simulations. Results show that the direct bearing-range hybrid method again provides cm-level accuracy under all conditions, proving its eligibility for also collision avoidance applications.

Chapter 6

CONCLUSION

In this section, we summarize the findings in this thesis, list the related publications, present remaining important open questions and challenges for the widespread deployment of vehicular VLP, and list our associated conclusions.

6.1 Open Questions and Challenges

We start with the open questions and challenges, and group them under the following categories: 1) further performance improvements and analyses for vehicular VLP, 2) integration of vehicular VLP into the currently evolving "connected and autonomous vehicle" (CAV) software stack and enabling its widespread deployment in thereof, and 3) co-design of vehicular VLP with sensor systems to enable better localization for upstream applications.

6.1.1 VLP Performance Improvements and Further Analyses

One of the main shortcomings of current vehicular VLP methods is insufficient FoV: The current setups that consider only front and rear-facing VLC units cannot detect pure side collision threats [Kaempchen et al., 2009, DESTATIS, 2017]. Although existing methods can be adapted for detecting such collisions via additional RX units on the sides [Eldeeb and Uysal, 2019], the effectiveness and regulation compliance of such configurations are yet to be investigated. Moreover, current classical position fixing methods have dead zones within their FoV limiting their coverage: target TXs need to be inside the FoVs of both RXs at the same time for a fix. Therefore, developing better running position fixing methods or hybrid bearing/range classical methods that use a single RX (similar to radial and distance measurement equipments (DMEs) in aviation [Kelly and Cusick, 1986]) are important directions for improving vehicular VLP FoV.

Another important line of research is further improving the accuracy and rate of vehicular VLP methods: Using an extended set of measurements by adding more RX units or taking more samples over time and solving over-determined systems of equations (i.e., $N_H > N_M$, typically via least-squares) is a promising research direction, and has recently seen some elementary progress [Xu and Xu, 2019]. Other promising research directions include new RX optical and electrical configurations [Căilean et al., 2020] and parameter measurement techniques (e.g., via positioning-motivated visible light waveform design [Yazar and Gezici, 2022]) with higher robustness against noise, and further "environment-aware" methods that sense and adapt to channel conditions for higher accuracy [Căilean and Dimian, 2016]. The theoretical performance of such new techniques can be investigated via the generalized bounds derived in [Keskin et al., 2017], and the positioning performance they enable can be evaluated via the CRLBs derived in this thesis.

Lastly, we note that experimental studies in this area are currently very limited [Yu et al., 2013, Béchadergue et al., 2019, Béchadergue et al., 2018]. Although theoretical and simulated analyses done so far have provided a good basis for understanding vehicular VLP performance in realistic scenarios, comprehensive experimental studies on the road are still necessary for fully characterizing vehicular VLP performance with actual regulation-compliant headlights that have asymmetric intensity distributions [Memedi et al., 2018, Memedi et al., 2017].

6.1.2 Integration and Widespread Deployment of Vehicular VLP

The integration of communication-based positioning methods into the vehicular domain is still an open field. Unlike RF [Alam and Dempster, 2013], VLP can provide the required accuracy for collision avoidance and platooning applications, but on-vehicle VLC TX and RX units are not ubiquitous yet. Moreover, the position of VLC technologies within the automotive software stack is not clear yet since the stack itself is currently evolving to accommodate "V2X" connectivity and autonomy [Fletcher et al., 2020]. VLP could either be a standalone localization service or it could exist as an extension of the VLC service without compromising communication functionality [Yang et al., 2020] within these lines. Further research on this aspect is necessary since this choice has implications for the newly developed safety-relevant automotive software standards (e.g., ISO/PAS 21448, SOTIF [Kirovskii and Gorelov, 2019]) as well as for future-proofing [Herschfelt et al., 2020].

One other related challenge, which might be regarded as the holy grail in this area, is attaining modulation-free VLP. Modulation-free VLP considers the detection of random LED intensity fluctuations which occur due to various random noise factors such as power supply switching noise; once the LED is detected, range and/or angle measurements can be done, and the vehicular VLP methods discussed in this thesis can be applied for positioning. Since this would enable the localization of "legacy" vehicles that do not carry dedicated VLC TX modulators, it would vastly improve the adoption speed of vehicular VLP in the automotive sector. While there have been indoor VLP works towards this direction primarily by utilizing so-called "signals of opportunity" [Bastiaens et al., 2020], this highly valuable technology is still an open question for vehicular VLP.

6.1.3 VLP-Sensor Co-design and Upstream Applications

Vehicular VLP and sensor-based systems can also be jointly designed to exploit localization performance gains from both sides in future studies since they have "orthogonal" performance attributes. For example, VLP position estimations can be used as a new grounding modality for improving the performance of vision-based target trackers [Janai et al., 2020a] and trajectory prediction models [Zhao et al., 2019]. Since current examples of such systems typically do grounding by bootstrapping on the same modality (e.g., they utilize *a priori* known features from the same source image for grounding [Deng et al., 2018]) which further increases the complexity and decreases rate, they could significantly benefit from a new modality like VLP that is low complexity, high rate and high accuracy.

Similarly, VLP-based collision avoidance and platooning systems could also benefit from sensor systems: The results in this thesis have shown that one of the main sources of error in vehicular VLP is due to the estimations not being able to catch up with the high-mobility target vehicle. Since this component changes relatively slowly compared to sensor rates as explained in [Soner and Coleri, 2021c], inertial and visual sensor-based probabilistic trajectory prediction methods (e.g., from SLAM literature [Ziegler et al., 2014, Nieto et al., 2006, Bailey and Durrant-Whyte, 2006]) can be used for mitigating this mobility-induced error in VLP. The investigation of the collaboration between such sensor-based methods and vehicular VLP methods for improving localization performance in autonomous driving, is a highly promising future research direction.

The primary upstream application for the material presented in thesis, especially the QRX design, is MIMO VLC. The QRX could be used for MIMO VLC similar to [Wang et al., 2013a], but with additional positioning capability, for a variety of domains. For instance, source separation could be applied on the received signals on all quadrants, and bearing to each separated source could be measured as described in Chapter 3. Measured bearing information for each source can be used for improving MIMO detection and decoding performance in challenging environments. Furthermore, as detailed in the proof-of-concept experimental study in Chapter 3, the QRX could be used simultaneously for tracking/pointing and physically secure VLC for UAVs. This application could also benefit from the VLP capability that comes with the QRX for coordination and localized control in swarm configurations.

6.2 Summary of the Findings in this Thesis

This thesis reviewed the state-of-the-art in vehicular VLP, proposed a new receiver design ("QRX") and four new associated positioning algorithms (one of which significantly advanced the state-of-the-art, namely, classical position fixing using direct bearing measurements from the novel QRX receiver), analyzed the performances of all methods under challenging and realistic road scenarios, and discussed future challenges faced for widespread deployment of vehicular VLP. The CRLBs derived for theoretical analyses of the all algorithms can be used for evaluating the positioning performance of potential new parameter measurement techniques in the future. The simulation results in the thesis show that classical position fixing methods with direct range measurements for longitudinal and direct bearing measurements for lateral coordinate estimations can satisfy the accuracy and rate requirements of collision avoidance and platooning applications under nearly all weather and noise conditions, proving their eligibility. Although single-RX running position fixing methods effectively promise FoV improvements and differential measurements promise alleviating target co-operation restrictions, current methods in those categories cannot provide sufficient accuracy under all realistic conditions, warranting further development in those directions.

Open challenges for vehicular VLP research includes environment and noise-adaptive operation and further analyses of performance under different use cases, including comprehensive experimental studies. Furthermore, integration of vehicular VLP as a relative vehicle localization technology into the modern CAV software stack is an important topic that requires attention from both the academia and the industry due to its implications for standardization of safe autonomous driving. Similarly, practical challenges such as increasing the FoV of vehicular VLP methods to enable side collision detection, and finding new signal-of-opportunity based target detection methods that do not require explicit LED modulation to enable positioning of "legacy" vehicles without VLC hardware, require further development efforts.

Solutions to these problems and challenges would free vehicular VLP of its technical restrictions and induct it into the vehicular localization framework alongside sensor-based methods. This would pave the way for the ultimate goal in vehicular VLP, which is complementing and improving sensor-based vehicle localization systems for fully autonomous collision avoidance and platooning applications.

6.3 List of Publications

The following first author publications resulted from the works in this thesis:

1. [Soner and Coleri Ergen, 2019c]: Soner, B., and Coleri Ergen, S. (2019, September). Vehicular visible light positioning with a single receiver. In *2019 IEEE 30th Annual International Symposium on Personal, Indoor and Mobile Radio Communications (PIMRC)* (pp. 1-6). IEEE.

2. [Soner and Coleri Ergen, 2019a]: Soner, B. and Coleri Ergen, S. (2019, September). Birbirlerine göre hareket eden araçların bağıl konumlarının belirlenmesi için bir yöntem ve sistem. *T.R. Patent 2019/13680*

3. [Soner and Coleri Ergen, 2019b]: Soner, B., and Coleri Ergen, S. (2019, June). A Low-SWaP, low-cost transceiver for physically secure UAV communication with visible light. In *International Symposium on Innovative and Interdisciplinary Applications of Advanced Technologies* (pp. 355-364). Springer, Cham.

4. [Soner et al., 2020]: Soner, B., Gürbilek, G., and Koca, M. (2020, February). Internal technical project report: Novel inter-vehicular communication techniques. *Koç University Ford Otosan Automotive Technologies Laboratory (KUFOTAL).*

5. [Soner and Coleri, 2021c]: Soner, B., and Coleri, S. (2021). Visible Light Communication Based Vehicle Localization for Collision Avoidance and Platooning. *IEEE Transactions on Vehicular Technology*, 70(3), 2167-2180.

6. [Soner et al., 2022]: Soner, B., Karakas, M., Noyan, U., Sahbaz, F., and Coleri, S. (2022). Vehicular visible light positioning for collision avoidance and platooning: A survey. *Pre-print in progress, planned for submission to IEEE T-ITS Surveys.*

Related supporting articles (not first author):

7. [Turan et al., 2019]: Turan, B., Demir, K. A., Soner, B., and Coleri Ergen, S. (2019). Visible light communications in industrial internet of things (IIOT). In *The Internet of Things in the Industrial Sector* (pp. 163-191). Springer, Cham.

8. [Gurbilek et al., 2019]: Gurbilek, G., Koca, M., Uyrus, A., Soner, B., Basar, E., and Coleri, S. (2019, December). Location-aware adaptive physical layer design for vehicular visible light communication. In *2019 IEEE Vehicular Networking Conference (VNC)* (pp. 1-4). IEEE.

9. [Koca et al., 2020]: Koca, M., Gurbilek, G., Soner, B., and Coleri, S. (2020). Empirical feasibility analysis for energy harvesting intravehicular wireless sensor networks. In *IEEE Internet of Things Journal*, 8(1), 179-186.

10. [Elbir et al., 2020b]: Elbir, A. M., Soner, B., and Coleri, S. (2020). Federated Learning in Vehicular Networks. *arXiv preprint arXiv:2006.01412.*

11. [Elbir et al., 2020a]: Elbir, A. M., Gurbilek, G., Soner, B., and Coleri, S. (2020). Vehicular Networks for Combating a Worldwide Pandemic: Preventing the Spread of COVID-19. *arXiv preprint arXiv:2010.07602.*

BIBLIOGRAPHY

[Abboud et al., 2016] Abboud, K., Omar, H. A., and Zhuang, W. (2016). Interworking of DSRC and cellular network technologies for V2X communications: A survey. *IEEE Trans. Veh. Technol.*, 65(12):9457–9470.

[Ackermann, 1994] Ackermann, J. (1994). Robust decoupling of car steering dynamics with arbitrary mass distribution. In *Proceedings of 1994 American Control Conference-ACC'94*, volume 2, pages 1964–1968. IEEE.

[Alam et al., 2011] Alam, N., Balaei, A. T., and Dempster, A. G. (2011). A cooperative positioning method for VANETs using DSRC carrier frequency offset. In *Int. Global Navigation Satellite Systems (IGNSS) Symp.* Citeseer.

[Alam and Dempster, 2013] Alam, N. and Dempster, A. G. (2013). Cooperative positioning for vehicular networks: Facts and future. *IEEE Trans. Intell. Transp. Syst.*, 14(4):1708–1717.

[Althoff et al., 2009] Althoff, M., Stursberg, O., and Buss, M. (2009). Model-based probabilistic collision detection in autonomous driving. *IEEE Transactions on Intelligent Transportation Systems*, 10(2):299–310.

[American Association of Highway and Transportation Officials (AASHTO), 2011a] American Association of Highway and Transportation Officials (AASHTO) (2011a). Chapter 3.4.6: Vertical curves. In *A Policy on Geometric Design of Highways and Streets, 7th edition*, pages 295–310.

[American Association of Highway and Transportation Officials (AASHTO), 2011b] American Association of Highway and Transportation Officials (AASHTO)

(2011b). Chapter 3.4.6: Vertical curves. In *A Policy on Geometric Design of Highways and Streets, 7th edition*, pages 295–310.

[Ansari, 2021] Ansari, K. (2021). Joint use of dsrc and c-v2x for v2x communications in the 5.9 ghz its band. *IET Intelligent Transport Systems.*

[Antoniali et al., 2013] Antoniali, M., De Piante, M., and Tonello, A. M. (2013). Plc noise and channel characterization in a compact electrical car. In *2013 IEEE 17th international symposium on power line communications and its applications*, pages 29–34. IEEE.

[Aparicio-Esteve et al., 2019] Aparicio-Esteve, E., Hernández, Á., Ureña, J., and Villadangos, J. M. (2019). Visible light positioning system based on a quadrant photodiode and encoding techniques. *IEEE Trans. Instrum. Meas.*

[Aparicio-Esteve et al., 2021] Aparicio-Esteve, E., Ureña, J., Hernández, Á., Pizarro, D., and Moltó, D. (2021). Using perspective-n-point algorithms for a local positioning system based on leds and a qada receiver. *Sensors*, 21(19):6537.

[Arafa et al., 2012] Arafa, A., Jin, X., and Klukas, R. (2012). Wireless indoor optical positioning with a differential photosensor. *IEEE Photon. Technol. Lett*, 24(12):1027–1029.

[Armstrong et al., 2013] Armstrong, J., Sekercioglu, Y. A., and Neild, A. (2013). Visible light positioning: a roadmap for international standardization. *IEEE Communications Magazine*, 51(12):68–73.

[Badino et al., 2009] Badino, H., Franke, U., and Pfeiffer, D. (2009). The stixel world - A compact medium level representation of the 3D world. In *Joint Pattern Recognition Symposium*, pages 51–60. Springer.

[Bai et al., 2011] Bai, B., Chen, G., Xu, Z., and Fan, Y. (2011). Visible light positioning based on LED traffic light and photodiode. In *2011 IEEE Vehicular Technology Conference (VTC Fall)*, pages 1–5. IEEE.

[Bailey and Durrant-Whyte, 2006] Bailey, T. and Durrant-Whyte, H. (2006). Simultaneous localization and mapping (slam): Part ii. *IEEE robotics & automation magazine*, 13(3):108–117.

[Balico et al., 2018] Balico, L. N., Loureiro, A. A., Nakamura, E. F., Barreto, R. S., Pazzi, R. W., and Oliveira, H. A. (2018). Localization prediction in vehicular ad hoc networks. *IEEE Commun. Surveys Tuts.*, 20(4):2784–2803.

[Baltar et al., 2011] Baltar, L. G., Schaich, F., Renfors, M., and Nossek, J. A. (2011). Computational complexity analysis of advanced physical layers based on multicarrier modulation. In *2011 Future Network & Mobile Summit*, pages 1–8. IEEE.

[Bastiaens et al., 2020] Bastiaens, S., Deprez, K., Martens, L., Joseph, W., and Plets, D. (2020). A comprehensive study on light signals of opportunity for subdecimetre unmodulated visible light positioning. *Sensors*, 20(19):5596.

[Bazzi, 2019] Bazzi, A. (2019). Congestion control mechanisms in ieee 802.11 p and sidelink c-v2x. In *2019 53rd Asilomar Conference on Signals, Systems, and Computers*, pages 1125–1130. IEEE.

[Béchadergue et al., 2016] Béchadergue, B., Chassagne, L., and Guan, H. (2016). Visible light phase-shift rangefinder for platooning applications. In *2016 IEEE 19th International Conference on Intelligent Transportation Systems (ITSC)*, pages 2462–2468. IEEE.

[Béchadergue et al., 2017] Béchadergue, B., Chassagne, L., and Guan, H. (2017). A visible light-based system for automotive relative positioning. In *2017 IEEE SENSORS*, pages 1–3. IEEE.

[Béchadergue et al., 2018] Béchadergue, B., Chassagne, L., and Guan, H. (2018). Vehicle-to-vehicle visible light phase-shift rangefinder based on the automotive lighting. *IEEE Sensors Journal*, 18(13):5334–5342.

[Béchadergue et al., 2019] Béchadergue, B., Chassagne, L., and Guan, H. (2019). Simultaneous visible light communication and distance measurement based on the automotive lighting. *IEEE Transactions on Intelligent Vehicles*, 4(4):532–547.

[Beiker, 2016] Beiker, S. (2016). Deployment scenarios for vehicles with higher-order automation. In *Autonomous Driving*, pages 193–211. Springer.

[Broumandan et al., 2008] Broumandan, A., Lin, T., Nielsen, J., and Lachapelle, G. (2008). Practical results of hybrid AOA/TDOA geo-location estimation in CDMA wireless networks. In *2008 IEEE 68th Vehicular Technology Conference*, pages 1–5. IEEE.

[Brown and Laurier, 2017] Brown, B. and Laurier, E. (2017). The trouble with autopilots: Assisted and autonomous driving on the social road. In *Proceedings of the 2017 CHI conference on human factors in computing systems*, pages 416–429.

[Cailean et al., 2014] Cailean, A.-M., Cagneau, B., Chassagne, L., Popa, V., and Dimian, M. (2014). A survey on the usage of dsrc and vlc in communication-based vehicle safety applications. In *2014 IEEE 21st Symposium on Communications and Vehicular Technology in the Benelux (SCVT)*, pages 69–74. IEEE.

[Căilean and Dimian, 2016] Căilean, A.-M. and Dimian, M. (2016). Toward environmental-adaptive visible light communications receivers for automotive applications: A review. *IEEE Sensors Journal*, 16(9):2803–2811.

[Căilean and Dimian, 2017] Căilean, A.-M. and Dimian, M. (2017). Current challenges for visible light communications usage in vehicle applications: A survey. *IEEE Commun. Surveys Tuts.*, 19(4):2681–2703.

[Căilean et al., 2020] Căilean, A.-M., Dimian, M., and Popa, V. (2020). Noise-adaptive visible light communications receiver for automotive applications: A step toward self-awareness. *Sensors*, 20(13):3764.

[CAMP Vehicle Safety Communications Consortium, 2005] CAMP Vehicle Safety Communications Consortium (2005). Vehicle safety communications project: Task 3 final report: identify intelligent vehicle safety applications enabled by DSRC. *NHTSA, US Department of Transportation, Washington DC.*

[Carbonneau et al., 1986] Carbonneau, R., Dubois, J., and Harris, G. (1986). An optical gun muzzle sensor to improve firing accuracy. In *Optical Testing and Metrology*, volume 661, pages 352–358. International Society for Optics and Photonics.

[Caveney, 2010] Caveney, D. (2010). Cooperative vehicular safety applications. *IEEE Control Syst. Mag*, 30(4):38–53.

[Chen et al., 1999] Chen, C., Hargis, M., Woodall, J., Melloch, M., Reynolds, J., Yablonovitch, E., and Wang, W. (1999). Ghz bandwidth gaas light-emitting diodes. *Applied physics letters*, 74(21):3140–3142.

[Chen and Abedi, 2010] Chen, J. and Abedi, A. (2010). A hybrid framework for radio localization in broadband wireless systems. In *2010 IEEE Global Telecommunications Conference GLOBECOM 2010*, pages 1–6. IEEE.

[Chen and Jiang, 2016] Chen, X. and Jiang, M. (2016). Adaptive statistical bayesian mmse channel estimation for visible light communication. *IEEE transactions on signal processing*, 65(5):1287–1299.

[Cincotta et al., 2019] Cincotta, S., He, C., Neild, A., and Armstrong, J. (2019). Indoor visible light positioning: Overcoming the practical limitations of the quadrant angular diversity aperture receiver (QADA) by using the two-stage QADA-plus receiver. *Sensors*, 19(4):956.

[Cincotta et al., 2017] Cincotta, S., Neild, A., He, C., and Armstrong, J. (2017). Visible light positioning using an aperture and a quadrant photodiode. In *2017 IEEE Globecom Workshops (GC Wkshps)*, pages 1–6. IEEE.

[Ciurana et al., 2009] Ciurana, M., López, D., and Barceló-Arroyo, F. (2009). SofTOA: Software ranging for TOA-based positioning of WLAN terminals. In *International Symposium on Location-and Context-Awareness*, pages 207–221. Springer.

[Coleri et al., 2002] Coleri, S., Ergen, M., Puri, A., and Bahai, A. (2002). Channel estimation techniques based on pilot arrangement in ofdm systems. *IEEE Transactions on broadcasting*, 48(3):223–229.

[de Ponte Müller, 2017] de Ponte Müller, F. (2017). Survey on ranging sensors and cooperative techniques for relative positioning of vehicles. *Sensors*, 17(2):271.

[Deng et al., 2018] Deng, C., Wu, Q., Wu, Q., Hu, F., Lyu, F., and Tan, M. (2018). Visual grounding via accumulated attention. In *Proceedings of the IEEE conference on computer vision and pattern recognition*, pages 7746–7755.

[DESTATIS, 2017] DESTATIS (2017). Statistisches Bundesamt (DESTATIS) Verkehrsunfälle 2017. `https://www.destatis.de/GPStatistik/receive/DEHeft_heft_00083585`. Accessed: 2020-03-06.

[Do and Yoo, 2016] Do, T.-H. and Yoo, M. (2016). An in-depth survey of visible light communication based positioning systems. *Sensors*, 16(5):678.

[Dolgov et al., 2010] Dolgov, D., Thrun, S., Montemerlo, M., and Diebel, J. (2010). Path planning for autonomous vehicles in unknown semi-structured environments. *The international journal of robotics research*, 29(5):485–501.

[Eckhoff et al., 2013] Eckhoff, D., Sofra, N., and German, R. (2013). A performance study of cooperative awareness in etsi its g5 and ieee wave. In *2013 10th Annual Conference on Wireless On-demand Network Systems and Services (WONS)*, pages 196–200. IEEE.

[Edmund Optics, 2019] Edmund Optics (2019). Edmund optics tech tools, focal length calculator. `https://www.edmundoptics.com/resources/tech-tools/focal-length`. Accessed: 2019-10-06.

[Elbir et al., 2020a] Elbir, A. M., Gurbilek, G., Soner, B., and Coleri, S. (2020a). Vehicular networks for combating a worldwide pandemic: Preventing the spread of covid-19. *arXiv preprint arXiv:2010.07602*.

[Elbir et al., 2020b] Elbir, A. M., Soner, B., and Coleri, S. (2020b). Federated learning in vehicular networks. *arXiv preprint arXiv:2006.01412*.

[Eldeeb and Uysal, 2019] Eldeeb, H. B. and Uysal, M. (2019). Vehicle-to-vehicle visible light communication: How to select receiver locations for optimal performance? In *2019 11th International Conference on Electrical and Electronics Engineering (ELECO)*, pages 402–405. IEEE.

[Eroglu et al., 2015] Eroglu, Y. S., Guvenc, I., Pala, N., and Yuksel, M. (2015). Aoa-based localization and tracking in multi-element vlc systems. In *2015 IEEE 16th annual wireless and microwave technology conference (WAMICON)*, pages 1–5. IEEE.

[Faisal et al., 2021] Faisal, A., Yigitcanlar, T., Kamruzzaman, M., and Paz, A. (2021). Mapping two decades of autonomous vehicle research: A systematic scientometric analysis. *Journal of Urban Technology*, 28(3-4):45–74.

[Feng et al., 2008] Feng, Y., Wang, J., et al. (2008). GPS RTK performance characteristics and analysis. *Positioning*, 1(13).

[Fletcher et al., 2020] Fletcher, R., Mahindroo, A., Santhanam, N., and Tschiesner, A. (2020). The case for an end-to-end automotive-software platform. *McKinsey & Company*.

[Ford, 2018] Ford (16 Aug 2018). A matter of trust: Ford's approach to developing self-driving vehicles. Ford Motor Company, Press Release.

[Gade, 2016] Gade, K. (2016). The seven ways to find heading. *The Journal of Navigation*, 69(5):955–970.

[Gonçalves et al., 2021] Gonçalves, A. L. R., Maia, Á. H. A., Santos, M. R., de Lima, D. A., and Neto, A. M. (2021). Visible light positioning and communication methods and their application in the intelligent mobility. *IEEE Latin America Transactions*, 19(11):1883–1894.

[Grabner and Kvicera, 2013] Grabner, M. and Kvicera, V. (2013). Multiple scattering in rain and fog on free-space optical links. *Journal of lightwave technology*, 32(3):513–520.

[Guelman et al., 2004] Guelman, M., Kogan, A., Kazarian, A., Livne, A., Orenstein, M., and Michalik, H. (2004). Acquisition and pointing control for inter-satellite laser communications. *ieee transactions on aerospace and electronic systems*, 40(4):1239–1248.

[Gurbilek et al., 2019] Gurbilek, G., Koca, M., Uyrus, A., Soner, B., Basar, E., and Coleri, S. (2019). Location-aware adaptive physical layer design for vehicular visible light communication. In *2019 IEEE Vehicular Networking Conference (VNC)*, pages 1–4. IEEE.

[Gustafsson and Gunnarsson, 2005] Gustafsson, F. and Gunnarsson, F. (2005). Mobile positioning using wireless networks: possibilities and fundamental limitations based on available wireless network measurements. *IEEE Signal Process. Mag.*, 22(4):41–53.

[He et al., 2019] He, C., Cincotta, S., Mohammed, M. M., and Armstrong, J. (2019). Angular diversity aperture (ada) receivers for indoor multiple-input multiple-output (mimo) visible light communications (vlc). *IEEE Access*, 7:145282–145301.

[He and Zhou, 2021] He, J. and Zhou, B. (2021). Vehicle positioning scheme based on visible light communication using a cmos camera. *Optics express*, 29(17):27278–27290.

[Herschfelt et al., 2020] Herschfelt, A., Chiriyath, A., Bliss, D. W., Richmond, C. D., Mitra, U., and Blunt, S. D. (2020). Vehicular rf convergence: Simultaneous radar, communications, and pnt for urban air mobility and automotive applications. In *2020 IEEE Radar Conference (RadarConf20)*, pages 1–6. IEEE.

[Huang et al., 2015] Huang, X., Wang, Z., Shi, J., Wang, Y., and Chi, N. (2015). 1.6 gbit/s phosphorescent white led based vlc transmission using a cascaded pre-equalization circuit and a differential outputs pin receiver. *Optics express*, 23(17):22034–22042.

[IALA E-122, 2001] IALA E-122 (2001). Recommendation on the Photometry of Marine Aids to Navigation Signal Lights, Section 2.4. Recommendation, AISM/IALA E-122, Saint Germain en Laye, FR.

[Isermann et al., 2002] Isermann, R., Schwarz, R., and Stolzl, S. (2002). Fault-tolerant drive-by-wire systems. *IEEE Control Systems Magazine*, 22(5):64–81.

[Jacobs et al., 2015] Jacobs, V., Forment, S., Rombauts, P., and Hanselaer, P. (2015). Near-field and far-field goniophotometry of narrow-beam led arrays. *Lighting Research & Technology*, 47(4):470–482.

[Janai et al., 2020a] Janai, J., Güney, F., Behl, A., Geiger, A., et al. (2020a). Computer vision for autonomous vehicles: Problems, datasets and state of the art. *Foundations and Trends® in Computer Graphics and Vision*, 12(1–3):1–308.

[Janai et al., 2020b] Janai, J., Güney, F., Behl, A., Geiger, A., et al. (2020b). Computer vision for autonomous vehicles: Problems, datasets and state of the art. *Foundations and Trends® in Computer Graphics and Vision*, 12(1–3):1–308.

[Jiang et al., 2019] Jiang, R., Wang, X., Cao, S., Zhao, J., and Li, X. (2019). Deep neural networks for channel estimation in underwater acoustic ofdm systems. *IEEE access*, 7:23579–23594.

[Jootel, 2012] Jootel, P. (2012). SAfe road TRains for the environment. *SARTRE Project, Final Project Report*.

[Jung et al., 2011] Jung, S.-Y., Hann, S., and Park, C.-S. (2011). Tdoa-based optical wireless indoor localization using led ceiling lamps. *IEEE Transactions on Consumer Electronics*, 57(4):1592–1597.

[Kaempchen et al., 2009] Kaempchen, N., Schiele, B., and Dietmayer, K. (2009). Situation assessment of an autonomous emergency brake for arbitrary vehicle-to-vehicle collision scenarios. *IEEE Trans. Intell. Transp. Syst.*, 10(4):678–687.

[Kahn and Barry, 1997] Kahn, J. M. and Barry, J. R. (1997). Wireless infrared communications. *Proceedings of the IEEE*, 85(2):265–298.

[Kahn et al., 1998] Kahn, J. M., You, R., Djahani, P., Weisbin, A. G., Teik, B. K., and Tang, A. (1998). Imaging diversity receivers for high-speed infrared wireless communication. *IEEE Communications Magazine*, 36(12):88–94.

[Kay, 1993] Kay, S. M. (1993). *Fundamentals of statistical signal processing*. Prentice Hall PTR.

[Kaymak et al., 2018] Kaymak, Y., Rojas-Cessa, R., Feng, J., Ansari, N., Zhou, M., and Zhang, T. (2018). A survey on acquisition, tracking, and pointing mechanisms for mobile free-space optical communications. *IEEE Communications Surveys & Tutorials*, 20(2):1104–1123.

[Kelly and Cusick, 1986] Kelly, R. J. and Cusick, D. R. (1986). Distance measuring equipment and its evolving role in aviation. *Advances in electronics and electron physics*, 68:1–243.

[Keskin and Gezici, 2016] Keskin, M. F. and Gezici, S. (2016). Comparative theoretical analysis of distance estimation in visible light positioning systems. *Journal of Lightwave Technology*, 34(3):854–865.

[Keskin et al., 2017] Keskin, M. F., Gezici, S., and Arikan, O. (2017). Direct and two-step positioning in visible light systems. *IEEE Transactions on Communications*, 66(1):239–254.

[Keskin et al., 2018] Keskin, M. F., Sezer, A. D., and Gezici, S. (2018). Localization via visible light systems. *Proceedings of the IEEE*, 106(6):1063–1088.

[Khan and Yuksel, 2015] Khan, M. and Yuksel, M. (2015). Autonomous alignment of free-space-optical links between uavs. In *Proceedings of the 2nd International Workshop on Hot Topics in Wireless*, pages 36–40.

[Kiela et al., 2020] Kiela, K., Barzdenas, V., Jurgo, M., Macaitis, V., Rafanavicius, J., Vasjanov, A., Kladovscikov, L., and Navickas, R. (2020). Review of v2x–iot standards and frameworks for its applications. *Applied Sciences*, 10(12):4314.

[Kirovskii and Gorelov, 2019] Kirovskii, O. and Gorelov, V. (2019). Driver assistance systems: analysis, tests and the safety case. iso 26262 and iso pas 21448. In *IOP Conference Series: Materials Science and Engineering*, volume 534, page 012019. IOP Publishing.

[Klukas and Fattouche, 1998] Klukas, R. and Fattouche, M. (1998). Line-of-sight angle of arrival estimation in the outdoor multipath environment. *IEEE Trans. Veh. Technol*, 47(1):342–351.

[Ko et al., 2012] Ko, J.-K., Cho, M.-R., Lee, M.-J., and Kim, J.-H. (2012). Analysis on iec 62471 for the introduction of photobiological safety of led lamp. In *Proceedings of the Safety Management and Science Conference*, pages 435–443. Korea Safety Management and Science.

[Koca et al., 2020] Koca, M., Gurbilek, G., Soner, B., and Coleri, S. (2020). Empirical feasibility analysis for energy harvesting intravehicular wireless sensor networks. *IEEE Internet of Things Journal*, 8(1):179–186.

[Kusano and Gabler, 2012a] Kusano, K. D. and Gabler, H. C. (2012a). Safety benefits of forward collision warning, brake assist, and autonomous braking systems in rear-end collisions. *IEEE Trans. Intell. Transp. Syst.*, 13(4):1546–1555.

[Kusano and Gabler, 2012b] Kusano, K. D. and Gabler, H. C. (2012b). Safety benefits of forward collision warning, brake assist, and autonomous braking systems in rear-end collisions. *IEEE Trans. Intell. Transp. Syst.*, 13(4):1546–1555.

[Lategahn and Stiller, 2014] Lategahn, H. and Stiller, C. (2014). Vision-only localization. *IEEE Trans. Intell. Transp. Syst.*, 15(3):1246–1257.

[Lee and Atkison, 2021] Lee, M. and Atkison, T. (2021). Vanet applications: Past, present, and future. *Vehicular Communications*, 28:100310.

[Lee and Jung, 2012a] Lee, S. and Jung, S.-Y. (2012a). Location awareness using angle-of-arrival based circular-PD-array for visible light communication. In *2012 18th Asia-Pacific Conference on Communications (APCC)*, pages 480–485. IEEE.

[Lee and Jung, 2012b] Lee, S. and Jung, S.-Y. (2012b). Location awareness using angle-of-arrival based circular-pd-array for visible light communication. In *2012 18th Asia-Pacific Conference on Communications (APCC)*, pages 480–485. IEEE.

[Lefèvre et al., 2014] Lefèvre, S., Vasquez, D., and Laugier, C. (2014). A survey on motion prediction and risk assessment for intelligent vehicles. *ROBOMECH journal*, 1(1):1–14.

[Li et al., 2019] Li, B., Wang, S., Zhang, J., Cao, X., and Zhao, C. (2019). Fast music algorithm for mm-wave massive-mimo radar. *arXiv preprint arXiv:1911.07434*.

[Li et al., 1998] Li, Y., Gao, J., Yu, G., Cao, Y., and Heeger, A. J. (1998). ac impedance of polymer light-emitting electrochemical cells and light-emitting diodes: A comparative study. *Chemical physics letters*, 287(1-2):83–88.

[Liu et al., 2007a] Liu, H., Darabi, H., Banerjee, P., and Liu, J. (2007a). Survey of wireless indoor positioning techniques and systems. *IEEE Trans. Syst., Man, Cybern. Syst., Part C (Applications and Reviews)*, 37(6):1067–1080.

[Liu et al., 2007b] Liu, S., Tan, J., and Hou, B. (2007b). Multicycle synchronous digital phase measurement used to further improve phase-shift laser range finding. *Measurement Science and Technology*, 18(6):1756.

[Liu et al., 2016] Liu, X., Gong, C., Li, S., and Xu, Z. (2016). Signal characterization and receiver design for visible light communication under weak illuminance. *IEEE Communications Letters*, 20(7):1349–1352.

[Lu and Chen, 2010] Lu, P.-W. and Chen, R. (2010). Signal-source trackers on infrared-based dedicated short-range communication. *Infrared physics & technology*, 53(2):127–139.

[Lu and Chen, 2013] Lu, P.-W. and Chen, R. (2013). Infrared-based vehicular positioning with the automatic radiation-strength control. *IET Intelligent Transport Systems*, 8(3):273–285.

[Luo et al., 2017] Luo, J., Fan, L., and Li, H. (2017). Indoor positioning systems based on visible light communication: State of the art. *IEEE Communications Surveys & Tutorials*, 19(4):2871–2893.

[Ma et al., 2019] Ma, S.-H., Lee, C.-H., and Yang, C.-H. (2019). Achromatic led-based projection lens design for automobile headlamp. *Optik*, 191:89–99.

[Mahmoud et al., 2020a] Mahmoud, A. A., Ahmad, Z., Almadani, Y., Ijaz, M., Haas, O. C., and Rajbhandari, S. (2020a). Outdoor visible light positioning using artificial neural networks for autonomous vehicle application. In *2020 12th International Symposium on Communication Systems, Networks and Digital Signal Processing (CSNDSP)*, pages 1–4. IEEE.

[Mahmoud et al., 2020b] Mahmoud, A. A., Ahmad, Z., Almadani, Y., Ijaz, M., Haas, O. C., and Rajbhandari, S. (2020b). Outdoor visible light positioning using artificial neural networks for autonomous vehicle application. In *2020 12th International Symposium on Communication Systems, Networks and Digital Signal Processing (CSNDSP)*, pages 1–4. IEEE.

[Mannoni et al., 2019] Mannoni, V., Berg, V., Sesia, S., and Perraud, E. (2019). A comparison of the v2x communication systems: Its-g5 and c-v2x. In *2019 IEEE 89th Vehicular Technology Conference (VTC2019-Spring)*, pages 1–5. IEEE.

[Manojlović, 2011] Manojlović, L. M. (2011). Quadrant photodetector sensitivity. *Applied optics*, 50(20):3461–3469.

[Mathar, 2015] Mathar, R. J. (2015). Solid angle of a rectangular plate. *Max-Planck Institute of Astronomy*, pages 1–9.

[Maurer et al., 2016] Maurer, M., Gerdes, J. C., Lenz, B., and Winner, H. (2016). *Autonomous driving: technical, legal and social aspects*. Springer Nature.

[Mazuelas et al., 2018] Mazuelas, S., Conti, A., Allen, J. C., and Win, M. Z. (2018). Soft range information for network localization. *IEEE Transactions on Signal Processing*, 66(12):3155–3168.

[Memedi and Dressler, 2020] Memedi, A. and Dressler, F. (2020). Vehicular visible light communications: A survey. *IEEE Communications Surveys & Tutorials*, 23(1):161–181.

[Memedi et al., 2018] Memedi, A., Tebruegge, C., Jahneke, J., and Dressler, F. (2018). Impact of vehicle type and headlight characteristics on vehicular vlc performance. In *2018 IEEE Vehicular Networking Conference (VNC)*, pages 1–8. IEEE.

[Memedi et al., 2017] Memedi, A., Tsai, H.-M., and Dressler, F. (2017). Impact of realistic light radiation pattern on vehicular visible light communication. In *GLOBECOM 2017-2017 IEEE Global Communications Conference*, pages 1–6. IEEE.

[Moreira et al., 1997] Moreira, A. J., Valadas, R. T., and de Oliveira Duarte, A. (1997). Optical interference produced by artificial light. *Wireless Networks*, 3(2):131–140.

[Mukhtar et al., 2015] Mukhtar, A., Xia, L., and Tang, T. B. (2015). Vehicle detection techniques for collision avoidance systems: A review. *IEEE Trans. Intell. Transp. Syst.*, 16(5):2318–2338.

[Nadeem et al., 2014] Nadeem, U., Hassan, N., Pasha, M., and Yuen, C. (2014). Highly accurate 3d wireless indoor positioning system using white led lights. *Electronics Letters*, 50(11):828–830.

[Narmanlioglu et al., 2018] Narmanlioglu, O., Turan, B., Ergen, S. C., and Uysal, M. (2018). Cooperative mimo-ofdm based inter-vehicular visible light communication using brake lights. *Computer Communications*, 120:138–146.

[National Highway Traffic Safety Administration, 1997] National Highway Traffic Safety Administration (1997). Lamps, reflective devices, and associated equipment. *Federal Motor Vehicle Safety Standards, Standard*, 108:49.

[Nguyen and Shin, 2013] Nguyen, T. L. N. and Shin, Y. (2013). A new approach for positioning based on aoa measurements. In *2013 International Conference on Computing, Management and Telecommunications (ComManTel)*, pages 208–211. IEEE.

[NHTSA, 2004] NHTSA (2004). Code of Federal Regulations, Title 49 - Transportation. Volume: 5, 571.108 - Standard No. 108; Lamps, reflective devices, and associated equipment. Section 5.1.1 and Table I.

[Nieto et al., 2006] Nieto, J., Bailey, T., and Nebot, E. (2006). Scan-slam: Combining ekf-slam and scan correlation. In *Field and service robotics*, pages 167–178. Springer.

[Ozaktas and Mendlovic, 1995] Ozaktas, H. M. and Mendlovic, D. (1995). Fractional fourier optics. *JOSA A*, 12(4):743–751.

[Papadimitratos et al., 2009] Papadimitratos, P., De La Fortelle, A., Evenssen, K., Brignolo, R., and Cosenza, S. (2009). Vehicular communication systems: Enabling technologies, applications, and future outlook on intelligent transportation. *IEEE communications magazine*, 47(11):84–95.

[Pathak et al., 2015] Pathak, P. H., Feng, X., Hu, P., and Mohapatra, P. (2015). Visible light communication, networking, and sensing: A survey, potential and challenges. *IEEE communications surveys & tutorials*, 17(4):2047–2077.

[Pendleton et al., 2017] Pendleton, S. D., Andersen, H., Du, X., Shen, X., Meghjani, M., Eng, Y. H., Rus, D., and Ang, M. H. (2017). Perception, planning, control, and coordination for autonomous vehicles. *Machines*, 5(1):6.

[Prince and Little, 2012] Prince, G. B. and Little, T. D. (2012). A two phase hybrid rss/aoa algorithm for indoor device localization using visible light. In *2012 IEEE Global Communications Conference (GLOBECOM)*, pages 3347–3352. IEEE.

[Roberts et al., 2010] Roberts, R., Gopalakrishnan, P., and Rathi, S. (2010). Visible light positioning: Automotive use case. In *2010 IEEE Vehicular Networking Conference*, pages 309–314. IEEE.

[SAE, 2021] SAE (2021). Taxonomy and definitions for terms related to driving automation systems for on-road motor vehicles. *Society of Automotive Engineers, Surface Vehicle Recommended Practice*, J3016 202104.

[Sandell and Edfors, 1996] Sandell, M. and Edfors, O. (1996). *A comparative study of pilot-based channel estimators for wireless OFDM*. Luleå tekniska universitet.

[Sasián, 2019] Sasián, J. (2019). *Introduction to Lens Design*. Cambridge University Press.

[Şayli et al., 2016] Şayli, O., Doğan, H., and Panayirci, E. (2016). On channel estimation in dc biased optical ofdm systems over vlc channels. In *2016 International Conference on Advanced Technologies for Communications (ATC)*, pages 147–151. Ieee.

[Sedlacek and Krumpholc, 2005] Sedlacek, M. and Krumpholc, M. (2005). Digital measurement of phase difference-a comparative study of dsp algorithms. *Metrology and Measurement Systems*, 12(4):427–448.

[Shen et al., 2020] Shen, S., Li, S., and Steendam, H. (2020). Simultaneous position and orientation estimation for visible light systems with multiple leds and multiple pds. *IEEE Journal on Selected Areas in Communications*, 38(8):1866–1879.

[Shieh et al., 2018] Shieh, W.-Y., Hsu, C.-C. J., Lin, C.-H., and Wang, T.-H. (2018). Investigation of vehicle positioning by infrared signal-direction discrimination for short-range vehicle-to-vehicle communications. *IEEE Transactions on Vehicular Technology*, 67(12):11563–11574.

[Shieh et al., 2017] Shieh, W.-Y., Hsu, C.-C. J., and Wang, T.-H. (2017). Vehicle positioning and trajectory tracking by infrared signal-direction discrimination for short-range vehicle-to-infrastructure communication systems. *IEEE Transactions on Intelligent Transportation Systems*, 19(2):368–379.

[Shladover and Tan, 2006] Shladover, S. E. and Tan, S.-K. (2006). Analysis of vehicle positioning accuracy requirements for communication-based cooperative collision warning. *Journal of Intelligent Transportation Systems*, 10(3):131–140.

[Sinha, 2011] Sinha, P. (2011). Architectural design and reliability analysis of a fail-operational brake-by-wire system from iso 26262 perspectives. *Reliability Engineering & System Safety*, 96(10):1349–1359.

[Sirkin et al., 2017] Sirkin, D., Martelaro, N., Johns, M., and Ju, W. (2017). Toward measurement of situation awareness in autonomous vehicles. In *Proceedings of the 2017 CHI Conference on Human Factors in Computing Systems*, pages 405–415.

[Smith and Personick, 1980] Smith, R. and Personick, S. (1980). Receiver design for optical fiber communication systems. In *Semiconductor devices for optical communication*, pages 89–160. Springer.

[Soner, 2021] Soner, B. (2021). *Video for the ES5 collision threat scenario* . `https://youtu.be/z4-dwkrvlLo`.

[Soner and Coleri, 2021a] Soner, B. and Coleri, S. (2021a). *Vehicular VLC-VLP-VPE Simulator*. `https://github.com/sonebu/v2lc_sim`.

[Soner and Coleri, 2021b] Soner, B. and Coleri, S. (2021b). *Vehicular VLP Simulations*. `https://github.com/sonebu/vehicular-vlp-simulations`.

[Soner and Coleri, 2021c] Soner, B. and Coleri, S. (2021c). Visible light communication based vehicle localization for collision avoidance and platooning. *IEEE Transactions on Vehicular Technology*, 70(3):2167–2180.

[Soner and Coleri Ergen, 2019b] Soner, B. and Coleri Ergen, S. (2019b). A low-swap, low-cost transceiver for physically secure uav communication with visible light. In *International Symposium on Innovative and Interdisciplinary Applications of Advanced Technologies*, pages 355–364. Springer.

[Soner and Coleri Ergen, 2019c] Soner, B. and Coleri Ergen, S. (2019c). Vehicular visible light positioning with a single receiver. In *2019 IEEE 30th Annual International Symposium on Personal, Indoor and Mobile Radio Communications (PIMRC)*, pages 1–6. IEEE.

[Soner and Coleri Ergen, 2019a] Soner, B. and Coleri Ergen, S. (T.R. Patent 2019/13680, Sep. 2019a). Birbirlerine göre hareket eden araçların bağıl konumlarının belirlenmesi için bir yöntem ve sistem.

[Soner et al., 2020] Soner, B., Gürbilek, G., and Koca, M. (28.02.2020). Internal technical project report: Novel inter-vehicular communication techniques. *Koç University Ford Otosan Automotive Technologies Laboratory (KUFOTAL)*.

[Soner et al., 2022] Soner, B., Karakas, M., Noyan, U., Sahbaz, F., and Coleri, S. (2022). Vehicular visible light positioning for collision avoidance and platooning: A survey. *Pre-print in Progress*.

[Steendam, 2017] Steendam, H. (2017). A 3-d positioning algorithm for aoa-based vlp with an aperture-based receiver. *IEEE Journal on Selected Areas in Communications*, 36(1):23–33.

[Steendam et al., 2016a] Steendam, H., Wang, T. Q., and Armstrong, J. (2016a). Cramer-Rao bound for indoor visible light positioning using an aperture-based angular-diversity receiver. In *2016 IEEE International Conference on Communications (ICC)*, pages 1–6. IEEE.

[Steendam et al., 2016b] Steendam, H., Wang, T. Q., and Armstrong, J. (2016b). Theoretical lower bound for indoor visible light positioning using received signal strength measurements and an aperture-based receiver. *Journal of Lightwave Technology*, 35(2):309–319.

[Steendam et al., 2017] Steendam, H., Wang, T. Q., and Armstrong, J. (2017).

Cramer-rao bound for aoa-based vlp with an aperture-based receiver. In *2017 IEEE International Conference on Communications (ICC)*, pages 1–6. IEEE.

[Stepniak et al., 2015] Stepniak, G., Schüppert, M., and Bunge, C.-A. (2015). Advanced modulation formats in phosphorous led vlc links and the impact of blue filtering. *Journal of Lightwave Technology*, 33(21):4413–4423.

[Stolte et al., 2021] Stolte, T., Ackermann, S., Graubohm, R., Jatzkowski, I., Klamann, B., Winner, H., and Maurer, M. (2021). A taxonomy to unify fault tolerance regimes for automotive systems: Defining fail-operational, fail-degraded, and fail-safe. *IEEE Transactions on Intelligent Vehicles*.

[Thrun et al., 2006] Thrun, S., Montemerlo, M., Dahlkamp, H., Stavens, D., Aron, A., Diebel, J., Fong, P., Gale, J., Halpenny, M., Hoffmann, G., et al. (2006). Stanley: The robot that won the darpa grand challenge. *Journal of field Robotics*, 23(9):661–692.

[Turan and Coleri, 2021] Turan, B. and Coleri, S. (2021). Machine learning based channel modeling for vehicular visible light communication. *IEEE Transactions on Vehicular Technology*, 70(10):9659–9672.

[Turan et al., 2019] Turan, B., Demir, K. A., Soner, B., and Ergen, S. C. (2019). Visible light communications in industrial internet of things (iiot). In *The Internet of Things in the Industrial Sector*, pages 163–191. Springer.

[Turan et al., 2018] Turan, B., Gurbilek, G., Uyrus, A., and Ergen, S. C. (2018). Vehicular vlc frequency domain channel sounding and characterization. In *2018 IEEE Vehicular Networking Conference (VNC)*, pages 1–8. IEEE.

[Ucar et al., 2016] Ucar, S., Ergen, S. C., and Ozkasap, O. (2016). Security vulnerabilities of ieee 802.11 p and visible light communication based platoon. In *2016 IEEE Vehicular Networking Conference (VNC)*, pages 1–4. IEEE.

[Ucar et al., 2018] Ucar, S., Ergen, S. C., and Ozkasap, O. (2018). Ieee 802.11 p and visible light hybrid communication based secure autonomous platoon. *IEEE Transactions on Vehicular Technology*, 67(9):8667–8681.

[UN ECE Regulation, No R112, 2004] UN ECE Regulation, No R112 (2004). Uniform provisions concerning the approval of motor vehicle headlamps emitting an asymmetrical passing beam or a driving beam or both and equipped with filament lamps.

[UNECE, 2021] UNECE (2021). Addendum 156 – un regulation no. 157. uniform provisions concerning the approval of vehicles with regard to automated lane keeping systems.
`https://unece.org/sites/default/files/2021-03/R157e.pdf`.

[Urey, 2004] Urey, H. (2004). Spot size, depth-of-focus, and diffraction ring intensity formulas for truncated gaussian beams. *Applied optics*, 43(3):620–625.

[Va et al., 2016] Va, V., Shimizu, T., Bansal, G., and Heath Jr, R. W. (2016). Millimeter wave vehicular communications: A survey. *Foundations and Trends® in Networking*, 10(1):1–118.

[Van Welden et al., 2009] Van Welden, D., Steendam, H., and Moeneclaey, M. (2009). Time delay estimation for ksp-ofdm systems in multipath fading channels. In *2009 IEEE 20th International Symposium on Personal, Indoor and Mobile Radio Communications*, pages 3064–3068. IEEE.

[Vandi et al., 2013] Vandi, G., Moro, D., Ponti, F., Parenti, R., and Einaudi, G. (2013). Vehicle dynamics modeling for real-time simulation. Technical report, SAE Technical Paper.

[Viriyasitavat et al., 2013] Viriyasitavat, W., Yu, S.-H., and Tsai, H.-M. (2013). Short paper: Channel model for visible light communications using off-the-shelf scooter taillight. In *2013 IEEE Vehicular Networking Conference*, pages 170–173. IEEE.

[Walther et al., 2010] Walther, F. G., Michael, S., Parenti, R. R., and Taylor, J. A. (2010). Air-to-ground lasercom system demonstration design overview and results summary. In *Free-Space Laser Communications X*, volume 7814, page 78140Y. International Society for Optics and Photonics.

[Wang et al., 2014] Wang, T. Q., Green, R. J., and Armstrong, J. (2014). Prism array-based receiver with application in MIMO indoor optical wireless communications. In *2014 16th International Conference on Transparent Optical Networks (ICTON)*, pages 1–4. IEEE.

[Wang et al., 2013a] Wang, T. Q., Sekercioglu, Y. A., and Armstrong, J. (2013a). Analysis of an optical wireless receiver using a hemispherical lens with application in MIMO visible light communications. *Journal of Lightwave Technology*, 31(11):1744–1754.

[Wang et al., 2013b] Wang, T. Q., Sekercioglu, Y. A., Neild, A., and Armstrong, J. (2013b). Position accuracy of time-of-arrival based ranging using visible light with application in indoor localization systems. *Journal of Lightwave Technology*, 31(20):3302–3308.

[Wang et al., 2015] Wang, Z., Tsonev, D., Videv, S., and Haas, H. (2015). On the design of a solar-panel receiver for optical wireless communications with simultaneous energy harvesting. *IEEE Journal on Selected Areas in Communications*, 33(8):1612–1623.

[Wedel et al., 2009] Wedel, A., Badino, H., Rabe, C., Loose, H., Franke, U., and Cremers, D. (2009). B-spline modeling of road surfaces with an application to free-space estimation. *IEEE transactions on Intelligent transportation systems*, 10(4):572–583.

[Windisch et al., 2000] Windisch, R., Knobloch, A., Kuijk, M., Rooman, C., Dutta, B., Kiesel, P., Borghs, G., Dohler, G., and Heremans, P. (2000). Large-signal-modulation of high-efficiency light-emitting diodes for optical communication. *IEEE journal of quantum electronics*, 36(12):1445–1453.

[Wu et al., 2002] Wu, H., Cheng, S., Peng, Y., Long, K., and Ma, J. (2002). IEEE 802.11 distributed coordination function (DCF): analysis and enhancement. In *2002 IEEE International Conference on Communications. Conference Proceedings. ICC 2002 (Cat. No. 02CH37333)*, volume 1, pages 605–609. IEEE.

[Xu and Xu, 2019] Xu, R. and Xu, Z. (2019). Led-based vehicular visible light ranging. In *ICC 2019-2019 IEEE International Conference on Communications (ICC)*, pages 1–6. IEEE.

[Yamamoto and Ozeki, 1983] Yamamoto, S. and Ozeki, O. (1983). Properties of high-frequency conducted noise from automotive electrical accessories. *IEEE Transactions on Electromagnetic Compatibility*, (1):2–7.

[Yamazato and Haruyama, 2014] Yamazato, T. and Haruyama, S. (2014). Image sensor based visible light communication and its application to pose, position, and range estimations. *IEICE transactions on communications*, 97(9):1759–1765.

[Yamazato et al., 2014] Yamazato, T., Takai, I., Okada, H., Fujii, T., Yendo, T., Arai, S., Andoh, M., Harada, T., Yasutomi, K., Kagawa, K., et al. (2014). Image-sensor-based visible light communication for automotive applications. *IEEE Commun. Mag.*, 52(7):88–97.

[Yang et al., 2020] Yang, H., Zhong, W.-D., Chen, C., Alphones, A., Du, P., Zhang, S., and Xie, X. (July 2020). Coordinated resource allocation-based integrated visible light communication and positioning systems for indoor iot. *IEEE Transactions on Wireless Communications*, 17(7):4671–4684.

[Yang et al., 2014a] Yang, S.-H., Kim, H.-S., Son, Y.-H., and Han, S.-K. (2014a). Three-dimensional visible light indoor localization using aoa and rss with multiple optical receivers. *Journal of Lightwave Technology*, 32(14):2480–2485.

[Yang et al., 2014b] Yang, S.-H., Kim, H.-S., Son, Y.-H., and Han, S.-K. (2014b). Three-dimensional visible light indoor localization using aoa and rss with multiple optical receivers. *Journal of Lightwave Technology*, 32(14):2480–2485.

[Yazar and Gezici, 2022] Yazar, O. and Gezici, S. (2022). Optimal pulse design for visible light positioning systems. *Signal Processing*, 191:108334.

[Yesilkaya et al., 2017] Yesilkaya, A., Basar, E., Miramirkhani, F., Panayirci, E., Uysal, M., and Haas, H. (2017). Optical mimo-ofdm with generalized led index modulation. *IEEE Transactions on Communications*, 65(8):3429–3441.

[Yu et al., 2013] Yu, S.-H., Shih, O., Tsai, H.-M., Wisitpongphan, N., and Roberts, R. D. (2013). Smart automotive lighting for vehicle safety. *IEEE Commun. Mag.*, 51(12):50–59.

[Zeadally et al., 2020] Zeadally, S., Guerrero, J., and Contreras, J. (2020). A tutorial survey on vehicle-to-vehicle communications. *Telecommunication Systems*, 73(3):469–489.

[Zhan et al., 2019] Zhan, W., Sun, L., Wang, D., Shi, H., Clausse, A., Naumann, M., Kummerle, J., Konigshof, H., Stiller, C., de La Fortelle, A., et al. (2019). Interaction dataset: An international, adversarial and cooperative motion dataset in interactive driving scenarios with semantic maps. *arXiv preprint arXiv:1910.03088*.

[Zhao et al., 2019] Zhao, T., Xu, Y., Monfort, M., Choi, W., Baker, C., Zhao, Y., Wang, Y., and Wu, Y. N. (2019). Multi-agent tensor fusion for contextual trajectory prediction. In *Proceedings of the IEEE/CVF Conference on Computer Vision and Pattern Recognition*, pages 12126–12134.

[Zheng et al., 2015] Zheng, K., Zheng, Q., Yang, H., Zhao, L., Hou, L., and Chatzimisios, P. (2015). Reliable and efficient autonomous driving: the need for heterogeneous vehicular networks. *IEEE Communications Magazine*, 53(12):72–79.

[Zhu et al., 2017] Zhu, B., Cheng, J., Wang, Y., Yan, J., and Wang, J. (2017). Three-dimensional vlc positioning based on angle difference of arrival with arbitrary tilting angle of receiver. *IEEE Journal on Selected Areas in Communications*, 36(1):8–22.

[Zhu et al., 2019a] Zhu, B., Zhu, Z., Wang, Y., and Cheng, J. (2019a). Optimal optical omnidirectional angle-of-arrival estimator with complementary photodiodes. *Journal of Lightwave Technology*, 37(13):2932–2945.

[Zhu et al., 2019b] Zhu, B., Zhu, Z., Wang, Y., and Cheng, J. (2019b). Optimal optical omnidirectional angle-of-arrival estimator with complementary photodiodes. *Journal of Lightwave Technology*, 37(13):2932–2945.

[Zhuang et al., 2018a] Zhuang, Y., Hua, L., Qi, L., Yang, J., Cao, P., Cao, Y., Wu, Y., Thompson, J., and Haas, H. (2018a). A survey of positioning systems using visible LED lights. *IEEE Commun. Surveys Tuts.*, 20(3):1963–1988.

[Zhuang et al., 2018b] Zhuang, Y., Hua, L., Qi, L., Yang, J., Cao, P., Cao, Y., Wu, Y., Thompson, J., and Haas, H. (2018b). A survey of positioning systems using visible LED lights. *IEEE Commun. Surveys Tuts.*, 20(3):1963–1988.

[Ziegler et al., 2014] Ziegler, J., Bender, P., Schreiber, M., Lategahn, H., Strauss, T., Stiller, C., Dang, T., Franke, U., Appenrodt, N., Keller, C. G., et al. (2014). Making bertha drive—an autonomous journey on a historic route. *IEEE Intelligent transportation systems magazine*, 6(2):8–20.

[Ziehn et al., 2020] Ziehn, J. R., Roschani, M., Ruf, M., Bruestle, D., Beyerer, J., and Helmer, M. (2020). Imaging vehicle-to-vehicle communication using visible light. *Advanced Optical Technologies*, 9(6):339–348.